Overcoming the effects of the Earth's atmosphere on astronomical observations with 3D integrated photonic technologies

By

Izabela Spaleniak

A thesis submitted to Macquarie University

for the degree of

Doctor of Philosophy

Department of Physics and Astronomy

December 2014

Typeset in LaTeX 2_ε.

Abstract

The earth's atmosphere prevents telescopes, astronomical instruments and astrophotonic devices from working at their full capabilities. Atmospheric turbulence introduces wavefront distortions, while hydroxyl molecules in the ozone layer produce strong emission lines in the infrared part of the spectrum. Most techniques to address these problems are inefficient and expensive, forcing the instrumentation to be of large size and cost. By using a femtosecond laser direct-write technique, 3D optical circuitry called *photonic lanterns* were fabricated. The devices enable the creation of compact optical instruments and integrated photonic devices on ground-based telescopes. The objective of this thesis was to optimise the design of photonic lanterns to increase their efficiency, and create an on-sky prototype instrument to demonstrate the feasibility of the approach.

A detailed optimisation of the three main building blocks of photonic lanterns and slit reformatting devices was performed. After optimising design for multimode waveguides, the mode evolution along a transition section between the multimode and isolated single-mode waveguides sections was analysed, and three types and lengths of transition to find the adiabatic regime were studied. An optimal design was identified for which back-to-back photonic lanterns and slit reformatting devices are $>90\%$ efficient.

In the second part of the thesis, fully integrated photonic lanterns with multiple waveguide Bragg gratings were created. Multiple gratings were placed in the waveguide using the point-by-point femtosecond laser inscription technique. Devices which filter

out one, two, three or four wavelengths were fabricated. The best performance was demonstrated by the device with three gratings for wavelengths of 1545 nm, 1552 nm and 1559 nm, featuring grating strengths of 5.12 dB, 5.60 dB, and 2.87 dB, respectively.

In the third part of the thesis, a slit reformatting device and a single-mode high resolution spectrograph were used to create a prototype on-sky demonstrator instrument and conduct a proof-of-concept test. The astronomical data were acquired on the 0.4 m telescope at the Macquarie University Observatory, Sydney. The spectrum of Antares revealed multiple CO band heads in the astronomical H band, as well as sharp atmospheric water absorption lines demonstrating the feasibility of the technique.

Statement of candidate

The integrated photonic lantern project evolved from collaboration between Macquarie University and the Australian Astronomical Observatory. All the work related to the fabrication, characterisation and on-sky demonstration was conducted at Macquarie University with assistance from the Australian Astronomical Observatory.

From the start of my PhD I was involved in the laboratory characterisation of existing prototypes of the integrated photonic lanterns. Further I was involved in characterisation of the multimode waveguides originally lead by Dr. Nem Jovanovic[1], which was reported in the Jovanovic et al. [1]. From there I took over the project and I developed my own fabrication code, designed, fabricated and characterised all the devices presented in the thesis. The fabrication of the photonic lanterns was done with assistance of Dr. Simon Gross[2]. The acquisition of the astronomical data was done with assistance of Dr. João Bento[3], who operates the semi-automated Macquarie University telescope. The spectrograph was designed in collaboration with Dr. Michael Ireland[4]. The coupled mode theory approximation was derived with the help of Dr. Michael Ireland. The data reduction of astronomical observations was done with huge assistance from Dr. Michael Ireland. Two parts of the DesignLantern program (calculate the radii of curvature and export to the G-code) were done by Dr. Simon Gross. Any other components of this thesis, including the design and characterisation processes,

[1]nem@naoj.org – Subaru Telescope - National Astronomical Observatory of Japan (NAOJ)
[2]simon.gross@mq.edu.au – Department of Physics and Astronomy, Macquarie University
[3]joao.bento@mq.edu.au – Department of Physics and Astronomy, Macquarie University
[4]michael.ireland@anu.edu.au – Macquarie University/Australian Astronomical Observatory/Australian National University

represent my work and contributions.

Some of the devices designed, fabricated and characterised by me have been tested on the Subaru Telescope, Hawaii and are a topic of a publication in preparation.

This thesis is submitted in fulfilment of the requirements of the degree of Doctor of Philosophy at Macquarie University and has not been submitted for a higher degree to any other university or institution. I certify that to the best of my knowledge, all sources used and assistance received in the preparation of this thesis have been acknowledged. This thesis does not contain any material which is defamatory of any person, form or corporation and is not in breach of copyright or breach of other rights which shall give rise to any action at Common Law or under Statute.

Izabela Spaleniak

Acknowledgements

I would like to express my sincere gratitude to all the people who have influenced, mentored, and helped me in various ways throughout of my candidature. This thesis would not have been possible without your care and consideration.

First of all I would like to thank my supervisors: Dr. Michael Ireland, Dr. Jon Lawrence, and Professor Michael Withford for the opportunity to carry on the research in astrophotonics in Australia. Their patience, guidance, and mentorship were more than I could ever have hoped for. Mike, thank you for all your dedication, guidance, crazy ideas, passion and for sharing the experience. Even despite your full-on schedule and moving to Canberra you made time for weekly meetings and discussions. Also, thanks to Ally Ireland for hosting me during my visit to Canberra. Jon, thank you for always providing help, support, useful insights, advice, critical feedback and fruitful discussions during my PhD. Mick, thank you for your continued support, giving directions, encouragement and reminding me to not forget about the big picture in my research. I am also grateful to my mentor and co-supervisor Nem Jovanovic for taking me under his wing when I started my PhD, introducing me to all the research-related matters, teaching me scientific structural thinking, sharing his passion and supervising my project on the daily basis and help, even after he moved to Hawaii.

I would also like to thank the astronomy group with whom I shared an office for two years; Stacey, Niyas, Dimitri you made every day in the office so interesting! My great thanks also go to other members of the MQ astronomical instrumentation/astrophotonics group: Carlos Bacigalupo, João Bento, Nick Cvetojevic, and Tobias Feger. Carlos,

thank you for the time you invested in adapting your wavelength scale model for my spectrograph. João, thank you for all the cold nights in the observatory, which were not only productive but also very informative (in the broad sense) and fun. Nick, thank you for all our astrophotonics discussions. Tobias, thank you for all your troubleshooting ideas about issues with the spectrograph.

To my office and lab mates in the CUDOS group: Peter Dekker, Martin Ams, Ben Johnson, Simon Gross, Alex Arriola, Robert Williams, Tom Meany, Yuwen Duan, Jocelyn Liu for your friendship and a very nice and collaborative working environment. Special thanks goes to Peter, for all the moral support, and to Simon, for sharing his broad knowledge and experience, assisting in the lab and always having time to help.

I would also like to thank all the members of the Physics and Astronomy Department at Macquarie University for all the years of support and creating such a friendly and collegial atmosphere. I would also like to thank the administrative staff (Carol, Lisa, Liz, Amanda, Anita) for your help, support and making my life as a PhD student a lot less complicated.

I would also like to thank my housemates at Shirley Road for creating such a nice place to live. Special thanks also goes to Ashley and Paul – Ashley for introducing me to off-track bushwalking and pushing me to successfully complete the Three Peaks; Paul, thanks to you for all amazing bush explorations, adventures and introducing me to dad's jokes. On that note, a big thank to Tristan for being such a great responder to my new puns and terrible jokes.

Most importantly I would like to thank my wonderful boyfriend Tom Murtagh, firstly, for rescuing me out of the bush and then being a fantastic friend, providing limitless support, patiently fixing my code bugs, being always interested in my work and making countless trips to the uni to bring me dinner while I was writing up.

Wreszcie chciałabym podziękować mojej Rodzinie; bratu Łukaszkowi i jego rodzine oraz przede wszystkim moim Rodzicom, Zofii i Józefowi, za Waszą miłość, wsparcie i zapewnienie edukacji. Bez Was nie byłoby to możliwe. To Wam dedykuję tę pracę. Dziękuję!

Iza

Contents

List of Figures

List of Tables

1

Introduction

We are currently experiencing very dynamic and exciting times in the development of astronomical telescopes and instrumentation. While more traditional medium size (2-10 m) telescopes contribute to be deployed, two newer strategies are rising in popularity. The first aims for the development of extremely large telescopes of more than 20 m diameter, such as the Giant Magellan Telescope (24.5 m) [2], the Thirty Meter Telescope (30 m) [3], and the European Extremely Large Telescope (39 m) [4]. The second focuses on the development of multiple small robotic telescopes 0.5-1 m diameter, such as the Solaris Project [5]. However, none of these telescopes operates at full capability due to the earth's atmosphere.

Atmospheric turbulence introduces wavefront distortions creating an unstable image in the telescope focus, called *astronomical seeing*. The seeing not only reduces the precision of the astronomical measurements but also requires larger instruments to

achieve the same sensitivity, angular and spectral resolutions as would a telescope operating in a diffraction-limited regime. When instruments for telescopes are designed to match the natural seeing of the site, the size of the instrument grows proportionally to the telescope diameter $D_{\text{Telescope}}$, creating room-size devices for large telescopes. Such relatively large optical devices require large ($\sim$0.3-0.5 m diameter), expensive optical components as the cost of the instrument scales with the square of the telescope diameter or more [6].

Ideally the seeing effect should be mitigated. The most common solution, adaptive optics, is used mostly on large telescopes due to its complexity and high cost. An adaptive optics system works by analysing the incoming wavefront and applying a correction on a deformable mirror. Because of the high speed of atmospheric turbulence in the visible wavelength range, even the state-of-the-art adaptive optics systems perform poorly in the visible wavelength range. Small and medium size telescopes are not normally equipped with adaptive optics; in order to utilise all the light in their focus they have to adjust their instruments for the seeing-limited, multimode operation. A functionally equivalent system that is less complex and less expensive than adaptive optics would create the perfect link between a seeing-limited telescope and a diffraction-limited spectrograph. Such devices were proposed by Leon-Saval et al. [7] and are called *photonic lanterns*.

Photonic lanterns can in principle provide a lossless transition from a single multimode input to multiple single-mode outputs by utilising the coupling between optical fibres or optical waveguides. Such systems consisting of a photonic lantern and a single-mode spectrograph can enable measurements with high precision and accuracy, e.g. exoplanet detection by means of the radial velocity method [8]. Another great advantage of such systems is the ability to deploy the same device (or with small changes) on multiple telescopes, instead of developing custom devices for each telescope. This in turn can greatly reduce the cost of the systems, as they can be easily replicated and tuned. However, the technology is still fairly young and the fact that it still has not been widely applied is due to the high cost associated with the development of the first fibre photonic lanterns [9], and the low transmission efficiency of integrated

photonic lanterns to date [10]. The low efficiency of the devices translates in astronomy to monetary cost, as low efficiency devices require longer observations. Therefore optimisation of loss reduction is a major concern during the development of astronomical instrumentation.

This thesis presents an exploration of the possibilities and limitations of infrared integrated photonic lanterns. In particular, we focus on optimising their design and fabrication parameters, incorporating spectral filtering and finally acquiring astronomical data. In this chapter we review the two atmospheric effects that are most relevant to this work: astronomical seeing and OH emission. An introduction to fibre optics is also given with a comparison of single-mode and multimode fibres. Finally, the concept of the photonic lantern is presented. In Chapter 2, we provide a background for the femtosecond direct-write technique and give more details on the fabrication aspects important for this work. Chapter 3 discusses the theory and results of modelling of the photonic lantern devices. In Chapter 4 we present the experimental methods for fabrication and characterisation of the photonic lanterns and slit reformatting devices. Chapter 5 presents the experimental results of the design and fabrication optimisation study of the photonic lanterns and slit reformatting devices. Chapter 6 reports on performance of the integrated photonic lanterns incorporating waveguide Bragg gratings. Finally, Chapter 7 outlines an on-sky demonstration of the diffraction-limited, high spectral resolution spectrograph fed with an integrated slit reformatting device. Concluding remarks and future outlook are provided in Chapter 8 along with a summary and key achievements contained in the thesis.

1.1 Atmosphere effects

The electromagnetic waves produced by astronomical objects, for most of their journey propagate in vacuum and they can travel long distances with barely any distortion. When they encounter other media such as gases, the gas molecules interact with the waves and change their speed, direction and location. Since the Earth's atmosphere consists of gases of various types and densities, the electromagnetic waves are affected

in various ways before they reach a telescope. Atmospheric effects include seeing, refraction, absorption, scattering, and emission. All these effects deteriorate the original signal.

The next sections describe two major effects: astronomical seeing, which affects visible and infrared light and OH molecular emission which affects most of the near infrared spectrum. Then classical and novel solutions to mitigate atmospheric effects are presented.

1.1.1 Atmospheric seeing

The Earth's atmosphere consists of multiple layers of gases at various temperatures and pressures. Since the refractive index of air depends primarily on its density, the incoming wavefront from a star is deflected by each layer by a different amount. Even more, each layer consists of independent air patches with different physical conditions (temperature, pressure); turbulence within each layer and the atmosphere as a whole leads to changing physical conditions on small spatial scales, so that the previously flat wavefront is distorted before it reaches the ground [11]. Telescopes are designed to focus a flat wavefront into a diffraction-limited image. However, when the corrugated wavefront reaches the telescope a random distribution of speckles is formed (Fig. 1.1). The timescale variation of the speckle pattern is very short ($<$10 ms), whereas the astronomical observations of faint objects require a much longer integration time. If the image is integrated over a longer time, the speckle patterns overlap and create a smooth, broad Moffat function profile [12]. The atmospheric seeing, θ_{Focus}, is defined as the full width at half maximum (FWHM) of this profile. The smaller the seeing value is, the better seeing conditions there are.

The seeing conditions depend on the thickness of the atmosphere through which the object is observed, and the temporal atmospheric conditions such as wind and temperature gradient. The size of the subsections of the corrugated wavefront, which can be considered as cophased, is called the Fried parameter r_0 [13] and its values are on the order of $r_0 \approx$ 10-20 cm in the visible at a good site [14]. This means that any telescope of a diameter larger than 10-20 cm produces an image which is dominated by

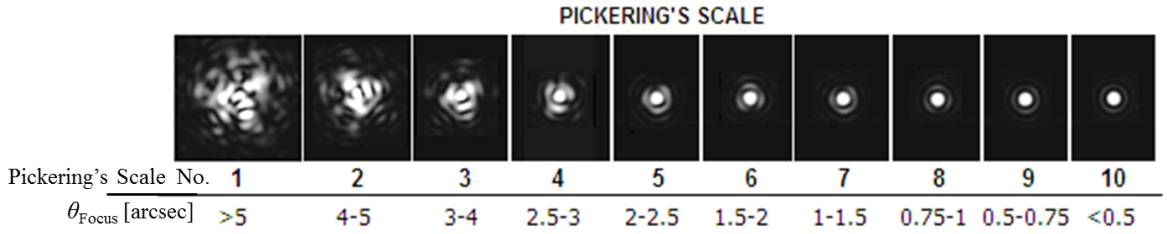

Figure 1.1: Illustration of various seeing conditions according to Pickering's seeing, which is used in amateur astronomy. The scale was created using a 5" (13 cm) refractor. #1 presents the worst seeing conditions – a boiling image without any sign of a diffraction pattern with $\theta_{\text{Seeing}} > 5$ arcsec, while #10 presents a perfect motionless diffraction-limited Airy pattern with $\theta_{\text{Seeing}} < 0.5$ arcsec. Image source: `http://www.telescope-optics.net/induced.htm#3.2._Air-medium_errorsl`.

atmospheric seeing because the incoming wavefront is globally decorrelated and only telescopes of diameter < 10 cm operate in the diffraction-limited regime. The typical seeing size for a good site (i.e. high altitude, low wind) is $\theta_{\text{Seeing}} = 0.5\text{-}1.0$ arcsec (i.e. $r_0 = 10\text{-}20$ cm for $\lambda = 550$ nm) and $\theta_{\text{Seeing}} = 3\text{-}4$ arcsec (i.e. $r_0 = 3\text{-}4$ cm) for places like Sydney.

The FWHM of the point spread function (PSF) created in the focus of the telescope θ_{Focus} is a convolution of the diffraction-limited ($\theta_{\text{Diffraction}}$) and seeing-limited ($\theta_{\text{Seeing}}$) images and can be approximated as a quadratic sum [1]:

$$\theta_{\text{Focus}} = \sqrt{\theta_{\text{Diffraction}}(\lambda)^2 + \theta_{\text{Seeing}}(\lambda)^2} \approx \sqrt{\left(\frac{\lambda}{D_{\text{Telescope}}}\right)^2 + \left(\frac{\lambda}{r_0}\right)^2}, \tag{1.1}$$

where

$$\theta_{\text{Diffraction}}(\lambda) \approx \frac{\lambda}{D_{\text{Telescope}}} \qquad \text{Diffraction-limited image component} \tag{1.2}$$

$$\theta_{\text{Seeing}}(\lambda) = 0.98 \cdot \frac{\lambda}{r_0} \qquad \text{Seeing-limited image component} \tag{1.3}$$

and $D_{\text{Telescope}}$ is the telescope diameter. The top graph in Fig. 1.2 shows the analytical

[1] Based on Dr. Jon Lawrence's Advance Astronomy lecture notes

solution for the PSF in the seeing-limited, as well as the diffraction-limited case and the resulting total PSF for $r_0 = 20\,\mathrm{cm}$ and $\lambda = 550\,\mathrm{nm}$. As can be seen, the image is diffraction-limited when $D_{\mathrm{Telescope}} < r_0$ and becomes seeing-limited when $D_{\mathrm{Telescope}} > r_0$. It means that image of any astronomical object will have the size of the seeing spot or larger.

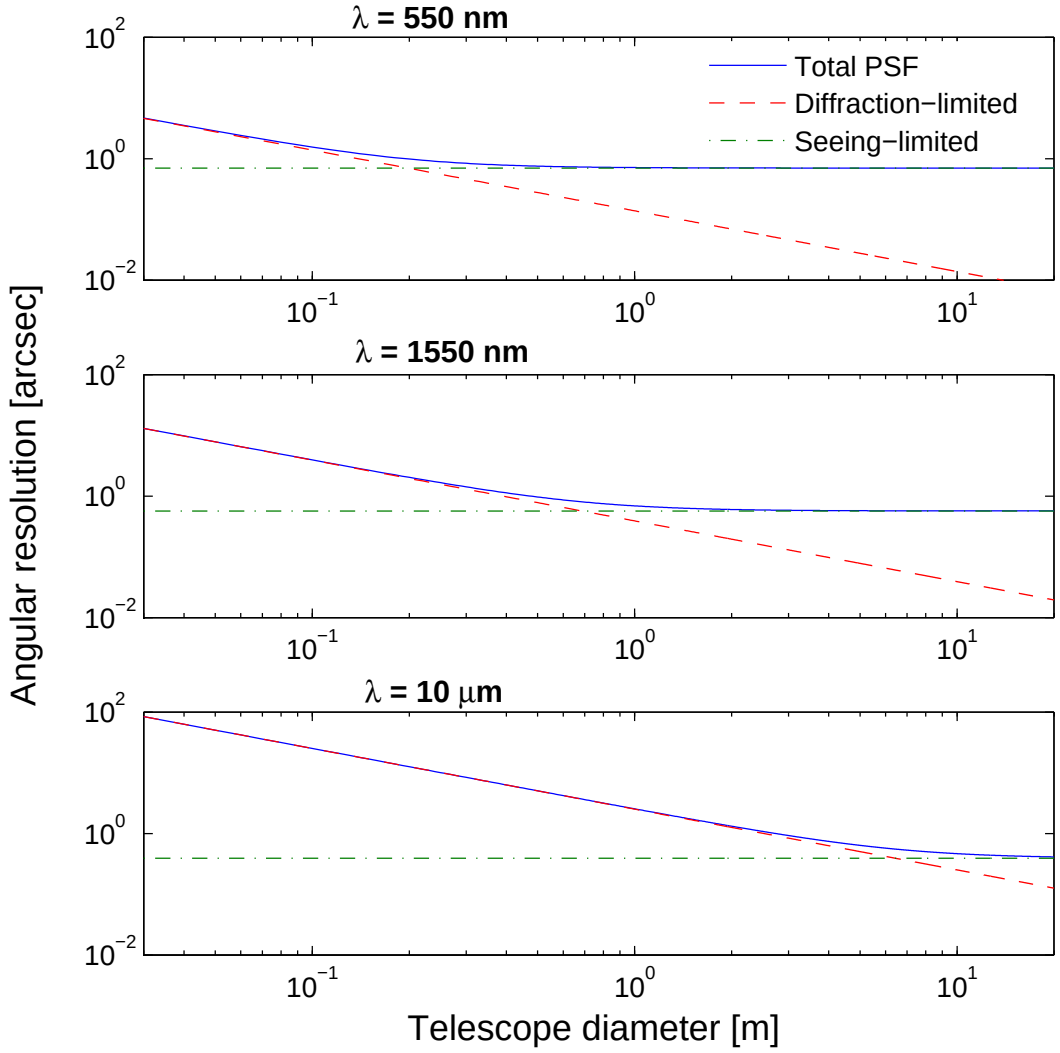

Figure 1.2: Relationship between the telescope angular resolution in a purely diffraction-limited case, purely seeing-limited case and the convolution of both, i.e. total PSF, for $\lambda = 550\,\mathrm{nm}$, $1550\,\mathrm{nm}$ and $10\,\mu\mathrm{m}$ and corresponding seeing $\theta_{\mathrm{Seeing}}(550\,\mathrm{nm}) = 0.7\,\mathrm{arcsec}$, $\theta_{\mathrm{Seeing}}(1550\,\mathrm{nm}) = 0.57\,\mathrm{arcsec}$, $\theta_{\mathrm{Seeing}}(10\,\mu\mathrm{m}) = 0.4\,\mathrm{arcsec}$.

The other parameters describing the atmosphere for astronomers are the coherence timescale τ_0 and isoplanatic angle θ_0. The coherence timescale describes how fast the phase perturbation (i.e. speckle pattern) changes. The isoplanic angle, on the other hand, is the angular size over which the turbulence can be considered coherent and two objects within that angle are influenced by the same atmosphere column. The isoplanic angle can be derived from r_0 and the elevation of the turbulent layer. The typical values of these parameters at good sites are $\tau_0 < 10\,\text{ms}$ and $\theta_0 > 4\,\text{arcsec}$.

The degree of influence of the atmospheric conditions on the astronomical signal depends on the signal wavelength. Both r_0 and τ_0 are wavelength dependent with an approximate relation: $r_0(\lambda) \propto \lambda^{6/5}$ and $\tau_0(\lambda) \propto \lambda^{6/5}$. Figure 1.2 shows a comparison of the telescope PSF at three wavelengths: 550 nm, 1550 nm and 10 µm when $\theta_{Seeing} = 0.7\,\text{arcsec}$ at 550 nm. It can be seen that the seeing contribution is smaller as the wavelength is increased and it is worth noticing that at $\lambda = 10\,\mu\text{m}$ even the existing largest telescopes ($D_{\text{Telescope}} = 12\,\text{m}$) operate in the diffraction-limited regime.

1.1.2 Astronomical spectrographs

An astronomical spectrograph is a device which splits the light from a source into its component wavelengths[2]. In the classic case, i.e. bulk optics-based spectrographs, the beam dispersion (splitting) is realised by means of dispersing elements, such as prisms or gratings (transmission or reflection). Figure 1.3 shows a schematic of an astronomical spectrograph incorporating a transmission grating. The basic components of a spectrograph are: slit, collimator, grating, camera and detector.

The slit isolates the region of interest in the sky and is placed in the focal plane of the telescope. The slit is then reimaged on the detector plane. If the beam is dispersed, each wavelength creates a different image of the slit, shifted in position. The separation between the images ($\Delta\lambda$) depends on the angular dispersion of the disperser and the magnification M of the system ($M = F_{\text{Cam}}/F_{\text{Coll}}$). The divergent beam from the telescope is collimated, so that a parallel beam can hit the grating.

[2]Section based on the lecture notes from courses on astronomical instrumentation by Prof. Vik Dhillon and Prof. Stephen Eikenberry

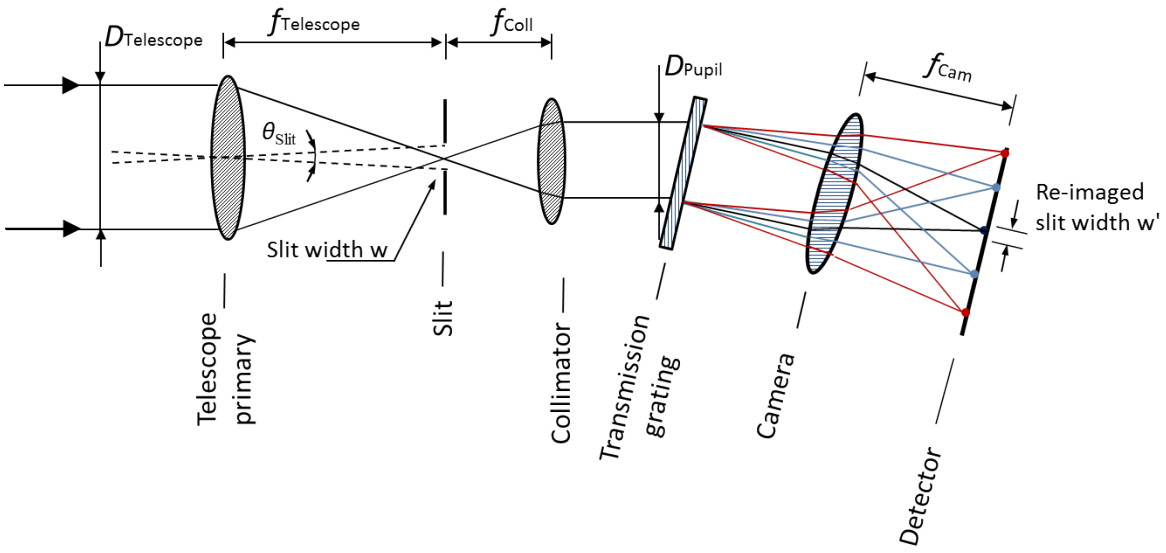

Figure 1.3: Schematic of an astronomical spectrograph incorporating a transmission grating.

The diffraction grating splits the light into its component wavelengths. The grating is placed in the pupil plane, to use a minimum-sized grating and disperse all on- and off-axis rays. The final optical element is a camera, which first collects and then focuses the spectrally dispersed beams onto the detector. In practice, in order to achieve a good quality image over the largest possible wavelength range, the collimator and camera are typically complicated multi-element systems.

1.1.2.1 Spectrograph size scaling

In this section we will introduce the basic theory behind optical spectrographs. The full derivation of the resolving power of a slit spectrograph is not given, as it can be found in the literature [15].

A diffraction grating deflects the light into a wavelength-dependent direction. The angular direction between the dispersed wavelengths is described by the grating equation:

$$m\lambda = d(\sin\alpha + \sin\beta), \tag{1.4}$$

where α is the incident angle, β is the diffracted angle, m is the diffraction order, d is

the grating groove spacing, and λ is the wavelength.

The angular separation between two dispersed wavelengths is given by the angular dispersion A as:

$$A = \frac{\mathrm{d}\beta}{\mathrm{d}\lambda}. \tag{1.5}$$

and for a diffraction grating A is given by:

$$A = \frac{\sin\alpha + \sin\beta}{\lambda \cos\beta}. \tag{1.6}$$

and if we consider the so-called Littrow configuration, i.e. when $\alpha = \beta = \theta_{\mathrm{B}}$, then Eq. 1.6 becomes:

$$A = \frac{2\tan\theta}{\lambda}. \tag{1.7}$$

The main parameter describing a spectrograph is its spectral resolving power R which is defined as:

$$R = \frac{\lambda}{\Delta\lambda}, \tag{1.8}$$

where $\Delta\lambda$ is the smallest difference in wavelengths that can be distinguished by the spectrograph at a wavelength of λ.

For a slit spectrograph (Fig. 1.3) operating at a near Littrow configuration ($\alpha = \beta = \theta_{\mathrm{B}}$) using Eq. 1.7, Eq. 1.8 can be rearranged and expressed as follows:

$$R = \frac{2\tan\theta_{\mathrm{B}} \cdot D_{\mathrm{Pupil}}}{\theta_{\mathrm{Slit}} \cdot D_{\mathrm{Telescope}}}, \tag{1.9}$$

where θ_B is the blaze angle of the grating, D_{Pupil} is the instrument pupil diameter and θ_{Slit} is the slit width. There is a limit on the value for the blaze angle θ_{B}, i.e. in practice it should not be more than $\sim 70°$. When designing a spectrograph for a given telescope of diameter D_{Telesope} the main parameters defining the resolving power R are D_{Pupil} and θ_{Slit}. As depicted in Fig. 1.3 D_{Pupil} determines the size of the optical components in the spectrograph. Large optical components are much more difficult to manufacture and their cost scales approximately as $D^2{}_{\mathrm{Pupil}}$ [16], so ideally it should be kept small. Therefore θ_{Slit} is the main parameter which determines the size and resolution of the

instrument. Ideally θ_{Slit} should match the size of the image at the focus to utilise all the signal captured by a telescope. However, a seeing-limited telescope produces a large image. When matching θ_{Slit} to such a large image, the spectrograph resolution becomes low. The alternative is to narrow the slit, which can produce higher resolution but this potentially throws away some of the light and results in a lower signal-to-noise ratio (S/N). Ideally θ_{Slit} should be small with the light well concentrated. Such is the case when the light is focused into the diffraction-limited spot. Therefore a huge effort has been spent over the years to fight the atmospheric seeing effects.

1.1.3 OH emission

Observations of faint targets from the ground in the near infrared (IR) part of the spectrum, specifically J and H band atmospheric transmission window (1.1-1.4 µm and 1.5-1.8 µm), are extremely difficult because the background is dominated by very bright and narrowband hydroxyl (OH) lines as shown in Fig. 1.4. During the day the solar energy is stored as ozone and other radicals in the upper layers of the atmosphere. The ozone interacts with water to form OH radical, which then decay to the ground state and emit numerous bright lines. Some of the other radicals also produce emission lines but they are much weaker and can be neglected. The other part of the emission is the continuum, which is due to sunlight scattered by interplanetary dust and cannot be removed. The OH lines are as much as 1000 times brighter than the continuum at 1 nm spectral resolution as can be seen in Fig. 1.4, and they are the main source of the background. Beyond 2 µm, thermal emission from the atmosphere begins to dominate the OH emission.

The first way of dealing with the lines was to remove them after astronomical object data acquisition in post-processing by subtracting a sky spectrum, i.e. a spectrum of a blank patch of sky. Unfortunately this solution does not work for all observations. When observing faint objects, such as distant redshifted galaxies, long exposures are needed. However, the strong night sky background dominates the signal, which prohibits long exposures. Therefore it is better to remove the strong emission lines before they reach the instrument and the detector. Several devices have been proposed which

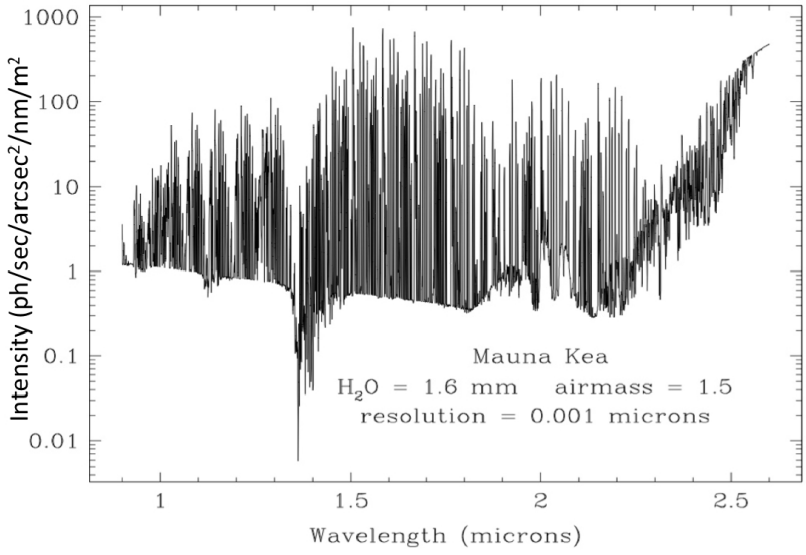

Figure 1.4: The near-IR sky background modelled for the Gemini Observatory at Manua Kea. Most of the strong, individual features are the OH emission lines. Image courtesy: Gemini Observatory.

apply this idea. For instance, Content and Angel [17] proposed an instrument which disperses the incoming light, masks out OH lines and recombines the image afterwards. Such post-dispersion suppression has the disadvantage that it cannot suppress the energy from the OH lines that has been scattered by imperfections in the spectrograph's grating, leaving a residual background that is higher than scattered zodiacal light. Offer and Bland-Hawthorn[18] proposed the use of multiple narrowband interference filters. However, both solutions are expensive, and complex, and introduce losses in the signal.

1.1.4 Mitigation of atmospheric turbulence effects

The obvious solution to overcome the atmospheric effects on image quality is to avoid it completely and send the telescope into space with the detection instruments. Unfortunately, space telescopes are much more expensive than ground-based telescopes and other, less expensive solutions are needed. As mentioned in Section 1.1.1, in a very short timescale (<10 ms) the speckle pattern is stable, so if the images are taken on a

relatively short time scale each of the them contains a collection of diffraction-limited images. Speckle interferometry [19] and *lucky imaging* [20] are based on this concept. Although it allows resolving of small objects and features, it prohibits the observation of faint objects.

A technique called adaptive optics (AO) was proposed [21] in 1953 but only since 1990 has is started being successfully implemented on astronomical telescopes thanks to the development of fast computers and deformable mirrors. Over the past $\sim$ 20 years AO has become the major system for minimising atmospheric turbulence effects. An AO system analyses the incoming deformed wavefront with a wavefront sensor and using a real-time closed-loop corrects the wavefront with a deformable mirror. If the correction is good enough, the signal can then be focused into a quasi-diffraction-limited spot. Nevertheless, the system has drawbacks, including the high cost, the need for bright guide stars and poor performance in the visible wavelength range. The high cost is definitely a prohibitive factor for smaller observatories. The need for a bright guiding star has been tackled by creating a fake, laser guide star using high-power lasers at 589 nm, which excite sodium atoms in the upper atmosphere, or lasers of other wavelengths (532 nm, 355 nm) which are Rayleigh scattered in the air. Consequently this makes the system complex and expensive. The poor visible performance, as explained in Section 1.1.1, results from the shorter coherence times and smaller coherence lengths of the atmosphere in the visible compared to the infrared, and because the atmosphere cannot be well-approximated by a thin phase-screen.

Therefore astronomers are constantly seeking new solutions and new technologies which can improve the quality of the results while reducing the device cost and complexity. Thus, their attention has been attracted to photonic technologies.

1.2 Photonics for astronomy

Over the past three decades there has been an increasing trend towards exploiting photonic technologies for astronomical instrumentation [22]. This began with multimode optical fibres used for transporting light from the telescope to the instrumentation

placed in a remote isolated location. Other recent achievements include the use of laser frequency combs for precise wavelength calibration [23], and the application of photonic chips for multi-aperture interferometry [24], pupil remapping interferometry [25], and spectroscopy [26]. Recent work has focused on the development of a single mode spectrograph [27, 28, 29], which although built with bulk-optics uses a single-mode fibre at spectrograph injection port.

The following section will provide an overview of the basic photonic components with their characteristics, advantages and drawbacks.

1.2.1 Optical fibres

The operating principle of optical fibres is based on the process of total internal reflection. This phenomenon takes place at the interface between two transparent media and allows light to be fully reflected given two conditions being satisfied. Firstly the light has to be coming from a medium of greater refractive index into a medium of lower refractive index, and secondly at a sufficiently large angle of incidence. Optical fibres have a core region of greater refractive index than the cladding, therefore the light can propagate along the core. The angle of incidence has to be larger than the so-called critical angle ϕ_{max}. The critical angle defines also the acceptance angle of the fibre θ_{max}, i.e. the largest angle at which the light launched from air into a fibre is guided successfully, which is depicted in Figure 1.5 and given by the following equation:

$$\theta_{max} = \sin^{-1}\left(\sqrt{n_{\text{core}}^2 - n_{\text{cladding}}^2}\right), \tag{1.10}$$

where n_{core} is the core refractive index and n_{cladding} is the cladding refractive index [30]. The above equation applies to step-index fibres which have uniform refractive indices across the core and cladding regions. For now the discussion will be limited to this type of fibre, as it is the most common and such fibres are a good approximation for the optical properties of the more complex refractive index profile fibres and waveguides.

Based on the equation 1.10, a numerical aperture (NA) in fibre optics can be defined:

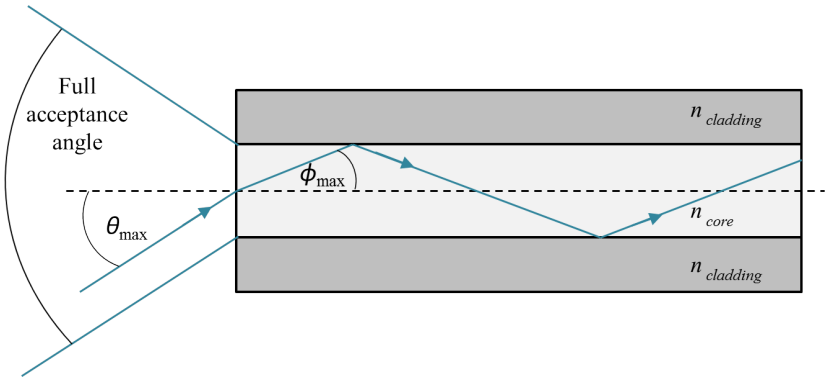

Figure 1.5: Concept of numerical aperture in a multimode optical fibre. This picture breaks down for small waveguides, where a mode approach is required (see Section 3.3).

$$\mathrm{NA} = \sqrt{n_{\mathrm{core}}^2 - n_{\mathrm{cladding}}^2} \tag{1.11}$$

The NA describes the ability of the fibre to capture and guide the light. The typical values of the NA are < 0.2 for single-mode and few mode fibres and 0.2-1.0 for multimode fibres. An equivalent definition of NA exists based on geometrical optics area (see Section 1.2.1.1).

Another important parameter describing guiding properties of the waveguides and fibres is the V number, known also as the waveguide parameter, waveguide frequency or normalised frequency, which is defined as:

$$V = \frac{\pi d}{\lambda}\mathrm{NA} = \frac{\pi d}{\lambda}\sqrt{n_{\mathrm{core}}^2 - n_{\mathrm{cladding}}^2}, \tag{1.12}$$

where d is the core diameter and λ is the propagation wavelength.

The V-number indicates the number of modes which can propagate in a fibre of certain refractive index contrast and diameter at a certain wavelength. When $V < 2.405$ the fibre is always single-mode and when $V > 2.405$ it is multimode. By modifying the diameter and index contrast the fibre can be tuned to be either single-mode or multimode at certain wavelengths. In the following sections the properties of both single-mode and multimode propagation are described.

1.2.1.1 Numerical aperture in an optics context

The numerical aperture (NA) of a lens defines the range of angles which can be accepted by a lens and the beam waist diameter; it is depicted in Figure 1.6 and is given by the equation:

$$\mathrm{NA} = \sin(\theta) \approx \frac{D}{2} \cdot \frac{1}{f}, \tag{1.13}$$

where θ is the half-angle of the maximum cone of light that can enter or exit the lens, D is the lens diameter and f is a focal length of the lens.

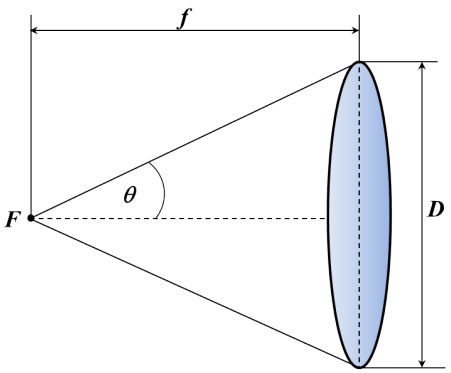

Figure 1.6: Concept of the numerical aperture in optics. F is the focus, f the focal length, D the entrance pupil, θ the acceptance angle.

In astronomical devices a more common term is the so-called focal ratio expressed as:

$$F/\# = \frac{f}{D} \approx \frac{1}{2 \cdot \mathrm{NA}} \tag{1.14}$$

1.2.2 Single-mode fibres

Single-mode fibres allow the propagation of only one fundamental spatial mode per polarisation direction at a given wavelength. In order to maintain the V-number below 2.405, the core diameter of the fibre is usually small (e.g. $d = 3\mu$m at 500 nm, $d = 9\mu$m at 1550 nm) and the index contrast is low. Each fibre also has a cut-off wavelength below which the fibre supports more than one mode. This means that in general the shorter the operating wavelength is, the smaller the fibre diameter has to be.

Single-mode fibres have numerous advantages compared to multimode fibres when used for astronomical applications. The most prominent characteristics are no focal ratio degradation, stable mode profile and no modal noise, when used at single-mode operation wavelength. The next section describes multimode fibres and these effects.

1.2.3 Multimode fibres

Multimode fibres support multiple spatial modes for a given polarisation and wavelength. Their V number is larger than 2.405 therefore their NA and core diameter are usually large (NA = 0.2-0.3, core diameter $\sim$ 50-200 µm). Multimode fibres can usually support hundreds of modes or more. The number of supported modes (N_m) for a step index fibre per polarisation direction, when V is large can be approximated as follows [31]:

$$N_m = \frac{V^2}{4} \tag{1.15}$$

Depending on the launching conditions different modes are excited in the fibre, i.e. light launched at a higher angle and/or more offset from the centre of the fibre excites higher order modes. Each of the propagating modes in the fibre contributes to the total electric field distribution along the fibre. As the modes propagate along the fibre their relative phases change due to the mode dependent propagation constant. As a result the light pattern launched into the fibre is not preserved and the output field varies with length of the fibre.

The propagation constant β determines the phase of a mode along the fibre. The value is specific to a mode in a fibre and defined as [30]:

$$\beta = n_{\text{eff}} \cdot k, \tag{1.16}$$

where k is the wavenumber and defined as:

$$k = \frac{2\pi}{\lambda} \tag{1.17}$$

and n_{eff} is the effective refractive index, and defined in a ray optics approximation as:

$$n_{\text{eff}} = n_{\text{core}} \cdot \cos\phi, \tag{1.18}$$

where ϕ is an angle of incidence in the fibre core (Fig 1.5).

The effective refractive index is different for each mode and for the guided modes it fulfils the condition $n_{\text{cladding}} \leq n_{\text{eff}} \leq n_{\text{core}}$. The modes for which $n_{\text{eff}} < n_{\text{cladding}}$ propagate in the cladding and are therefore called cladding or radiation modes. Depending on the light launching conditions, even though most of the light is coupled into the fibre core, some of the the light may be coupled into a cladding and propagate as a cladding mode. The cladding modes are usually strongly attenuated by dissipation into the fibre coating, so contribute to the coupling losses.

The relatively large core diameter, large acceptance and ability to support multiple (often hundreds of) modes makes multimode fibres a convenient medium to transport incoherent light over a distance. Therefore multimode fibres find an application in astronomical instrumentation to transport the light from the focus of the telescope to the instrument, which can be detached from the telescope structure and placed in a gravity invariant, temperature and vibration controlled laboratory. Because the multimode fibres only partially retain the spatial and angular information, they are not optimal for feeding instruments which require such information, such as imagers, yet they work very well to deliver the light to spectrographs, where they are commonly used. However, there are several drawbacks resulting from the use of multimode fibres, which are non-existent in single-mode fibres. By understanding the characteristics of multimode fibres, the impact can be reduced or corrected. In the Sections 1.2.5, 1.2.6, 1.2.7 three of these effects are discussed.

1.2.4 Telescope/fibre coupling

In order to maximise the throughput of fibre-fed astronomical devices the light has to be efficiently coupled into multimode fibres. Therefore the fibre parameters have to match the parameters of the input light. Firstly, the diameter of the fibre core has to

at least as big as the diameter of the object in focus. For a telescope the size of the focus d_{Focus} depends on the telescope diameter and its $F/\#$, the angular size of the focus θ_{Focus} and the size of the observed object. For a point-like object d_{Focus} can be calculated as follows:

$$d_{\text{Focus}} = \theta_{\text{Focus}} \cdot D_{\text{Telescope}} \cdot F/\# \tag{1.19}$$

Secondly the NA of the fibre has to be equal to or larger than the NA of the beam in the focus (usually expressed as $F/\#$) because a smaller NA leads to a loss of light.

The two conditions above can be summarised as a condition that the number of modes supported by the fibre has to be at least equal to the number of modes in the focus of the telescope, which can be calculated as follows (full derivation can be found in Appendix A) [31]:

$$N_m = \frac{V^2}{4} = \frac{\pi^2}{16} \cdot \left(\frac{\theta_{\text{Focus}}(\lambda) \cdot D_{\text{Telescope}}}{\lambda} \right)^2 \tag{1.20}$$

The number of modes strongly depends on the wavelength, as presented in Fig. 1.7. For $D_{\text{Telescope}} =$ 0.4 m, at a site with $\theta_{\text{Seeing}} = 1.5$ arcsec the number of modes at $\lambda = 1550$ nm is $N_m \approx 2$, whereas at $\lambda = 450$ nm, $N_m \approx 28$. For $D_{\text{Telescope}} = 4$ m, at the same seeing conditions, the number of modes are $N_m(1550\text{nm}) \approx 140$ and $N_m(450\text{nm}) \approx 2700$. For $D_{\text{Telescope}} = 10$ m the number of modes are $N_m(1550\text{nm}) \approx 865$ and $N_m(450\text{nm}) \approx 16{,}800$.

1.2.5 Focal ratio degradation

In a perfect, straight fibre the light emerges at the same focal ratio $F/\#$ as it enters, however due to minor imperfections in the fibre the light emerges at a larger angle (lower focal ratio) than the input beam as shown in Fig. 1.8 and Fig. 1.9, hence the name focal ratio degradation (FRD). The main origin of FRD is the mechanical deformations of the fibre cylindrical geometry, such as macro- and micro-bends in the fibre [32]. These deformations result in the transfer of energy from one mode to another, which over the length of a fibre causes FRD. Obviously, the energy cannot be transferred to another mode in single-mode fibres, therefore FRD is present only in multimode fibres. It is

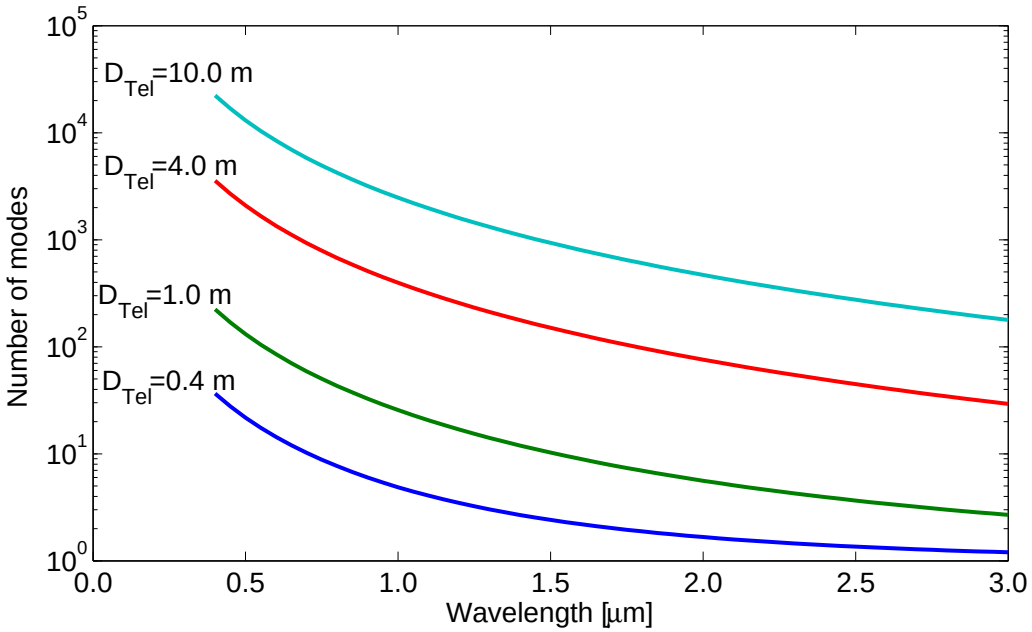

Figure 1.7: Number of modes as a function of wavelength for $\theta_{\text{Seeing}} = 1.5$ arcsec calculated for telescope diameter (D_{Tel}) of 0.4 m, 1.0 m, 4.0 m, and 10.0 m.

worth pointing out that the FRD is not present when the core of the fibre is fully illuminated and its NA is fully filled. However, due to the tolerances on fibre core diameter and Δn, errors in the telescope guiding, and tolerances on instrument optics, the astronomers choose to under-fill the optical fibre to maintain the highest throughput even for the price of FRD.

An optimally coupled spectrograph has a collimator designed to match the telescope focal ratio [33]. When a multimode fibre is introduced between the telescope and the spectrograph, the beam emerging from the fibre overfills the collimator aperture, which causes light loss. The size of the collimator can be increased but this increases the size of the pupil and all the dispersive elements, hence the cost.

FRD can be triggered by three factors: (i) deformations of the fibre cylindrical core produced during the fibre drawing process, (ii) mechanical stresses and micro-bend on the fibre during the application of the buffer coating as well as later in the fibre use, and (iii) fibre end-face scattering. It is important for the manufacturers to control the fibre drawing environment to reduce the non-uniformities along the fibre.

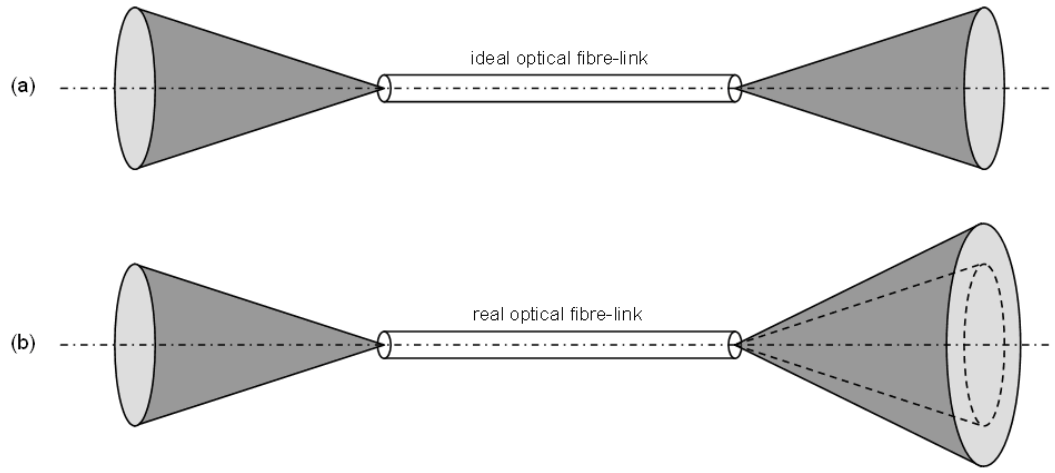

Figure 1.8: Schematic illustration of focal ratio degradation. The top figure (a) shows an ideal fibre with no FRD losses, whereas figure (b) represents a real fibre with a wider output cone than its respective input cone. Image courtesy: Tobias Feger.

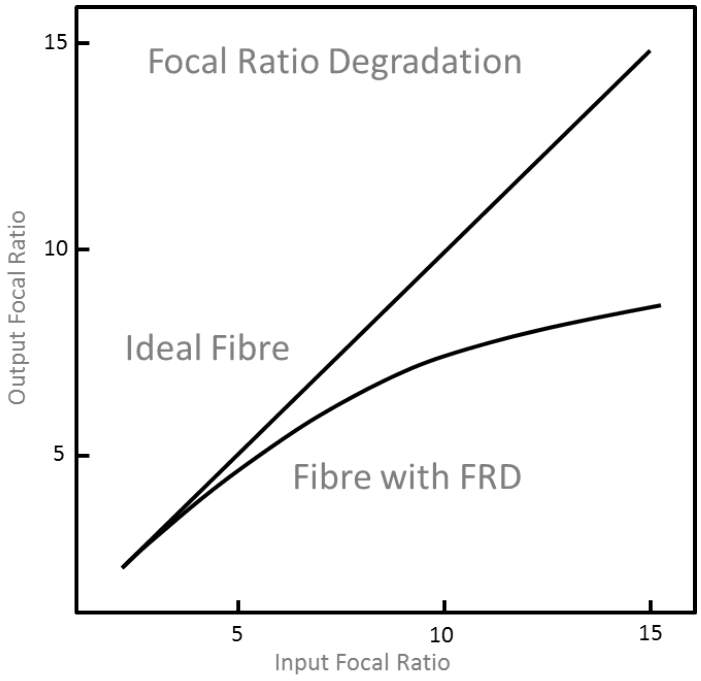

Figure 1.9: Plot showing typical focal ratio degradation for a single multimode optical fibre (NA=0.25) as a function of input focal ratio. Image courtesy: Gemini Observatory.

Further, mechanical stress on the fibre can deform the fibre shape and induce additional micro-bending, hence increase the FRD. Mechanical parts such as fibre jackets and fibre connectors can apply stress on the fibre. Special care with the fibre cabling and connectorising has to be taken to minimise the FRD effect [34].

1.2.6 Image scrambling

There are two types of image scrambling: (i) azimuthal and (ii) radial. Azimuthal scrambling means that the intensity in the output is symmetric about the fibre axis. The degree of radial scrambling describes the constancy of the output beam as the input image is moved across the fibre core [33]. Azimuthal scrambling is essentially perfect and nearly complete in step-index, multi-mode fibres, while the radial scrambling is in most cases incomplete.

When the radial scrambling is incomplete, variations in illumination on the entrance fibre result in a variation of the output spot profile, as illustrated in Fig. 1.10. In astronomy such variations occur due to inaccurate telescope-guiding or seeing fluctuations [35]. The instability of the PSF on the detector is one of the key limitations in the accuracy of radial velocity measurements [36], as it causes radial velocity shift.

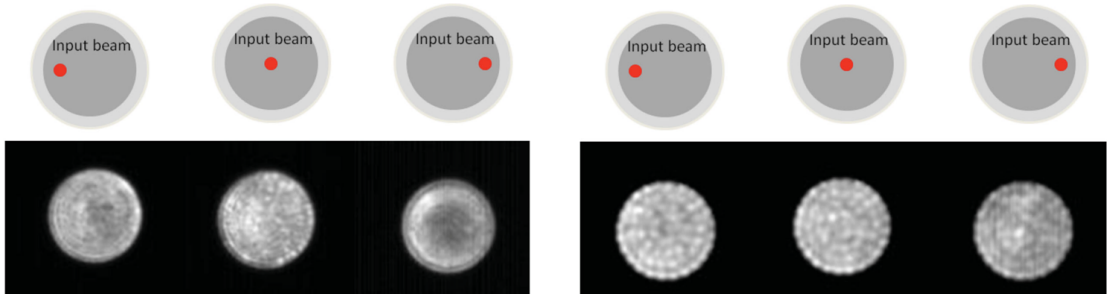

Figure 1.10: Illustration of (a) bad and (b) good radial scrambling. The top images show the input point source position relative to the centre of the fibre input and the bottom images illustrate the output near-field patterns [37].

To increase image scrambling, several solutions have been proposed. One of them is to use a double-fibre scrambler [38], which incorporates a pair of fibres coupled together by a pair of microlenses, separated by their common focal length. Another solution

consists of mechanical scramblers, which squeeze the fibre with small bendings [39, 40]. Although both solutions increase the scrambling gain of the fibre, they introduce extra losses and more complexity in the system. Connes et al. [41] noted that a single-mode fibre is a perfect scrambler. As mentioned in Section 1.2.2 single-mode fibres permit the propagation of only one spatial mode and therefore act as perfect single-mode spatial filters. Their output beam is quasi-Gaussian and preserves no memory of the input beam geometry.

1.2.7 Spectral modal noise

Spectral modal noise is an interference effect between various modes at the multimode fibre output, occurring when light of narrow bandwidth is propagating in the fibre [42]. It results in an undesired modulation of the intensity, forming a speckle pattern at the fibre output. The contrast of the speckle pattern is higher for high coherence light (narrow bandwidth) than for lower coherence light (wider bandwidth) [43]. This means that when the fibre is used to feed a high-resolution spectrograph, the resulting PSF is dominated by the speckle pattern, as shown in Fig. 1.11. The effect cannot be easily removed by flat-fielding (division by a reference spectrum) because the intensity distribution is subject to any change in the fibre conditions, such as stress and temperature and any small changes in the fibre illumination [44]. The instabilities limit the achievable signal-to-noise ratio of high resolution spectroscopic measurements.

The solution that is currently used to mitigate modal noise is the use of fibre shakers near the fibre exit. Fibre shakers continuously agitate the fibre during the exposure at a period of agitation much shorter than the exposure time [44]. The detected signal is a sum of the multiple speckle patterns therefore it appears to be smoothed. Of course this modal noise does not exist in single-mode fibres.

1.2.8 Fibre Bragg gratings

Fibre Bragg gratings (FBG) act as selective filters. They consist of a periodic modification of the refractive index along the core of the optical fibre as depicted in Fig. 1.12.

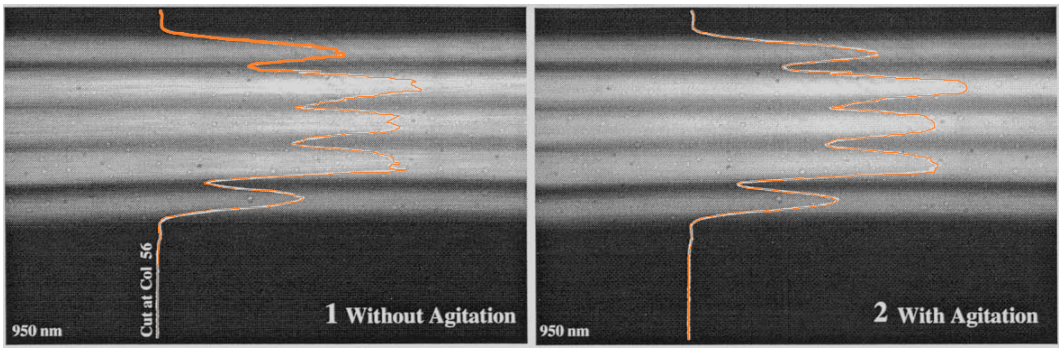

Figure 1.11: Image of the spectra and transverse profiles with and without fibre agitation (spectral direction is along the horizontal axis; the lines profiles were highlighted to make them more visible). The structure in the spectrum with the non-agitated fibre comes from modal noise. The relatively high frequency of the fibre agitation smoothes out the spectrum [44].

The light undergoes weak Fresnel reflection from each of the index modifications as it propagates through the FBG. The backwards-propagating waves interfere with each other in such a way that there is constructive interference for a narrow range of frequencies. All the other frequencies propagating backwards undergo destructive interference and are therefore transmitted by the FBG. As a result, a narrow range of frequencies is reflected backward due to periodic index modulation and hence the FBG act as fibre-based dichroic mirrors. They find numerous applications such as wavelength filters in telecommunication systems, cavity mirrors in fibre laser systems or sensors and dispersion compensators.

The reflected wavelength (also called Bragg wavelength) can be calculated using the following Bragg equation:

$$\lambda_{\mathrm{B}} = 2 \cdot n_{\mathrm{eff}} \Lambda, \tag{1.21}$$

where λ_B is the Bragg wavelength, n_{eff} is the effective refractive index, and Λ is the period of the refractive index modulation. As can be seen the Bragg wavelength depends on the effective refractive index. This means that each mode propagating in a multimode fibre would be reflected at a different Bragg wavelength. As a result, the single-wavelength, narrow-bandwidth FBG can be realised only in single-mode fibres.

The Bragg wavelength in a FBG is highly influenced by the ambient conditions,

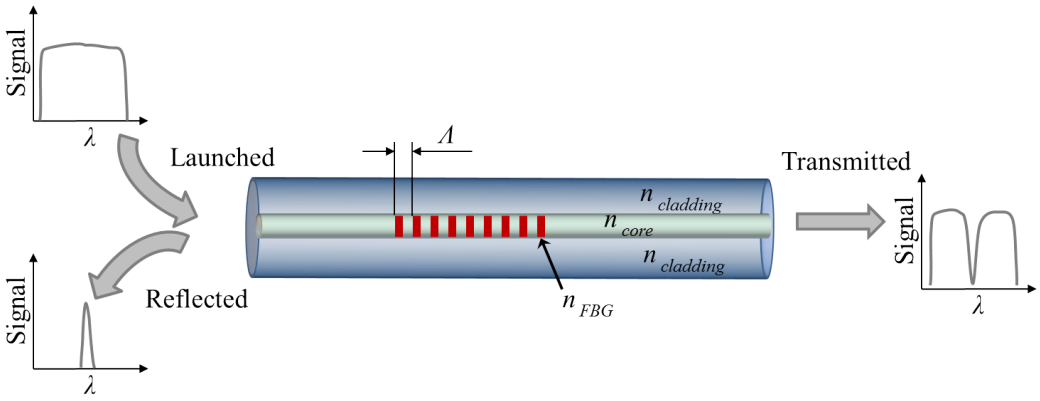

Figure 1.12: Schematic diagram of the fibre Bragg grating. Λ is the grating period, n_{cladding}, n_{core}, n_{FBG} are the refractive indices of the cladding, core and grating periodic modifications, respectively.

such as temperature and stress. These two factors impact the length of the fibre, which in turn changes the period of the refractive index modulation. On one hand it makes the FBGs excellent sensors but the effect is undesired when the Bragg wavelength has to be kept stable. To prevent this effect the FBGs have to be temperature and stress stabilised or placed in athermal packaging.

1.3 Photonic lanterns

As was shown in Sections 1.2.5, 1.2.6, and 1.2.7 multimode fibres are not ideal for feeding light into a spectrograph, whereas single-mode fibres possess excellent properties. However, it is impossible to efficiently inject the seeing-limited light into a single-mode fibre, unless the telescope is operating with adaptive optics that can match the size of the point spread function (PSF) to the diameter of the fibre. On the other hand, multimode fibres are perfect for collecting the incoherent seeing-limited light. A device which can combine the light coupling efficiency of a multimode fibre with the properties of single-mode fibres could greatly enhance the sensitivity and precision of the spectroscopic measurements, and allow photonic technologies to be employed, while reducing the footprint of the astronomical spectrograph.

It is impossible to couple hundreds of modes of a multimode fibre into one mode

in a single-mode fibre without huge loss. This fact is prohibited by the second law of thermodynamics – it would decrease the number of degrees of freedom and hence the entropy. Nevertheless it is possible to couple the light into another multimode system which has at least as many degrees of freedom. This idea has been successfully realised and experimentally demonstrated in a device called a *photonic lantern* in 2005 by Leon-Saval et al. [7]. The name photonic lantern originates from its passing resemblance to a Chinese lantern, as depicted in Fig. 1.13. The primary motivation for the photonic lantern came from a device which would utilise FBG on a telescope for the suppression of atmospheric OH lines [45, 46].

In general, the photonic lantern consists of an array of single-mode waveguides on one end and a multimode waveguide on the other end (Fig. 1.13a). The multimode waveguide is created by bringing together single-mode waveguides, so that cross-talk can occur. In a fibre photonic lantern it is realised by placing the fibres in a lower refractive index tube and slowly tapering it down. As the size of the core of the single-mode fibres reduces along the taper section it loses its ability to confine the light. The propagating light spreads out to the cladding and becomes confined by the lower refractive index tube. The fused fibres effectively act as a multimode fibre [47]. Figure 1.13 shows the concept of a photonic lantern device and a back-to-back device with inserted FBGs and a multi-core fibre photonic lantern with the FBGs.

1.3.1 Photonic lantern requirements

There are two essential requirements for creating a low-loss photonic lantern: (i) mode number preservation between the sections and (ii) slow, adiabatic transition between the sections [47]. A low-loss coupling from one multimode system into another multimode system is possible if the second system supports at least as many modes, i.e. $N_{m1} \leq N_{m2}$ as shown in Fig. 1.14. For a photonic lantern device it means that the number of modes supported in the multimode input has to be less than or equal to the number of single-mode cores. For a back-to-back device, the third section has to support at least as many modes as the middle one, $N_{m2} \leq N_{m3}$. Allowing N_m to increase between the input and the output leads to focal ratio degradation. To avoid this effect

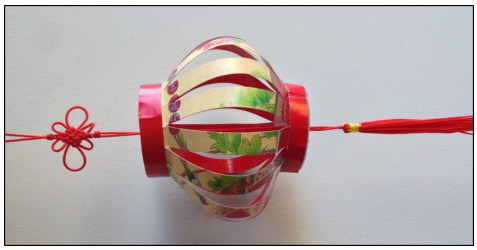

(a)

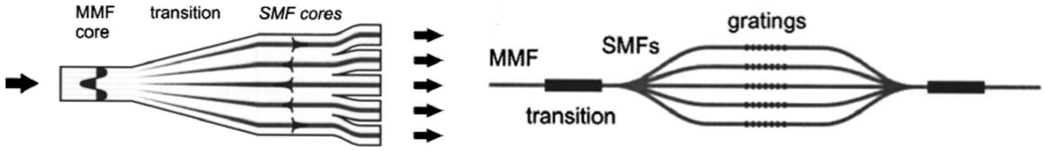

(b) (c)

Figure 1.13: (a) Picture of a Chinese lantern. (b,c) Schematic diagram of (b) a fibre photonic lantern (c) a back-to-back photonic lantern with the FBGs in the single-mode section [7].

ideally the number of modes is the same for all section, i.e. $N_{m1} = N_{m2} = N_{m3}$.

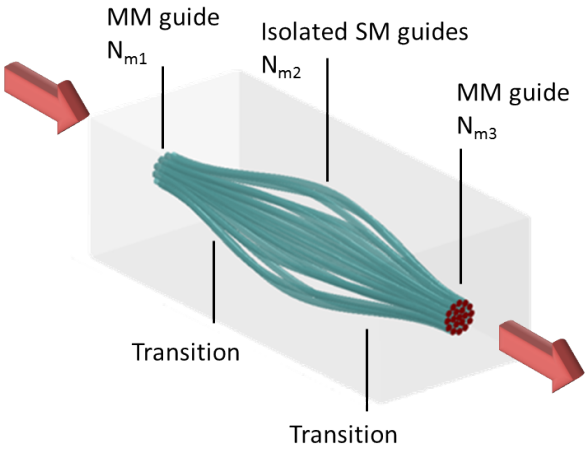

Figure 1.14: Schematic illustration of the back-to-back photonic lantern.

The second requirement is the adiabatic transition between the multimode and single-mode sections; adiabatic here refers to the gradual transitions required to ensure that there is effectively no energy loss from the photonic circuit. Hence, each mode in the multimode section evolves into a super-mode in the single-mode section, and vice versa, without coupling into cladding or radiation modes [48]. In a physical device the

overall structure of the photonic circuit changes along the transition but the energy distribution among the local modes remains the same [49]. The condition for the adiabatic transition can be fulfilled by avoiding sudden changes in the geometry of the waveguides, which is achieved practically when the waveguides are sufficiently long and slowly varying. The concept of adiabatic coupling in step-index fibres is depicted in Fig. 1.15. A sudden change in the mode field diameter of the supported mode due to reduction of the fibre core diameter results in coupling into cladding modes and hence energy loss (Fig. 1.15a). In contrast, slow reduction of the core diameter allows the mode to gradually reduce its diameter and it efficiently couples into the smaller core (Fig. 1.15b).

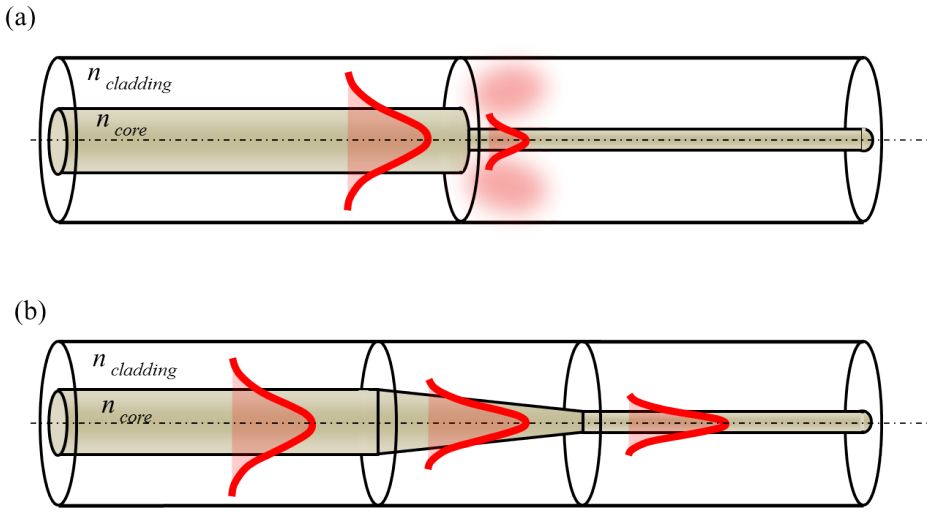

Figure 1.15: Schematic illustration of (a) non-adiabatic and (b) adiabatic coupling between two fibres. The fibres are assumed to be step-index, with the same refractive index contrast, different core diameters and different mode field diameters. When coupling the light directly from a larger to a smaller core, the mode cannot suddenly 'shrink' and part of the light is coupled into cladding modes, hence producing the energy loss (a). As a solution, a gradual core diameter change in a form of a taper is introduced to perform a slow mode field diameter reduction with effectively no energy loss (b).

In most photonic lanterns, light launched into the multimode end couples into a set of non-degenerate modes in the multimode section and then into a set of degenerate modes in the single-mode section in a non-deterministic fashion. However, recent works

[50] show that it is possible to determine the multimode - single-mode coupling and match the modes.

The mode distribution and evolution in the photonic lanterns presented here will be described in Section 3.3. The study on the adiabatic transition will be presented in Section 3.5.1.

1.3.2 Fibre photonic lantern

There are two main approaches to the fibre photonic lantern fabrication. In the first one a bundle of standard single-mode fibres is inserted into a low refractive index capillary tube. The tube with fibres is then heated up, tapered down and fused into a solid glass element to form a multimode fibre on one end while keeping the isolated single-mode fibres on the other end, as shown in Fig. 1.16. The FBGs and another photonic lantern can then be spliced to each of the single-mode fibres as shown in Fig. 1.13 b) [7, 51]. Up to now several devices of high throughput fabricated via this technique have been reported: a 7 channel photonic lantern of 0.32 dB losses (93 % throughput) [9] and a 61 channel back-to-back (MM-SM-MM) photonic lantern of 0.76 dB losses (84 % throughput).

The GNOSIS instrument [46] employed photonic lanterns for OH line suppression. It used seven pairs of 1×19 photonic lanterns back-to-back (MM-SM-MM), which were connected to complex fibre Bragg gratings in the middle that suppress 103 atmospheric lines between 1470 nm and 1700 nm.

The main advantage of this technique is that the multiple FBGs can be fabricated independently in single-mode fibres, producing devices of the same spectral characteristics. On the other hand, this manufacturing technique is labour consuming, expensive and leads to a bulky instrument, thus an alternative is desired.

A second approach uses multi-core fibres. Multi-core fibres are bundles of physically independent single-mode fibres, which are well separated from each other eliminating fibre cross-talk. In telecommunications each of the single-mode fibres is individually jacketed to avoid any cross-talk. However, a multi-core fibre can be also realised by placing the single-mode cores in one big common cladding but with spacing large

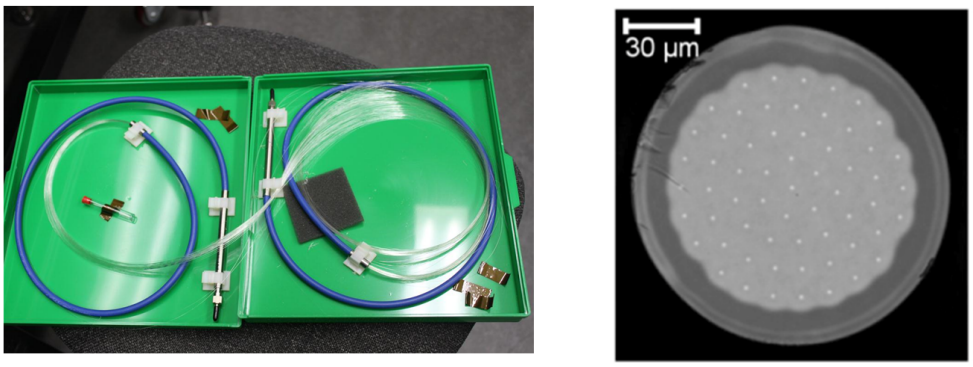

(a) (b)

Figure 1.16: (a) Picture of the back-to-back (MM-SM-MM) 19 channel fibre photonic lantern manufactured by NKT Photonics. (b) Microscopic image of the multimode end of the 61 channel fibre photonic lantern [9].

enough to reduce the cross-talk. Such fibres are used to fabricate photonic lanterns based on multi-core fibres (Fig. 1.17). The ends of a multi-core fibre are inserted into a low-index jacket and tapered down to create multimode fibre ports. The FBGs are simultaneously inscribed across the cores of the single-mode section of the multi-core fibre as shown in Fig. 1.17c [48, 52, 53]. Despite the simplification of the photonic lantern fabrication process the inscription of uniform FBGs across all the cores has proven to be difficult, and the resulting spectral response of devices fabricated so far has been insufficient for astronomical applications.

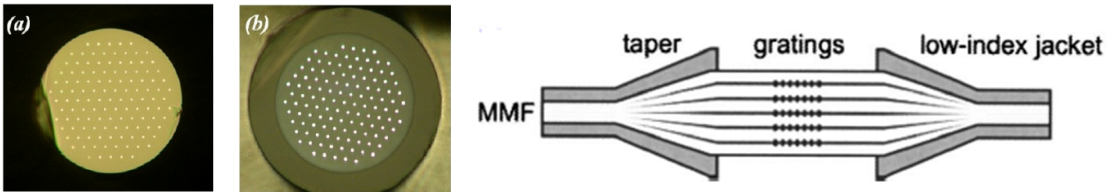

(a) (b) (c)

Figure 1.17: Microscopic image of a multi-core fibre cross-section (a) uncoated fibre, (b) jacketed fibre [48]; (c) schematic diagram of multi-core fibre based photonic lantern with FBGs [48].

Although fibre based photonic lanterns offer high performance, they are limited in terms of scalability. As shown in Section 1.2.4 the number of modes needing to

be supported in the telescope focus scales as $\sim 1/\lambda^2$. A device which operates in the visible wavelength range on a 4-metre class telescope has to support $\sim$ 2000-3000 modes (Fig. 1.7). Such devices are not really practical because the fibre photonic lantern is bulky, temperature sensitive, and complex to make and handle.

1.3.3 Direct-write photonic lanterns

Thomson et al. [54] proposed that ultrafast laser inscription could be used to fabricate three-dimensional (3D) photonic lanterns in a monolithic device (Fig. 1.18). In this technique ultrashort laser pulses are focused in a dielectric material such as glass. If sufficient power is delivered the material can be locally modified, which results in a permanent refractive index change [55]. By translating the glass sample along three axes, a track of index change can be inscribed which acts as an optical waveguide. The waveguides can in principle be packed arbitrarily close, which allows for the miniaturisation of devices compared to fibre-based technology. Thomson et al. [10] fabricated the first integrated photonic lanterns that supported 16 modes at 1550 nm. The back-to-back devices exhibited losses too high to be used in astrophotonics (5.7 dB of insertion loss, throughput of 27%), but they showed that the loss for a multimode to single-mode transition could be $\sim$ 2.0 dB (63% throughput), demonstrating the feasibility of the approach.

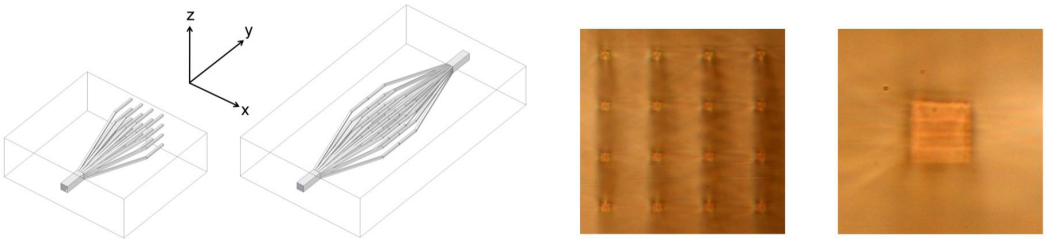

(a) (b)

Figure 1.18: (a) Sketches of the 1×16 multimode to single-mode transition (left) and back-to-back integrated photonic lantern (right); (b) microscopic images of the 4×4 single-mode (left) and multimode (right) ends of integrated photonics lanterns by Thomson et al. [10].

2

Femtosecond direct write technique background

Femtosecond micromachining holds great potential for fabricating a wide range of photonic circuits inside bulk glasses without damaging the surface, with applications in sensing, laser sources, lab-on-chip and more. The ultrashort pulses possess unique properties enabling the observation of physico-chemical processes occurring on a timescale of < 1 ps. The femtosecond laser pulse can reach very high intensities of ~ 10 TW/cm^2, which, when tightly focused in a dielectric material, results in extremely high and brief energy concentration. The high intensity results in a nonlinear process that leads to the deposition of the energy in a highly localised region of bulk glass. The high energy deposition causes a material breakdown, which locally modifies the material structure.

The creation of a laser-induced breakdown resulting in microstructures in transparent fused silica glass was demonstrated for the first time in 1994 [56]. Soon after that Glezer et al. [57] fabricated submicrometer-diameter voids and areas of very high refractive index in fused silica. They showed that the femtosecond pulses can lead to explosive expansion in bulk material. The first smooth refractive index modification was shown by Davis et al. [58] in 1996. They reported a highly localised, elliptical-shape refractive index modification in various types of bulk glasses (high-silica, borate, soda lime silicate, and fluorozirconate) using a 810 nm Ti:sapphire laser that emits 120 fs, with a 200 kHz repetition rate and an average power of 975 mW. The samples were moved on translation stages creating lines of positive refractive index change (0.015 for a silica glass and 0.010 for a Ge-doped silica glass) acting as optical waveguides [58]. What is more, they identified this technique as the opportunity for realising truly 3D optical circuits in bulk glasses. Since this discovery, femtosecond waveguide fabrication has drawn huge attention and a large number of integrated devices have been fabricated.

Femtosecond direct write is now a common fabrication technique of fabrication for various photonic circuits, such as waveguide couplers [59], Fresnel lenses [60], waveguide Bragg gratings [61], waveguide lasers [62], photonic quantum circuits [63], astrophotonics circuits [10] and sensors [64]. Optical structures can be written in many types of dielectric materials. The most popular materials are common glasses, typically fused silica [61], borosilicates and aluminosilicates [65, 66], soda-lime [64], as well as exotic glasses, such as phosphates [67], chalcogenide glasses [68], fluorozirconates [69] and crystals, like lithium niobate [70], silicon [71], and sapphire [72].

In the first part of this chapter the interaction between the laser light and material is discussed, summarising the physico-chemical processes occurring in the glass under the ultrashort irradiation, and the three main types of modifications that are created depending on the laser pulse energy. The second part discusses various aspects of fabrication: writing geometry, laser repetition rate, translation speed and substrate material. These aspects are most important for the work presented here.

2.1 Laser interaction with transparent dielectrics

When a femtosecond laser beam of high enough intensity is focused into a dielectric material an optical breakdown can be observed [55]. Electrons in the material absorb the photon energy and, once excited, they transfer energy to the lattice, leading to a permanent material modification. There are three main steps in the process: the generation of the free electron plasma, energy relaxation, and modification of the material [73].

2.1.1 Free electron plasma generation

Depending on parameters such as the laser power and the pulse duration there are different absorption processes leading to the generation of a free electron plasma, namely multiphoton ionisation, tunnelling ionisation, and avalanche ionisation. Stuart et al. [74, 75] derived a rate equation for the evolution of the free electron density $N(t)$ in a dielectric material exposed to intense laser radiation [75]:

$$\frac{N(t)}{t} = \sigma_m I(t)^m + \alpha I(t) N(t), \tag{2.1}$$

where $I(t)$ is the intensity of the laser pulse, σ_m is the m-photon absorption cross-section, m is the number of electrons required to bridge the bandgap, and α is the avalanche coefficient. The first parameter in Eq. 2.1 scales the laser intensity exponentially with the number of photons m and represents the non-linear photoionisation, including multiphoton absorption and/or tunnelling photoionisation. The second parameter in Eq. 2.1 depends linearly on laser intensity and represents the avalanche photoionisation.

From Eq. 2.1 we can see that the non-linear photoionisation is the main factor creating the free space electrons $N(t)$ for materials with higher bandgap energies which are illuminated with short laser pulses ($<$ 10 fs for fused silica, 100 fs for borosilicate glasses) [75]. At longer pulse durations and for materials with higher bandgap energies, the contribution from the avalanche ionisation becomes significant as well.

2.1.2 Nonlinear Photoionisation

Multiphoton ionisation occurs when an electron in the valence band absorbs multiple photons simultaneously and gets promoted to the conduction band (Fig. 2.1a) [73]. The number of photons m needed to promote the electron depends on the energy gap of the material and the energy (i.e. frequency or wavelength) of the photon. It has to satisfy the condition $mh\nu > E_g$, where m is the number of photons, h is Planck constant, ν is the frequency of light, and E_g is the material bandgap energy.

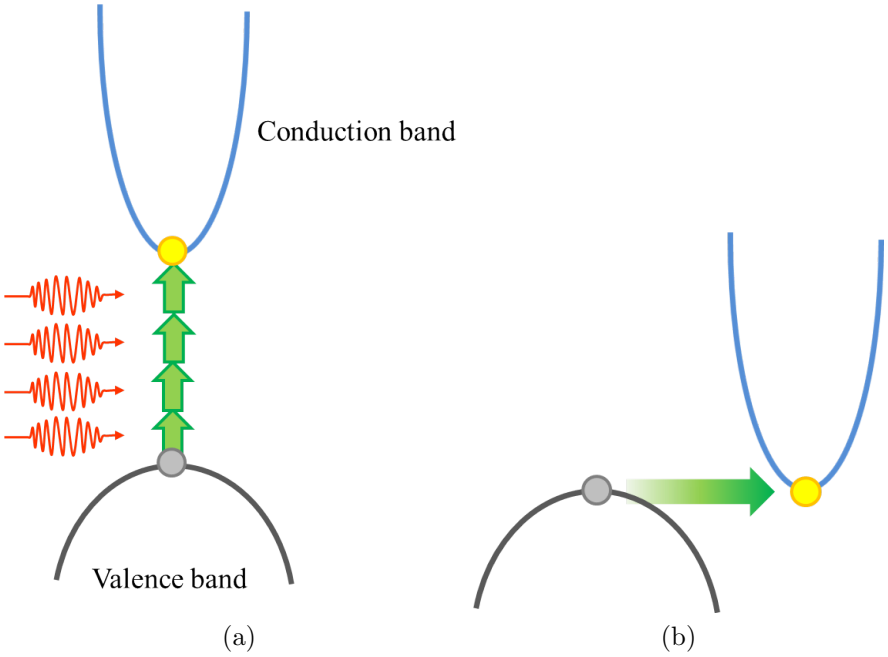

Figure 2.1: Illustration of a) multiphoton photoionisation, b) tunnelling ionisation.

When using a laser beam of 800 nm the typical number of photons required is $m = 2$ for a phosphate glass, $m = 3$ for BK7 or $m = 6$ for fused silica [76].

Multiphoton ionisation is the dominant process for a laser with low intensity and high frequency. However at high intensity and low frequency the dominant process is *tunnelling ionisation*. Tunnelling ionisation (Fig. 2.1b) occurs when the strong field distorts the band structure and reduces the bandgap; the electron tunnels through the potential barrier between the valence and conduction bands.

The relative dominance of multiphoton and tunnelling ionisation is described by

the Keldysh parameter [77]:

$$\gamma = \frac{\omega}{e}\sqrt{\frac{m_e c n \epsilon_0 E_g}{I}}, \tag{2.2}$$

where ω is the frequency of the laser field, e is the electron charge, m_e is the effective electron mass, c is the speed of light, n is the refractive index of the glass, ϵ_0 is the permittivity of free space, and I is the laser intensity. When $\gamma \gg 1$ multiphoton ionisation dominates and when $\gamma \ll 1$ tunnelling ionisation dominates. The typical γ values are $\gamma \sim 1$, indicating a significant contribution from both non-linear ionisation processes [78].

2.1.3 Avalanche photoionisation

Avalanche photoionisation is a two stage process, as shown in Fig. 2.2. First, the free electron in the conduction band absorbs the laser light. After absorbing several photons and gaining more energy than the bandgap energy, the redundant energy can be transferred to another electron in the valence band via impact ionisation. In the second stage, the electron is then promoted to the conduction band creating two free electrons at the conduction band minimum. Avalanche ionisation initially requires free seed electrons, which can be provided by thermally excited carriers, easy ionisable impurities and defect states, or being created by multiphoton or tunnelling photoionisation. The process can be repeated as long at the laser irradiation is present [73]. The effect of the process becomes significantly greater for longer laser pulse duration and for material with greater bandgap energies [79].

2.1.4 Relaxation and material modification

Non-linear photoionisation and avalanche photoionisation create a free electron plasma. Electrons transfer energy to the material lattice via electron-phonon coupling [80]. The transferred energy modifies the glass causing structural change. The type of modification depends on the laser parameters (wavelength, pulse energy, pulse duration, pulse repetition), the exposure parameters (polarisation, NA of the focusing objective, scan

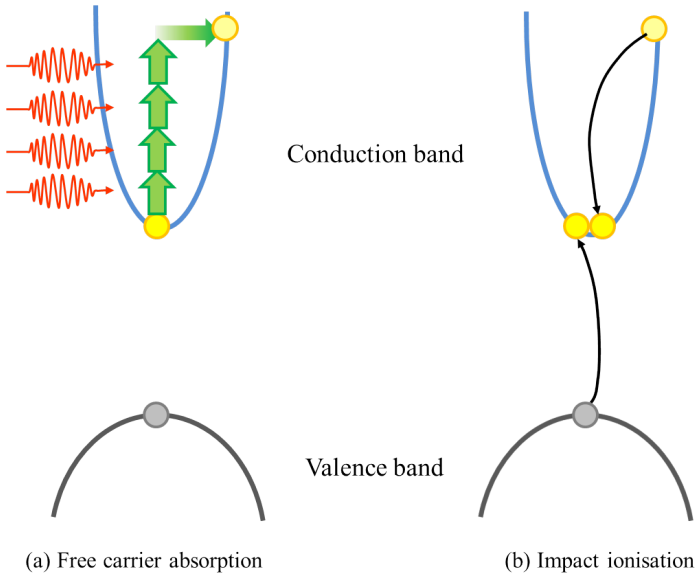

Figure 2.2: Illustration of avalanche ionisation: free carrier absorption followed by impact ionisation.

speed) as well as the material properties (e.g. bandgap energy, thermal conductivity) [73].

Depending on the amount of irradiation delivered to the material three types of glass modification can be identified:

- a very low pulse energy below the modification threshold results in no damage;
- a low pulse energy just above the modification threshold results in a positive or negative refractive index change;
- an intermediate pulse energy forms a birefringent refractive index change;
- a high pulse energy forms empty voids.

2.1.4.1 Refractive index change

A low laser pulse energy (just above the threshold for fused silica) during direct-write inscription can create a positive or negative refractive index change Δn. A smooth and uniform positive refractive index modification drawn along the glass sample creates a low propagation loss optical waveguide. The exact process of the refractive index change creation is not yet well understood but several explanations have been proposed.

Poumellec et al. [81] suggested that the redistribution of the material, causing densification and strain are the origins of the positive refractive index change. This theory has been confirmed by Chan et al. [82], using Raman microscopy to observe an increase of 3- and 4-membered silicon-oxygen rings in fused silica glass. This increase proves the densification of the glass in the focal volume.

Colour centres have also been correlated with the refractive index change. Two groups identified a creation of colour centres under IR femtosecond irradiation in laser modified region of boro-silicate and alkali silicate glasses [83] and fused silica [84]. However, Streltsov and Borelli [85] observed that the colour centres disappeared after annealing the waveguides in fused silica and a borosilicate glass, while the refractive index modification was still present. Later on, Dekker et al. [86] showed that for the Yb-doped phosphate glass, the colour centres contributed 15% to the overall induced refractive index change [86].

Little et al. [87] studied the influence of the IR 1 kHz and 5.1 MHz laser pulse repetition rate on the structure of borosilicate glass BK7 (Schott). In the kHz regime the positive refractive index change was attributed to an elevated population of non-bridging oxygen atoms, associated with colour centres and an increase in the molar refractivity of the glass. For the MHz regime a change of density was identified as the dominant mechanism of refractive index modification: densification leading to positive change and rarefaction leading to a negative change [87]. Fletcher et al. [88] observed the high-repetition rate laser pulses induced a change in the glass network (and refractive index), specifically the phosphor-oxygen bond length in a phosphate glass [88]. It has been also shown that high-repetition rate lasers can deliver enough thermal energy to induce migration of the elements of the lattice in the heated volume [89].

In short, it is currently understood that the smooth refractive index change induced by femtosecond laser radiation mostly comes from density change and colour centre creation. However, the relative contributions to the refractive index modification vary with the glass composition and laser exposure conditions [73].

2.1.4.2 Birefringent refractive index change

Intermediate laser pulse energies produce birefringent refractive index modification. Surdie et al. [90] was the first group to create permanent birefringent structures in bulk fused silica using a Ti:Sapphire laser, of 805 nm wavelength, 130 fs pulse duration, and 200 kHz repetition rate [90]. Subsequently, other groups showed a femtosecond laser polarisation dependency on the physical orientation of the nanostructures. Shimotsuma et al. [91] and Hnatovsky et al. [92] reported that the nanostructures exhibited an orientation perpendicular to the electric field vector of a linearly polarised laser beam in fused silica and silica glasses, as shown in Fig. 2.3. The birefringence originates from self-organised, oxygen rarified nanolayers of 20 nm width. Shimotsuma et al. [91] suggested that orientation of the nanostructures is caused by interference between the laser field and induced electron plasma wave.

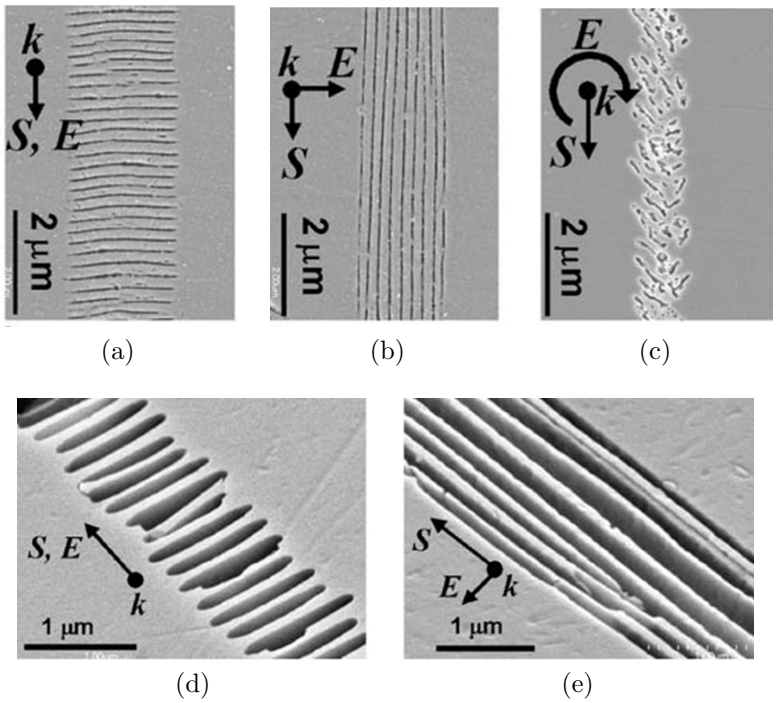

Figure 2.3: Scanning electron microscopy (SEM) images of the nanogratings fabricated in fused silica with laser linear polarisation and (a) the laser beam parallel to the fabrication direction, (b) perpendicular to the fabrication direction, (c) circular polarisation. SEM images of the etched nanogratings with the laser polarisation (d) parallel and (e) perpendicular with respect to the translation direction [92].

Nanostructure fabrication is limited to a narrow inscription parameter space, e.g. Hnatovsky et al. [92] were able to create nanogratings only for the medium NA focusing objective lenses. Furthermore, so far the nanostructures have been reported in silica [91, 93], fused silica [92], phosphate glasses [94], borosilicate glasses (Borofloat 33, BK7) [95] and silica ULE glass [95]. Most of the nanostructures have been fabricated in the kHz repetition rates, but they have also been observed under high repetition rate irradiation [94, 95].

The main potential application of this discovery is the fabrication of microchannels for microfluidics [92, 93]. Nevertheless, the birefringent devices can also be used for polarisation dependent devices such as holograms [96] and polarisation-dependent optical routers [97].

2.1.4.3 Empty voids

High energy laser pulses create empty voids in a material. When a laser beam of high pulse energy is focused with high NA objective lenses, a peak intensity larger than 10^{14} W/cm^2 can be easily achieved [73]. Such high intensities create a high intensity plasma in the glass. Before the energy can escape through diffusion or radiative recombination [98] the plasma transfers the energy to the lattice by heating it to $\sim 10^6$ K. This generates a high pressure ($\sim$TPa) , which far exceeds the Young's modulus of the material, generating a strong shock and rarefaction wave that results in the formation of a void surrounded by a shell of higher refractive index [99].

The main applications of the microvoids in bulk glasses are data storage [57], laser direct-written photonic crystals [100], waveguide Bragg grating in bulk glass [101] and fibre Bragg gratings in silica fibres [102].

2.2 Fabrication aspects

When fabricating optical waveguides with a femtosecond laser, there are several variables influencing the final outcome. It has been already shown in Section 2.1.4.1 that, depending on the laser pulse energy, it can create a smooth refractive index change,

birefringent structures or empty voids. The other characteristics of the fabricated waveguides depend on parameters such as the material in which the laser beam is focused, laser beam polarisation, laser wavelength, pulse duration, laser repetition rate and the translation speed of the stages. The following section will focus on the fabrication aspects which are most relevant for the work presented here.

2.2.1 Writing geometry

There are two standard configurations for writing optical waveguides with a femtosecond laser: transverse (perpendicular) and longitudinal (parallel) writing, as depicted in Fig. 2.4. In both cases the laser beam is tightly focused inside the bulk glass sample with an objective lens (Fig. 2.4a). The glass sample is placed on top of moving stages. By translating the stages and moving the position of the focus in the sample, the waveguides can be written.

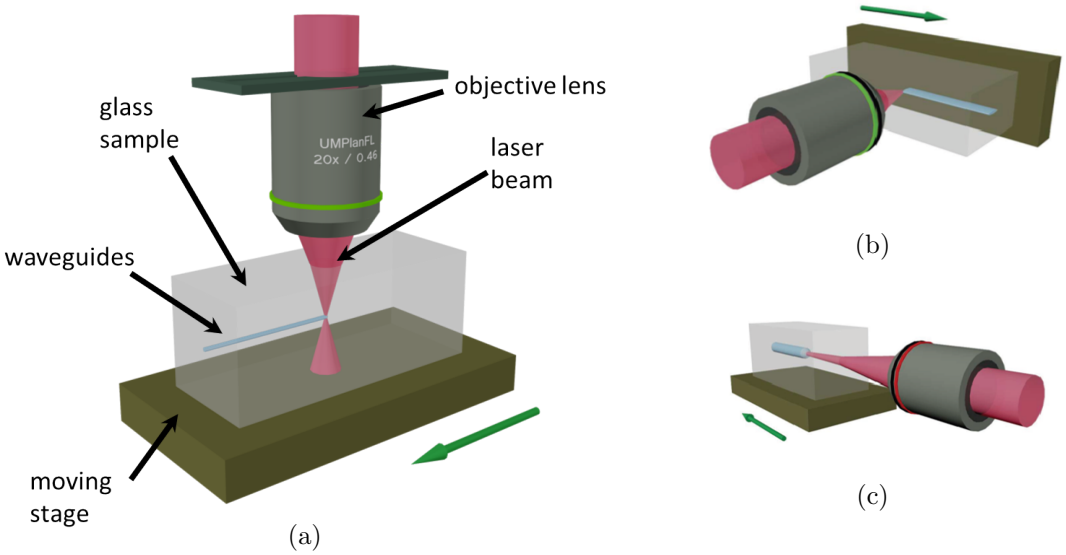

Figure 2.4: Illustration of direct-write technique: (a) & (b) perpendicular (transverse) configuration, (c) parallel (longitudinal) configuration. Image courtesy: Dr. Martin Ams.

In the longitudinal configuration Fig. 2.4c the sample is moved parallel to the incident laser beam, either towards or away from the laser focal spot. The resulting structures are cylindrically symmetric due to the transverse Gaussian-like energy profile

of the laser beam in the focus [73]. The length of the waveguides is limited by the working distance of the objective lenses, which would result in waveguides of only a few mm length when using a tightly focusing objective of high NA. To overcome this limitation, an objective of lower NA can be used, allowing for weaker focusing but requiring much higher laser power to reach the optical breakdown. However, the high laser power leads to self focusing. The self focusing results in an elongated filament, i.e. a region of localised laser pulses. The elongated filament extends the length of the waveguides up to several hundred microns [103] but requires a relatively slow (few microns per second) translation speed to achieve large enough refractive index modification, and prohibits the fabrication of curved waveguides. Poor confinement of the filament and long fabrication time make the longitudinal laser writing configuration less ideal. Instead, the transverse configuration is currently the most commonly used approach.

In the transverse configuration the glass sample is translated perpendicularly to the laser beam direction creating a permanent refractive index modification, as depicted in Fig. 2.4ab. In this case the objective working distance does not impose a limitation on the length of the waveguides, so in practice the waveguide length is limited by the sample length and/or the travel range of the stages. The working distance of the objective lens determines the maximum depth of the waveguides beneath the top face of the glass.

The only drawback of the transverse configuration is the elliptical shape of the laser beam focus which can cause an elliptical cross-section of refractive index modification. The laser focus depth is usually longer (between 2 and 6 times) than its width. This asymmetry results in an elongated, elliptical cross-section of the waveguide and thus an elliptical shape of the propagating mode. Coupling the light from the optical fibre into such an elliptical waveguide results in high coupling losses and birefringence. The geometry of the focus can however be reshaped to avoid the asymmetry. When operating in low-repetition rate laser systems (kHz), the main solutions are the use of a slit [104], multiscan technique [105], cylindrical lenses or spatial light modulator (SLM). When using a high-repetition rate (MHz) laser system, the waveguides are created by

heat diffusion and regardless of the focus shape the waveguides have a cylindrical cross-section, therefore the transverse configuration is preferable for the high-repetition rate regime.

2.2.2 Laser repetition rate

There are two working regimes in the fabrication of laser-written waveguides: low-repetition rate (< 100 kHz, athermal) and high-repetition rate ($>$ 100 kHz, usually several MHz, thermal). The distinction comes from the heat diffusion time in the glass ($\approx$1 µs [106]) and the time period between two consecutive laser pulses. If the time between the pulses is long enough (> 1 µs) that all the heat dissipates from the focus before the next pulse arrives, the system is operating in the low-repetition rate regime (Fig. 2.5a). If the the next pulse arrives before the heat dissipates (≤ 1 µs) then the system operates in the high-repetition rate regime. (Fig. 2.5b). At a low-repetition rate, the material cools down to the ambient temperature between the pulses and each of the pulses acts independently on the material, causing a repetitive modification. In the case of a high-repetition rate, the heat builds up with each pulse and the waveguides are created through cumulative heating. Figure 2.5 depicts both operation regimes.

At a low-repetition rate, the shape of the waveguide represents the shape of the laser focus. When the waveguides are fabricated in the transverse laser configuration, the resulting waveguides are of an elliptical shape. In order to get a circular shape, one of the common solutions proposed by Ams et al. [104] is to shape the beam by placing a slit before the focusing objective lens. Another method is the multi-scan technique [105, 107], wherein each of the tracks is slightly offset from its neighbours, so that in the end they create one relatively smooth square waveguide. Long heat diffusion time in the glass forces a slow translation speed of the stages and long fabrication time for the devices. A single scan, which is few mm long, requires a few minutes of fabrication time. If the refractive index change produced during the single scan is not high enough, then a single waveguide requires multiple scans. When fabricating complex structures of multiple waveguides and/or performing a parameter scan of the devices, the fabrication time requires tens of hours. In such cases the long fabrication

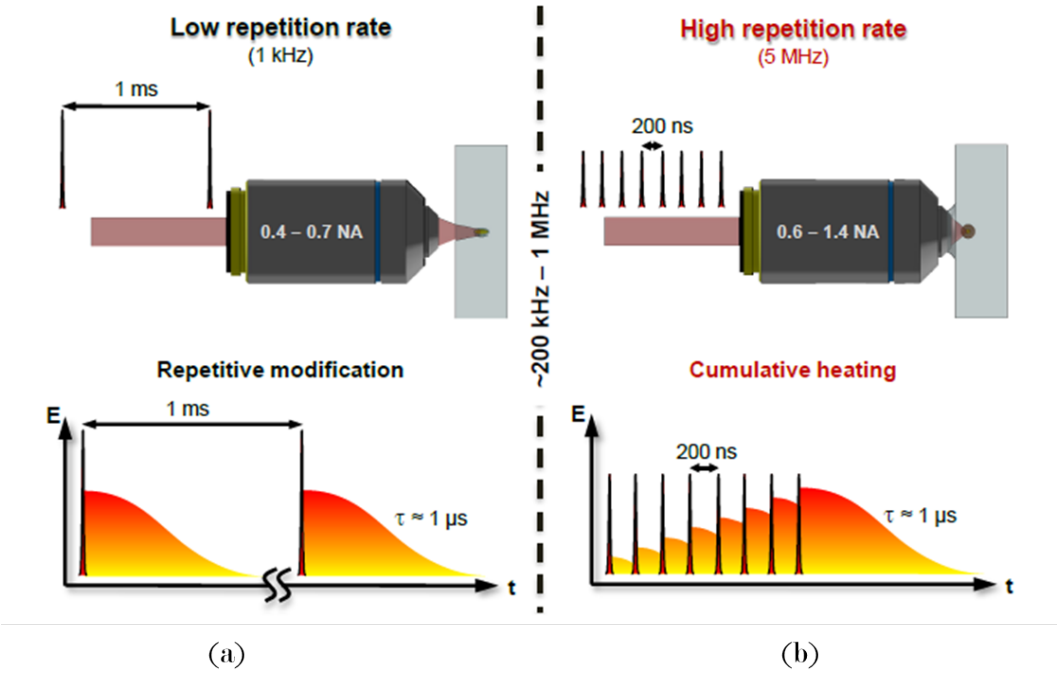

Figure 2.5: Illustration of the (a) low-repetition rate and (b) high-repetition rate regimes. Image courtesy: Dr. Simon Gross.

time is highly impractical as the alignment of the laser and the sample is very sensitive to external vibrations and temperature variations.

At high-repetition rate, the pulse period is shorter than the thermal relaxation time of the material. The heat in the sample builds up and melts the glass modifying the chemical structure of the glass. Once the laser irradiation is stopped, the modified structures freeze and become permanent. Schaffer et al. in 2003 [79] were the first to demonstrate the use of high-repetition rate (25 MHz) lasers in waveguide fabrication. They reported a tremendous increase in the waveguide size compared to the size of the focus, with a sub-micrometre-sized focal volume producing much bigger structures of $\sim$ 10-20 µm in diameter.

Waveguides can be written using both low NA (NA = 0.25) and high NA (NA = 1.25) focusing objective lenses when fabricating them at the high-repetition rate. However, to create the same refractive index contrast a low NA objective lens requires higher

laser pulse energy than a high NA lens. On the other hand a low NA objective lens has a longer working distance than a high NA objective lens so that the waveguides can be written within a larger depth range. The waveguides created with a low NA objective lens tend to be non-symmetrical (elliptical) compared to the waveguides fabricated with a high NA objective lens [108] leading higher coupling losses between the fibre and the waveguides. Overall, the choice of the NA of the objective lens depends on the available laser system and waveguides application. More detail on structures fabricated in the high-repetition rate regime is given in the next section.

2.2.3 Translation speed

Pulse energy and translation speed are the main factors affecting the size and the refractive index contrast of a waveguide during the writing process. Each glass behaves differently under femtosecond laser irradiation but the most common responses can be generalised and are presented below.

Eaton et al. [109, 66] studied the influence of the laser repetition rate and the irradiation dose on the size of the modified structures. They reported that the laser repetition rate strongly affects the cross-sectional size of the heat affected area. As shown in Fig. 2.6, the size of the index modification significantly exceeds the 2 µm laser spot size for repetition rate $>$ 200 kHz, manifesting the cumulative heating process. The irradiation dose (number of pulses) also changes the size of the modified structures. Figure 2.6 shows the modest size increase with increasing number of pulses in the low-repetition regime (100 kHz and 200 kHz). The size increase in the high-repetition rate (500 kHz and 1 MHz) is much stronger, again giving a strong evidence of the increased heat accumulation. The sensitivity of the high modification size to the irradiation rate gives the high-repetition rate regime huge flexibility in producing waveguides of wide range of sizes and refractive index changes.

The translation speed relates to the irradiation dose, meaning a slow translation speed produces a higher irradiation dose. The irradiation dose also affects the refractive index modification. In the case of the low-repetition regime the refractive index change increases with the number of laser pulses (Fig. 2.6). In the case of the high-repetition

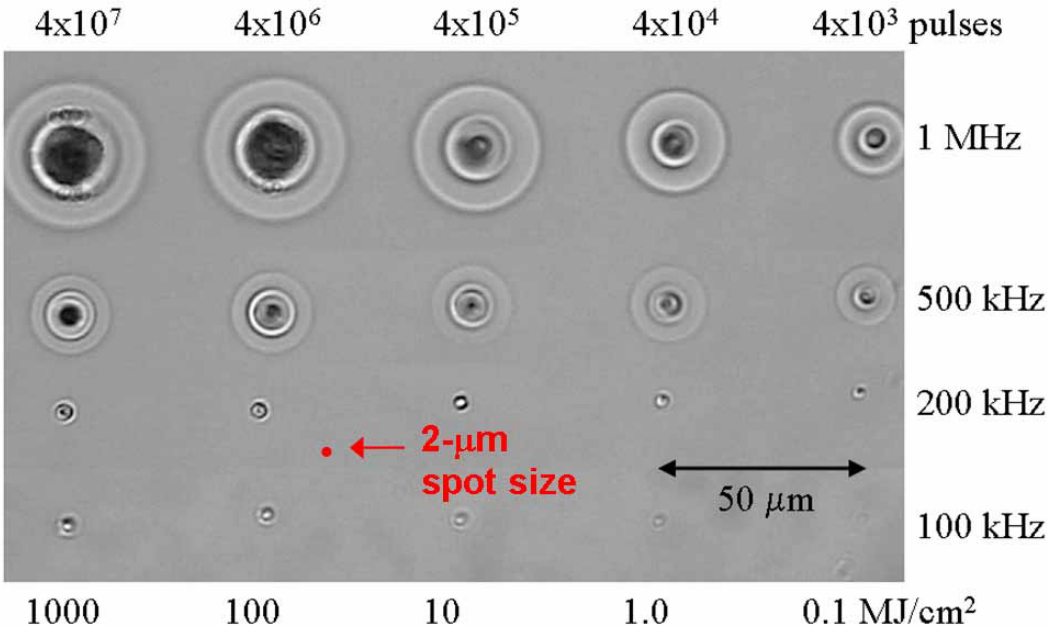

Figure 2.6: Microscopic images showing the cross-sections of the structures created in AF45 glass and the heat affected zones. The structures were written with 450 nJ energy from a 1045 nm femtosecond laser. Total pulse (top) and fluence accumulation (bottom) is shown for each column and the laser repetition rate is indicated for each row [109].

regime, not only the magnitude but also the profile of the refractive index change is affected [110]. When the number of pulses increases, the profile of the refractive index modification can exhibit regions (dips) lower than the base glass refractive index. Nolte et al. [111] showed that the bright central regions seen in the micrographs of the waveguides correspond to a positive index contrast, whereas the surrounding dark regions represent the areas of the negative index contrast (refractive index lower than the base glass refractive index) as seen in Fig. 2.6 and Fig. 2.7. This effect is a result of the variable temperature across the melted volume and non-uniform rapid cooling providing a non-uniform final density distribution through the glass [110, 66, 112].

Despite the complex geometry of the refractive index structure for most of the waveguides fabricated in the cumulative heating regime, the guided modes maintain a Gaussian-like profile (Fig. 2.8) allowing for efficient coupling between the waveguide and a fibre.

The cylindrical symmetry of the waveguides, fine control on the waveguide size

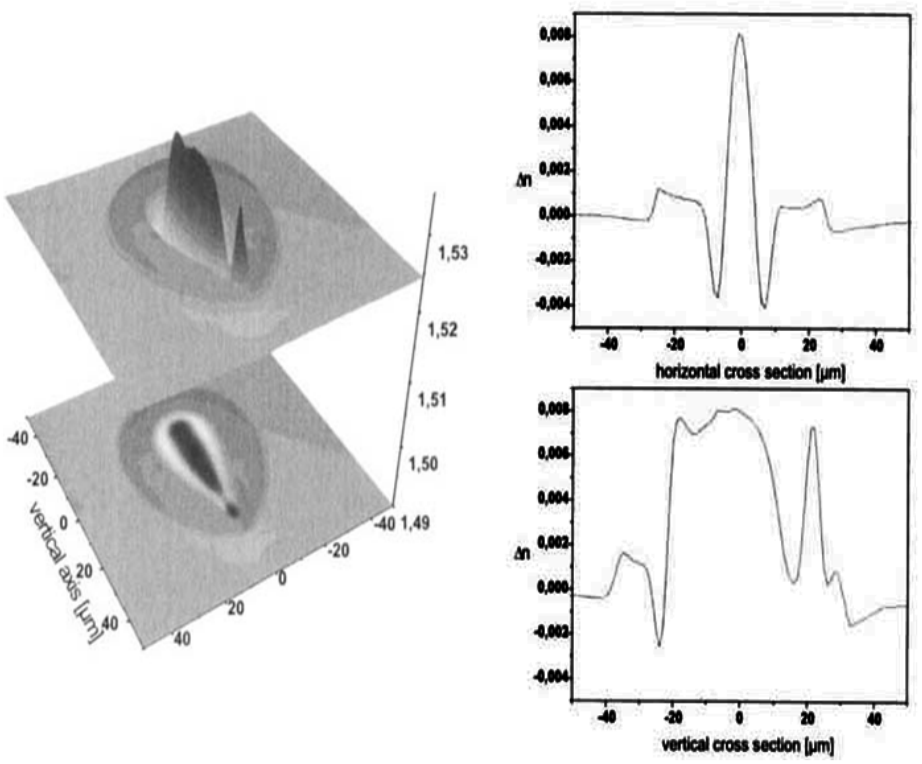

Figure 2.7: (a) & (b) Refractive index profile of the waveguides written in AF45 glass in a cumulative heating regime and (c) 1550 nm mode profile of the waveguide [111].

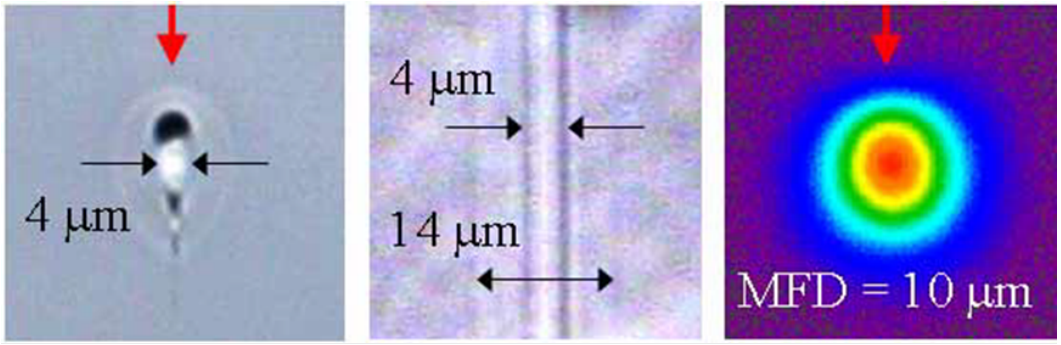

Figure 2.8: (a) Cross-section and (b) top view microscopic pictures of the waveguides written in AF45 glass in the cumulative heating regime and (c) 1550 nm mode profile of the waveguide [109]. Dark regions in the microscopic pictures represent the negative refractive index contrast, while the bright regions represent the positive index contrast. The resulting mode field profile is Gaussian-like.

and refractive index contrast, and high speed of the fabrication process make the high-repetition rate regime a very versatile technique well-suited to the fabrication of complex 3D optical circuits.

2.2.4 Substrate material

The choice of the substrate material is dictated by the device application and required properties of the glass, such as transmission, nonlinearity, and ability to be doped for active waveguide applications. This glass used in this work is an alkaline Earth Boro-Aluminosilicate Eagle2000 (Corning) glass. The glass is mostly used as a substrate for active matrix flat panel displays due to its good optical properties, mechanical endurance, low weight, chemical durability and low thermal expansion coefficient [113]. The high popularity of the glass results in its low cost.

Eaton et al. [66] showed the suitability of Eagle2000 glass for waveguide writing and since then the glass has become one of the most commonly used substrates for femtosecond direct-written waveguides and passive optical devices. By performing a large parameter scan they achieved very low propagation losses of $\sim 0.3\,\mathrm{dB/cm}$ at 1550 nm. Eagle2000 has been successfully used to fabricate high performance waveguides at 800 nm and 1550 nm for applications in telecommunication, quantum optics [114] and astronomy [10, 25].

Eagle2000 features relatively high transmission over the 500-2000 nm wavelength range. Figure 2.9a shows the optical absorbance of Eagle2000 [113] over the visible and near-IR wavelength range. The optical absorbance is the fraction of radiation absorbed at a specific wavelength and is expressed as:

$$I(z) = I_0 e^{-\alpha z}, \tag{2.3}$$

where I_0 is the initial light intensity, α is the absorption coefficient and z is the propagation direction (sample length). In 2013 Meany et al. [115] measured the absorption coefficient in Eagle2000 and AF45 (Schott) glass (Fig. 2.9b). Even though AF45 exhibits lower absorption losses, we selected Eagle2000 as the material of choice due to

our extensive experience with the glass and because AF45 was uncharacterised at the start of our project.

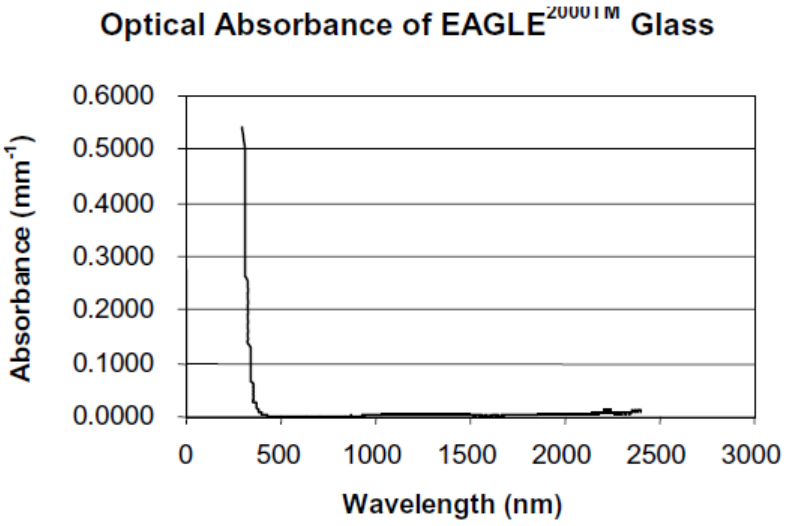

(a)

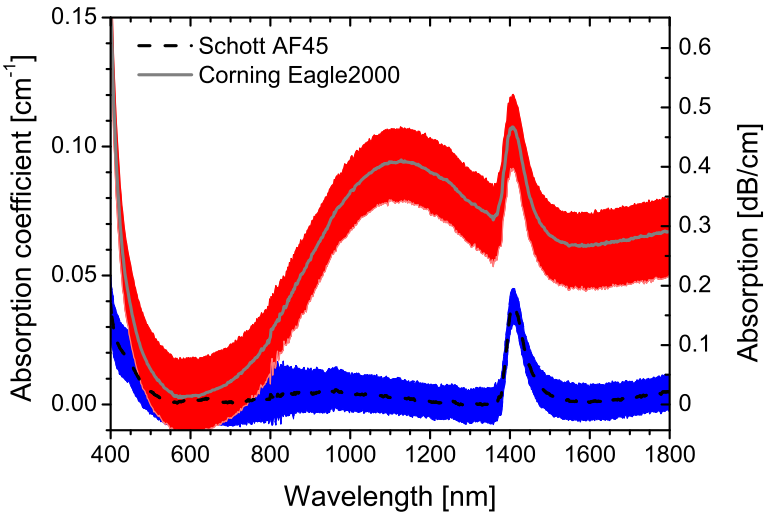

(b)

Figure 2.9: (a) Absorbance of the Eagle2000 glass [113]. (b) Bulk absorption spectra of Schott AF45 and Corning Eagle2000, including error bands due to experimental uncertainty [115].

3

Design and modelling of photonic lanterns

The requirement of low loss for the photonic lantern devices implies that the devices have to be carefully designed. With help of simulation tools it is possible to find the right geometrical parameters and predict the devices' performance prior to their fabrication. The photonic lantern structure can be broken down to three major components as shown in Fig. 3.1. The first one is the multimode waveguide for collecting the light from a telescope, or from a multimode guide used for transport. It should be able to collect all the light from a telescope, so its diameter, the acceptance angle (NA) and the number of modes supported have to match the telescope parameters. The second component is the transition between the multimode waveguide and the isolated single-mode waveguides, which has to be adiabatic thus slowly varying to allow for an efficient mode conversion. The final component consists of the isolated single-mode waveguides, which can be arranged in an arbitrary pattern but with the requirement

of supporting the same number of modes as the multimode section.

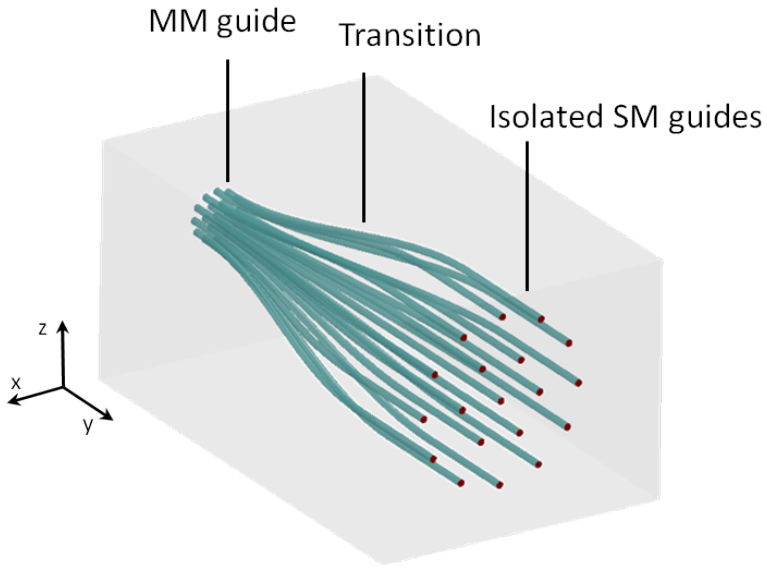

Figure 3.1: CAD model of the 1×19 photonic lantern and its blocks: multimode (MM), transition and isolated single-mode (SM) guides.

This chapter summarises the results of the preliminary study on the multimode waveguides by Jovanovic et al. [1], which created a foundation for the study presented here. Then it presents the coupled modes approximation and describes beam propagation software used to simulate the photonic lantern components and finally discusses the design and the results of the optimisation.

3.1 Multimode waveguides

The first element of the photonic lantern is the multimode waveguide section. The multimode waveguide determines the quality of the coupling into the device, therefore in our preliminary study [1], we analysed a number of multimode waveguides to find the most efficient design. We demonstrated that efficient multimode waveguides could be constructed from a lattice of single-mode waveguides in close proximity to each other arranged in a circular or hexagonal pattern (Fig. 3.2). The physical size of the single-mode waveguide is slightly smaller than the separation between them so that they do

not overlap but are sufficiently close to allow for significant cross-coupling. The size of a single-mode waveguide is ∼10 µm and the outer diameter of the multimode waveguides was designed to be 50 µm in diameter as a first step towards making large ≥ 100 µm multimode waveguides matching the diameter of the multimode fibres currently used at astronomical observatories. Taking into account these two geometrical constraints, the multimode waveguide is composed of 19 single-mode waveguides. The experimental results showed that the lowest loss devices consisted of 19 single-mode waveguides arranged in a circular lattice with a 10 µm separation between single-mode waveguides and fabricated with 35 nJ pulse energy at translation speed of 750 mm/min. This design was used for the photonic lantern design and simulations.

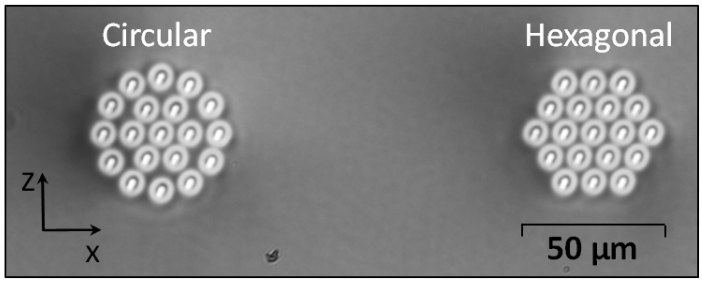

Figure 3.2: Cross-sectional micrograph of circular and hexagonal multimode waveguides. The waveguides are composites of 19 single-mode waveguides separated by 10 µm, fabricated in Eagle2000 glass with a femtosecond laser of central wavelength 800 nm, 5.1 MHz repetition rate, <50 fs pulse duration, 100× and NA = 1.25 objective lens, 35 nJ pulse energy, and translation speed of 1750 mm/min [1]. The angle in each individual refractive index modification originates from the off-centre position of laser beam in the objective aperture during the fabrication process.

3.2 Beam propagation and mode solving software

A commercial implementation of the beam propagation algorithm (BeamPROP package of RSoft [116]) and mode solver based on the finite element method (FemSIM package of RSoft [116]) were used to simulate the waveguide circuits. These packages allow for a detailed analysis of light propagation in complex structures using finite-difference beam propagation techniques. The program features a CAD environment

which allows the easy creation of 2D and 3D structures. The structure's physical properties include the background refractive index, refractive index difference (difference between the waveguide and material refractive indices), profile of the refractive index, free space wavelength and the width and height of the waveguides. The details of the parameters and settings used to simulate the photonic lanterns are given in the following sections.

3.3 Coupled mode approximation

Mode propagation in the photonic structures of complicated refractive indices are best solved using the finite element methods with packages like FemSIM (RSoft[116]). Nevertheless they can be approximated analytically using coupled mode theory, which will help in developing an intuitive understanding of the modal structure. In this section we introduce the basic concepts and show the solutions.

Let us approximate the electric field, E, as a scalar obeying the wave equation:

$$\frac{\partial^2 E}{\partial t^2} = \frac{c^2}{n^2}\nabla^2 E, \tag{3.1}$$

where E is the scalar electric field, t is time, c is the speed of light in a medium, n is the refractive index of the medium. The solutions of Eq. 3.1 are the optical modes of a waveguide. If we search for solutions like $E = E(x, y)\exp(i\beta z - i\omega t))$, where β is the propagation constant and the eigenvalue of the mode, ω is the angular frequency of a wave, Eq. 3.1 yields to its eigenvalue equation:

$$\beta^2 E = \left(\nabla^2_{x,y} + \frac{\omega^2 n^2}{c^2}\right) E, \tag{3.2}$$

which can be reduced to:

$$n^2_{\text{eff}} E = \left(\frac{\lambda_0^2}{4\pi^2}\nabla^2_{x,y} + n^2(x, y)\right) E, \tag{3.3}$$

where $n_{\text{eff}} = \beta/k_0$ is the effective refractive index, $k_0 = 2\pi/\lambda_0$ is the wavenumber in

vacuum and $n(x, y)$ is the refractive index profile at (x, y). If the waveguide of n_{core} refractive index is surrounded by a medium of n_{cladding} then

$$n^2(x, y) = n_{\text{core}}^2 \left(1 - \left(1 - \frac{n_{\text{cladding}}^2}{n_{\text{core}}^2}\right) g(x, y)\right), \tag{3.4}$$

where $g = 0$ at the maximum index and $g = 1$ for cladding [31].

The operator of the eigenvalue equation Eq. 3.3 is

$$A = \frac{\lambda^2}{4\pi^2} \nabla_{x,y}^2 + n^2(x, y), \tag{3.5}$$

hence we can write:

$$Af = n_{\text{eff}}^2 f \tag{3.6}$$

If we consider that the waveguide j is affected by other waveguides, the operator A can be expressed as

$$A_j = A_j^0 + \sum_{\substack{k=1 \\ k \neq j}}^{N} A_{jk} = A_j^0 + A_j^1, \tag{3.7}$$

where A_j^0 is the operator for a single waveguide and A_j^1 is the sum of the perturbations to $n(x, y)$ from all of the other N waveguides.

The solution for modes propagating in an array of N waveguides can approximated to first order as a linear combination of the wave equation solutions to the unperturbed system:

$$f = a_1 f_1 + \ldots + a_N f_N \tag{3.8}$$

In order to estimate the values of a_j, and the n_{eff} values for each mode, we substitute this into Equation 3.6, multiply by f_j for $1 < j < N$ and integrate, giving N sets of equations. These sets of equations can be approximated as a matrix equation:

$$\sum_{k=1}^{N} B_{jk} a_j = \left(n_{\text{eff}}/n_{\text{eff},0}\right)^2 a_j, \tag{3.9}$$

where $n_{\text{eff},0}$ is the effective refractive index of the LP_{01} mode of an isolated waveguide,

$B_{jj} = 1$, and B_{jk} is the overlap integral:

$$B_{jk} = \frac{1}{n_{\text{eff},0}^2} \int f_j(x,y) A_k^1 f_k(x,y) dxdy \tag{3.10}$$

for $j \neq k$. The overlap integral depends on the refractive index contrast and the separation between the waveguides; in fact $\log(B_{jk})$ is roughly a linear function of d_{jk} for large d_{jk}, where d_{jk} is separation between j and k waveguides. Finding the eigenvalues of the matrix $\mathbf{B_{jk}}$ will give rough eigenvalues of the coupled waveguides, meaning the $n_{\text{eff,j}}$ of the mode j relative to the effective refractive index $n_{\text{eff},0}$ of the LP_{01} mode of an isolated waveguide. The resulting eigenvectors will give the amplitude of the mode j at (x, y) position.

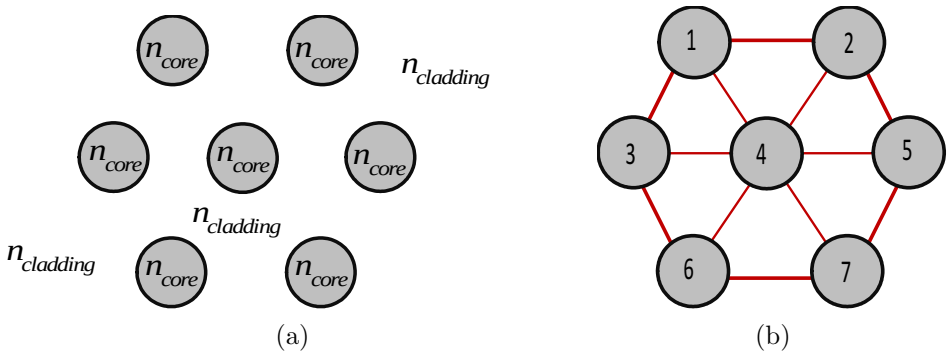

Figure 3.3: The geometry of the example presented here. (a) The cores of n_{core} are surrounded by a medium of n_{cladding} and are placed close enough to each other that their modes overlap. (b) Ordering of the waveguides.

Let us now consider an array of 7 waveguides as shown in Fig. 3.3. We can assume that each waveguide is affected only by the nearest waveguides, e.g. #3 affected by #1, #4, #6. Because of the equal distances to these waveguides, the overlap integrals have equal magnitude. Therefore for simplicity we will denote $B_{jk} = \alpha$ (α is the overlap coefficient) between neighbouring waveguides, $B_{jk} = 0$ for non-neighbouring

and $B_{jj} = 0$. In such a case, the matrix $\mathbf{B_{jk}}$ can be expressed as:

$$\mathbf{B_{jk}} = \begin{pmatrix} 1 & \alpha & \alpha & \alpha & 0 & 0 & 0 \\ \alpha & 1 & \alpha & \alpha & 0 & 0 & 0 \\ \alpha & 0 & 1 & \alpha & 0 & \alpha & 0 \\ \alpha & \alpha & \alpha & 1 & \alpha & \alpha & \alpha \\ 0 & \alpha & 0 & \alpha & 1 & 0 & \alpha \\ 0 & 0 & \alpha & \alpha & 0 & 1 & \alpha \\ 0 & 0 & 0 & \alpha & \alpha & \alpha & 1 \end{pmatrix} \tag{3.11}$$

Figure 3.4a shows details of the modes solved using the above method, assuming the overlap coefficient $\alpha = 0.0004$ and the effective refractive index of the LP_{01} for an individual single-mode waveguide $n_{\text{eff}} = 1.4883$. The structure supports 7 modes per polarisation direction. The modes in a 7 waveguide array were also solved using the FemSIM package of RSoft [116]. Each waveguide had a $\sim 10\,\mu$m diameter and the refractive index profile of a typical HPO system laser-written waveguide (FEMTOSOURCE XL500 modelocked Ti:sapphire femtosecond high-power oscillator (HPO), cf. Section 3.4). The simulation was performed to solve for 9 modes, so that it is clearly visible which modes are supported in the structure. Figure 3.4b shows the result of the simulation. There are 7 modes per polarisation direction guided in the waveguide structure, while two modes have an effective refractive index lower than the glass refractive index, meaning they propagate in the cladding. In summary, the two methods show almost identical solutions, which means that the approach presented here is a good approximation.

The only physical parameter that changes along the photonic lantern is the separation between the waveguides, which means the overlap integral between the modes varies. By solving the modes for a range of the overlap coefficient α we can monitor the modes' evolution along the transition between the multimode waveguide and the isolated single mode waveguides. As was described in Section 1.3.1 the first essential requirement for the low-loss photonic lantern is to preserve the number of modes in each section. In order to investigate the evolution of the modes along the transition, the

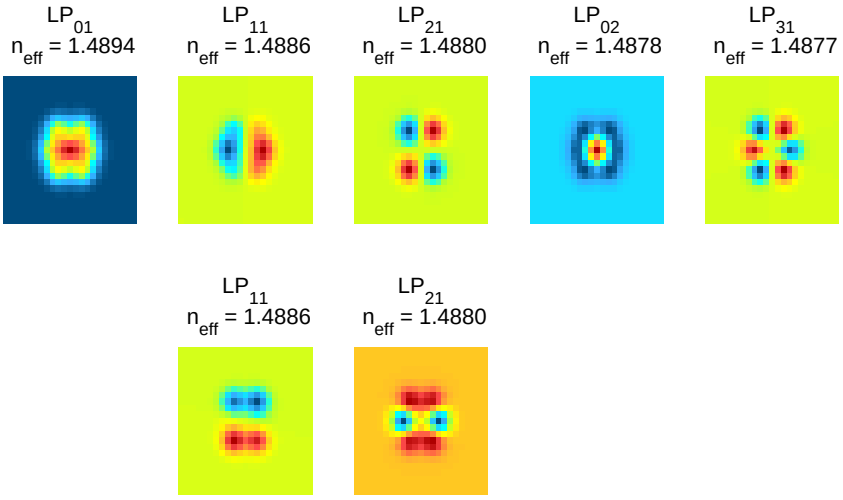

(a)

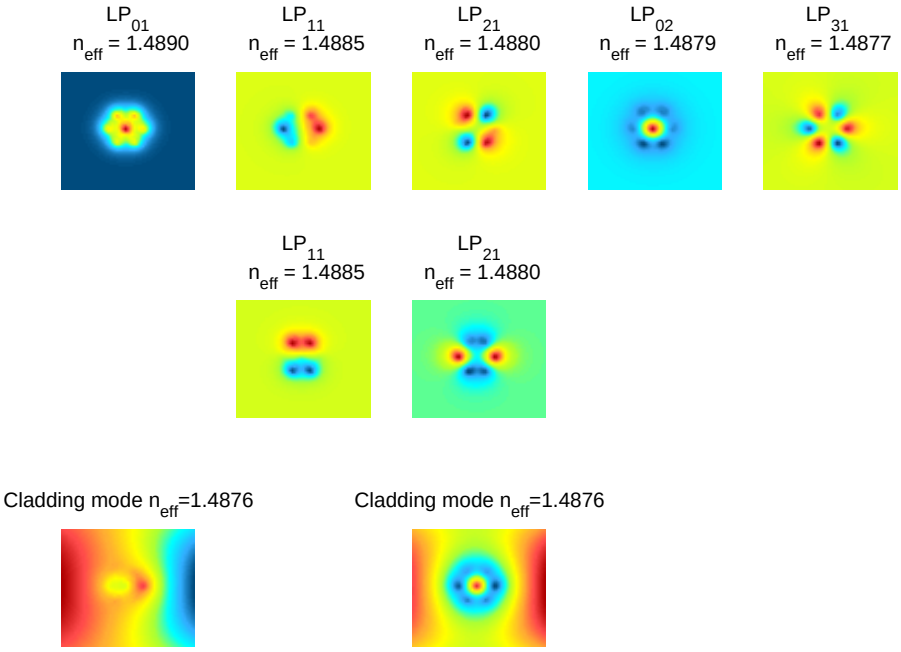

(b)

Figure 3.4: Details of the modes supported by an array of 7 waveguides (a) solved using the coupled modes approximation for an overlap integral (b) computed at 1550 nm wavelength with the FemSIM package and using the refractive index profile for typical system laser-inscribed single-mode waveguides separated by 12 µm.

eigenvalues of the matrix $\mathbf{B_{jk}}$ were solved for a range of the overlap coefficients α between 0 and 0.0005, where 0 means that there is no influence from the other waveguides and 0.0005 means that there is relatively strong coupling between the modes.

Figure 3.5a shows the n_{eff} for the modes supported by the 7 waveguide array, where n_{eff} of the LP_{01} for an individual single-mode waveguide is 1.4883. The x-axis was reversed in order to better present the data. For high overlap coefficients α the modes are highly distinctive and fill the range of n_{eff}. When counting only one polarisation 7 non-degenerate modes are supported in a structure. For low overlap coefficients α, the modes are converging to the n_{eff} of an individual single-mode. This means the waveguides are sufficiently far apart, so that 7 degenerate modes can propagate. The simulation of the 7 waveguide array was repeated using FemSIM for a range of separation distance between the waveguides. Figure 3.5b shows n_{eff} as a function of the waveguide separation between 6 µm and 40 µm. When the distance between the waveguides is smaller than the waveguide diameter, the n_{eff} of the higher order modes (LP_{02} and LP_{31}) is below the glass refractive index n_{cladding}. Therefore (LP_{02} and LP_{31} are propagating in the cladding and there are < 7 guided non-degenerate modes in the structure. When the separation between the waveguides is approximately equal to the size of the waveguides, all 7 non-degenerate modes are propagating in the structure. As expected, for large waveguide separation (> 35 µm) the modes are becoming degenerate with no cross-coupling between them.

In conclusion, FemSIM gives an accurate solution for the photonic lanterns allowing the use of the actual refractive index profile for the waveguides, while in the coupled mode the step index profile was used. Nevertheless, the method still provides a good approximation of the modes' evolution.

3.4 BeamPROP – Photonic lanterns

This section gives details of the settings chosen to simulate the photonic lanterns in BeamPROP [116]. Figure 3.6 shows a screenshot of a 1×19 photonic lantern created in BeamPROP. With the intention of reproducing the physical devices as accurately

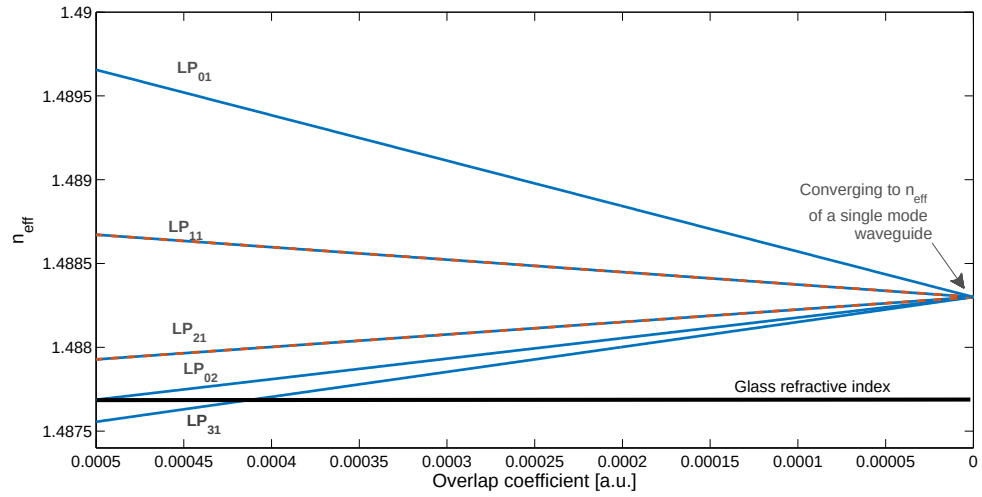

(a)

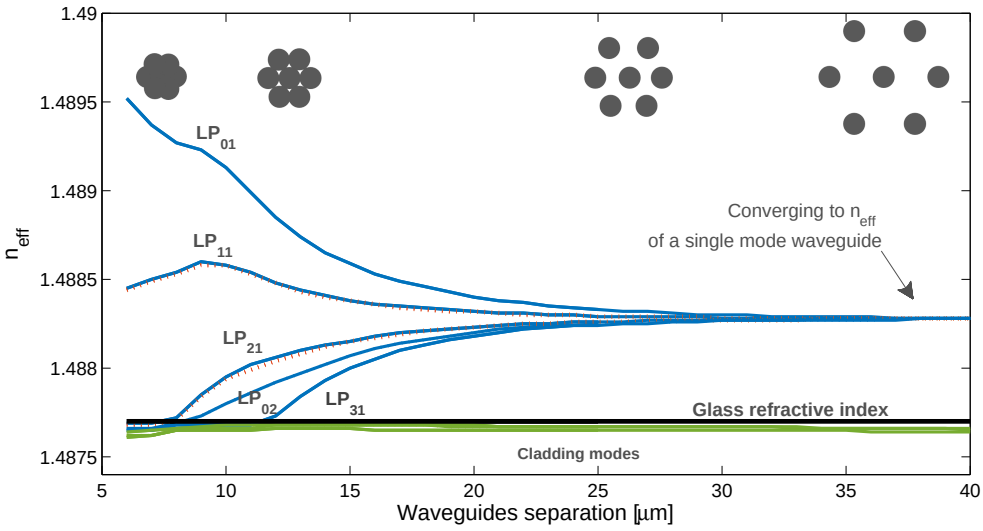

(b)

Figure 3.5: Evolution of the effective refractive index (n_{eff}) of the modes along the transition section of the 7 waveguide photonic lantern. (a) n_{eff} as a function of the overlap integral calculated using the coupled modes approximation. Overlap integral is plotted in reverse order because is it proportional to the inverse of the waveguides separation. (b) n_{eff} as a function of the waveguide separation computed using the FemSIM package and visualised waveguide separation change.

as possible, real physical parameters were used in the simulation. As described in Section 2.2.2 the HPO system produces a non-uniform refractive index modification, meaning that the pre-set BeamPROP index profiles cannot be used. Instead, a user defined index profile was applied. A refractive index profile of a typical HPO system laser-inscribed SM waveguide was taken with a refractive index profilometer (Rinck Elektronik) as seen in Fig. 3.7. The data were inserted into the program for each single-mode waveguide and the index profile was rescaled to compensate for material dispersion between 0.633 µm (where the index profile was measured) and 1550 nm (where the waveguides operate) by using the Sellmeier equation for Corning Eagle2000 (the glass of choice for experiments). The width (and height) of the waveguides was based on the measured values and, if needed, adjusted to match the simulated mode field diameter and the measured physical mode field diameter of the waveguide.

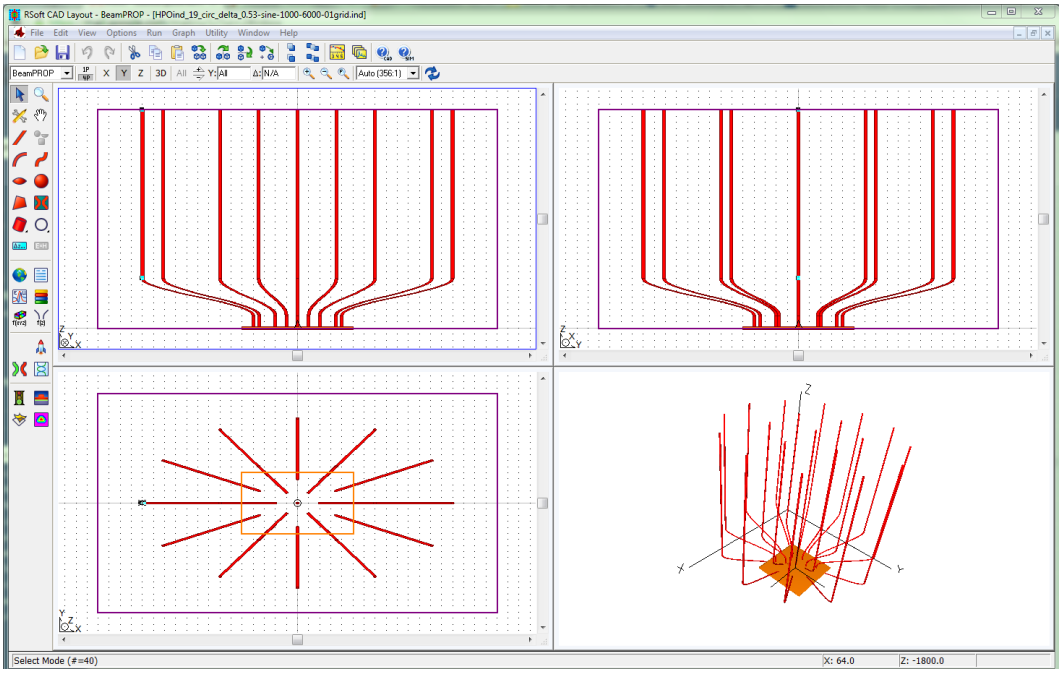

Figure 3.6: Screenshot of a photonic lantern structure in BeamPROP.

The parameters to run a simulation have to be chosen carefully, as they can greatly affect the result. Table 3.1 summarises parameters used in the simulation. The initial condition of the simulation is the launch field. BeamPROP allows selection among the following launch types: fibre mode, Gaussian, rectangle, computed mode, user defined

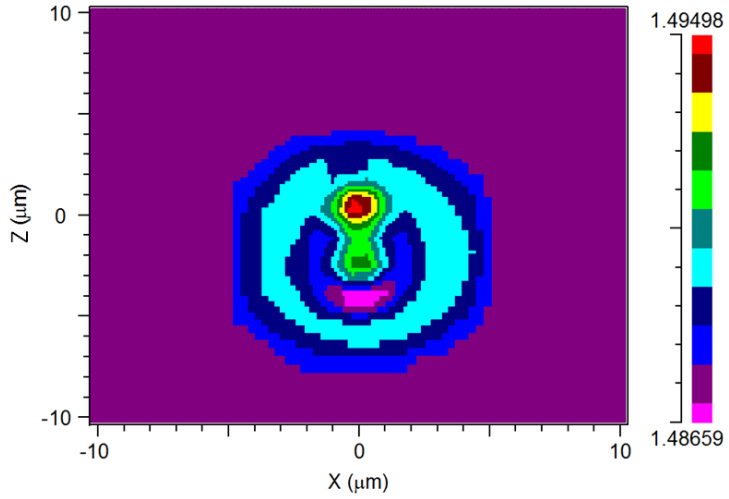

Figure 3.7: Refractive index profile of a single waveguide fabricated with the laser system.

and multimode. The multimode type is a superposition of all fibre modes supported by the input multimode component and it was selected because it best approximates the physical conditions and ensures that all the modes in the multimode waveguide are equally excited.

BeamPROP solves the Helmholtz equations for a given structure within a computation domain an a spatial grid. Both the domain and spatial grid have to be defined correctly to ensure a correct result. The domain size has to big enough to include all the structure elements, which was satisfied by defining it between -90μm and +90 µm. The spatial grid size has to be small enough to present accurate results. It is a trade-off between the computing time and accuracy. Given that the study required a large number of simulations, the computing time was an important factor and first a convergence study was performed, starting with a grid size of 2 µm and going down to 0.01 µm. The results were convergent at 0.1 µm and below, therefore the grid size was defined as 0.1 µm.

The objective of the simulation was to find the least lossy design of the photonic lanterns. Due to the relatively complex geometry of the photonic lanterns the best way to measure the transmission is to monitor the total power (normalised to the input power) contained in the simulation domain along the Y coordinate. As the total

Table 3.1: Summary of the simulation parameters for the photonic lantern beam propagation.

Parameter	Type	Comments
Wavelength	1550 nm	Wavelength of interest.
Background index	1.4877	Refractive index of the glass of choice: Corning Eagle2000.
Launch field	Multimode	The multimode input field is a superposition of all fibre modes supported by the input component with equal power in each mode and a random phase for each mode.
Domain Min/ Domain Max	-90 µm / +90 µm	The size of the domain has to be big enough to include all parts of the structure and electromagnetic fields to be simulated, including any evanescent fields outside of the structure.
Grid size	0.1 µm	A fine grid size is important to ensure high accuracy of the simulation. A convergence study was performed to find an optimum grid size.
Pathway Monitor	Total power	The value returned by the simulation is the total power in the simulation domain as a function of Y.
Isolated single-mode waveguides length	27 mm	The long length of the isolated waveguides is important to make sure that all the light, which escaped in the transition part, is outside the simulation domain, as the total power pathway monitor was selected.

power monitor includes both the guided and non-guided light, it has to be ensured that the non-guided light is outside the simulation domain and not included in the final result. Most of the light escapes along the transition section and if the isolated SM waveguides are long enough, one can be sure that non-guided light is outside the simulation domain. For that reason the isolated SM waveguides were extended to a length of 27 mm (Fig. 3.6). Figure 3.8 shows a result of the simulation and the total power variation along the Y coordinate. It can be seen that the light begins to escape at $\sim$10,000 µm (10 mm) and the total power stabilised at the level of 90% at $\sim$15,000 µm (15 mm).

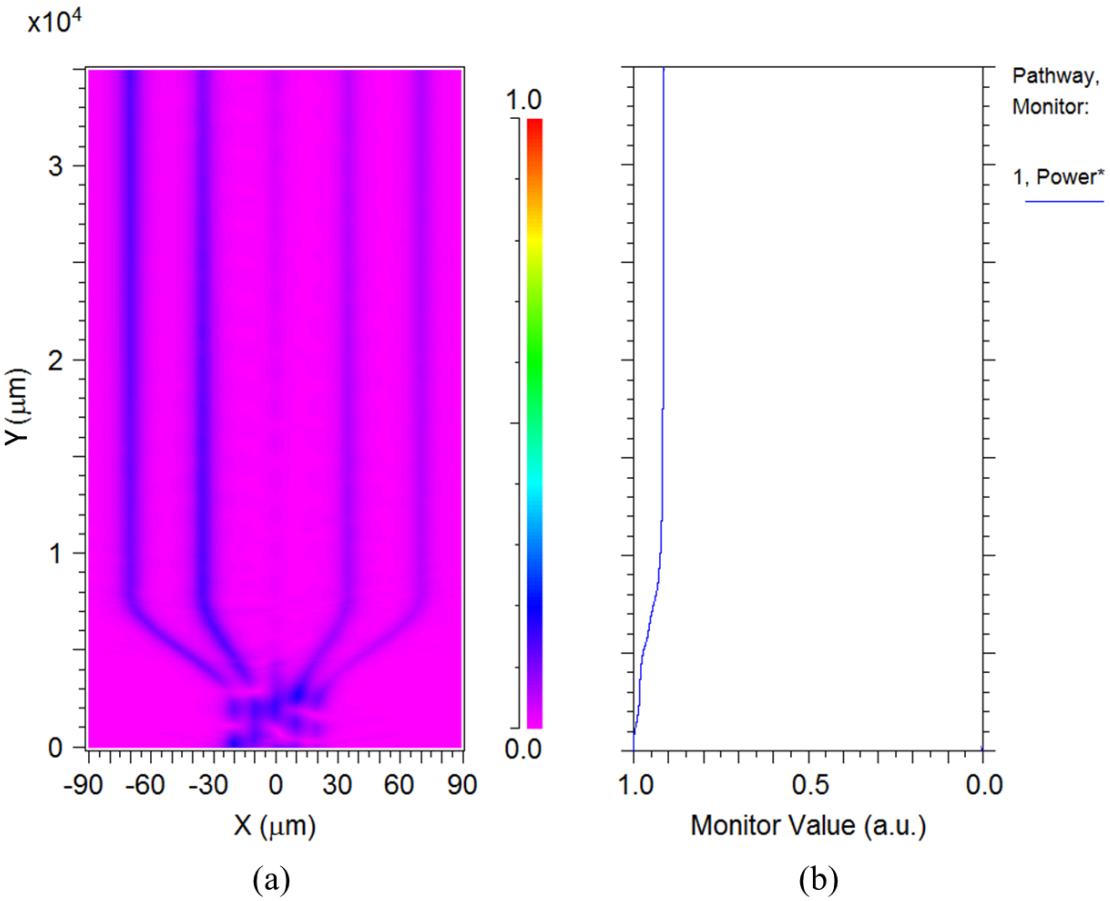

Figure 3.8: BeamPROP simulation window, where (a) shows the light propagation along the Y coordinate and (b) shows the total power changes along the device.

3.5 Adiabatic transition between the multimode waveguide and isolated single-mode waveguides

The second requirement for lossless photonic lanterns is an adiabatic transition between the multimode and isolated single-mode waveguides sections (see Section 1.3.1). The following sections will describe the designs which were considered and the modelling results.

3.5.1 Design

There are two factors determining the adiabatic transition. The first one is the geometrical shape of the transition and the second one is its length. Based on the common designs three types of transitions were considered: linear, cosine bend and raised sine bend [116]. Their equations are presented in Table 3.2 and visualised for comparison in Fig. 3.9. Arriola et al.[117] showed that low bend loss single-mode waveguides fabricated on the HPO system (see Section 4.2.1) can be achieved when the radius of curvature is $\geq$ 40 mm. Based on analytical calculations this value corresponds to a transition length of $\geq$ 4 mm for our design of 1×19 photonic lanterns and gave us a reference for this study. The simulations were performed as the transition length changed from 1 mm to 24 mm.

Table 3.2: Summary of the functions used for transition part in the photonic lanterns; y is the horizontal position and $x(y)$ is the vertical position.

Type of function	**Formula**
Linear	$x(y) = y$
Cosine	$x(y) = \frac{1 - \cos(\pi \cdot y)}{2}$
Raised sine	$x(y) = y - \frac{\sin(2\pi \cdot y)}{2\pi}$

3.5.2 Simulation results

Figure 3.10 presents the results of the transition type and length simulation at a wavelength of 1550 nm. The figure shows the normalised throughput as a function of transition length for all three transition types (linear, cosine and raised sine). For taper lengths between 1-5 mm, the losses strongly depend on the transition length. For transition lengths $>$ 5 mm the transmission reaches $\sim$ 0.97 and flattens off. The 5 mm length roughly agrees with the analytical finding, which showed that the transition length should be $\geq$ 4 mm. This high throughput is due to the fact that the multimode section supports 12 modes whereas there are 19 single-modes (see section 3.7).

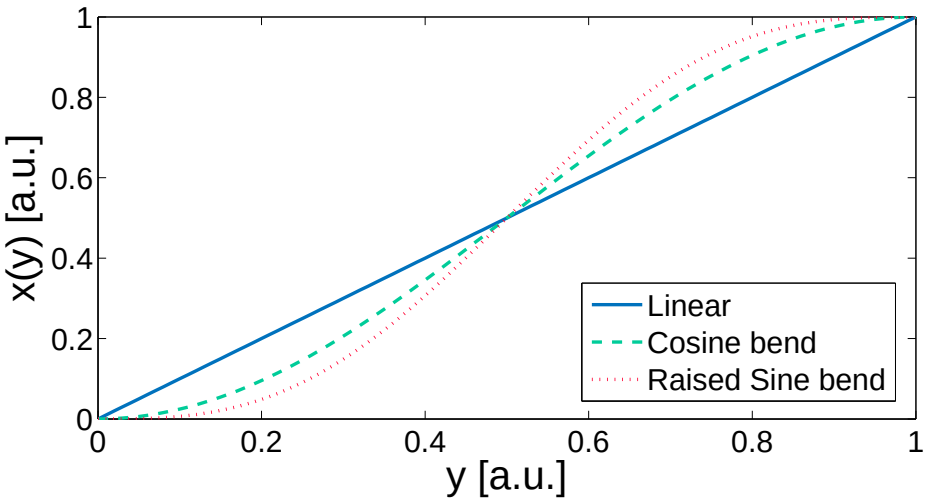

Figure 3.9: Linear, cosine and raised sine types of function.

The cosine type of transition offered the best performance for short transition lengths, therefore it was chosen for all fabricated devices presented further in this work.

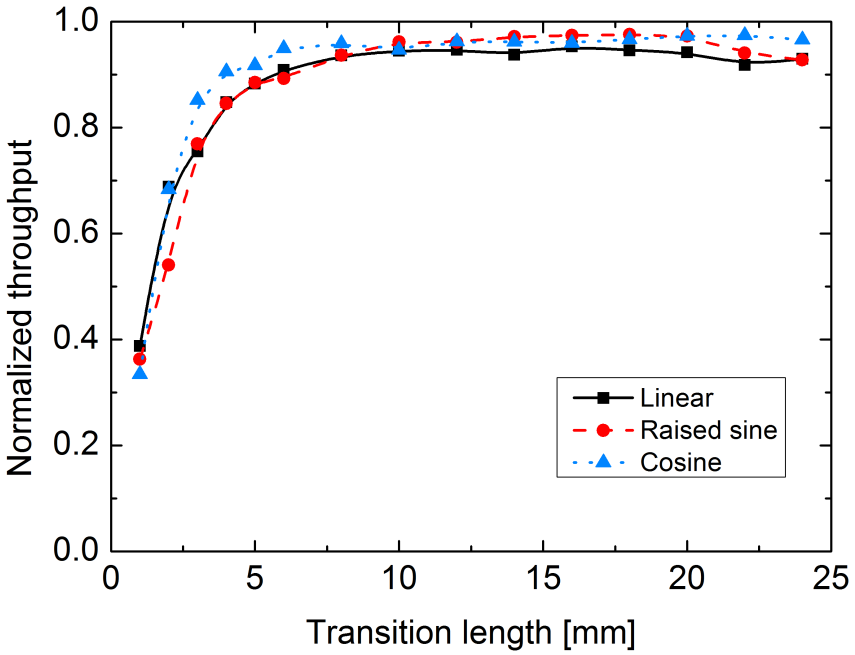

Figure 3.10: Simulated normalised throughput as a function of transition length between MM and SM sections for three different transition types: linear, raised sine and cosine.

3.6 Isolated waveguides

The final block of the basic design of the photonic lanterns are the isolated single-mode waveguides. In particular, the single-mode waveguides must be far enough apart so that there is no cross-coupling between them, so that devices like waveguide Bragg gratings can be used efficiently. The required separation for waveguides presented here is $\geq$ 37 µm (as shown in Fig.3.5b). In a photonic lantern device this was achieved by increasing the separation between the waveguides from 10 µm up to 37.5 µm and creating a circular array of separated, non-coupled single-mode beams (Fig. 3.1). If the photonic lantern has to be interfaced with another device the output can be arranged in an arbitrary format. One of the examples is a linear array of SM waveguides i.e. a slit, which finds an application in astronomy as outlined in Section 5.4.

3.7 Design of the slit reformatting devices

The separated isolated single-mode waveguides can be reformatted into a slit (fanout) with separations between single-mode waveguides large enough to avoid coupling. This however would require a long slit (e.g. 19 waveguides at the wavelength of 1550 nm, 40 µm spacing results in 720 µm slit length) which becomes difficult when one moves to the visible as the mode count scales with $1/\lambda^2$ (150 waveguides now required at the wavelength of 0.55 µm, 15 µm spacing means 2250 µm slit length). This puts constraints on the quality of the optics required to image off-axis cores at the diffraction limit in the spectrograph. A more serious concern though is the poor use of the valuable detector area.

As such, the ideal scenario is to bring the waveguides in the slit closer together so that they become coupled. However, when recombining the beams to form a slit, the converse of the above condition is also true; for a lossless slit the number of non-degenerate modes supported by the slit must be equal to the number of single-mode beams that are being combined. This condition can be fulfilled by careful selection of the waveguide spacing in the slit. The number of modes supported by a linear array

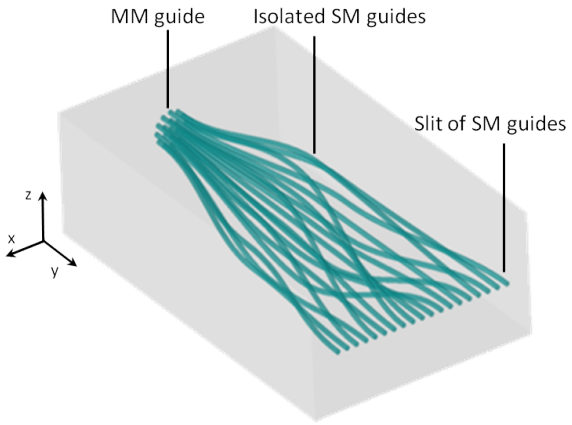

Figure 3.11: CAD drawing of a slit reformatting device.

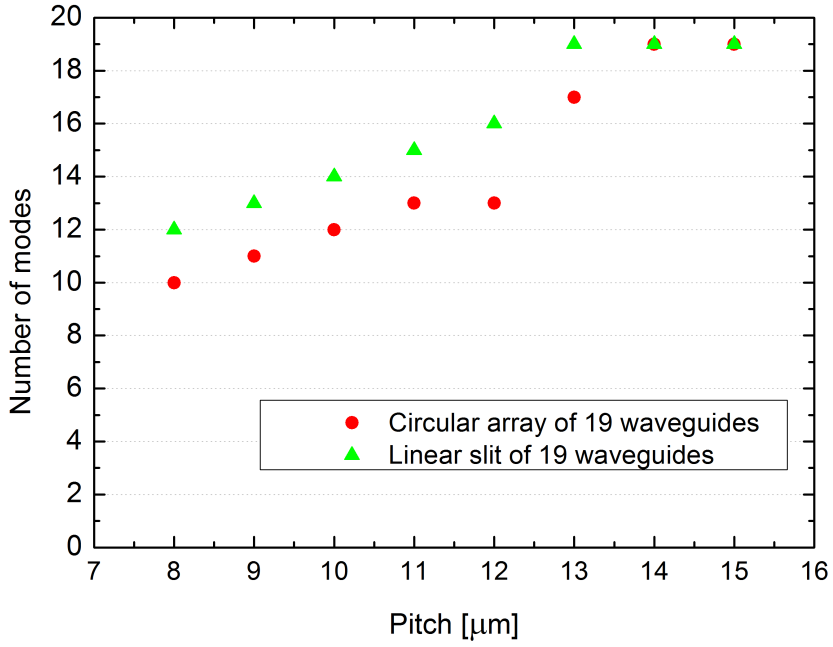

Figure 3.12: Number of modes supported by the circular lattice structure of 19 waveguides and a linear slit as a function of the separation between the waveguides (pitch).

of single-mode waveguides as a function of the spacing has been calculated in FemSIM (package of RSoft [116]) and is shown in Fig. 3.12. It can be seen that for the same waveguide spacing (pitch) the waveguides in a linear slit arrangement support more modes than waveguides in a circular arrangement. Moreover a minimum separation of 13 µm between the waveguides will still support the 19 modes required for a lossless slit to be realised. By using this technique it is possible to reduce the slit length to 250 µm and hence maximise the detector real estate used. In this way the slit is multimode in nature along its length but still retains the single-mode format in the orthogonal dispersion direction, which allows for a miniature spectrograph (free from scaling laws common to seeing-limited spectrographs) to be constructed.

In order to design a high-transmission slit reformatting device the adiabatic requirement for a transition between the isolated single-mode waveguides and slit-like pattern has to be fulfilled as well. This condition will be satisfied by allowing the transition to be long enough and by remapping the circular-like pattern into a slit-like pattern by remapping them in the right order (this will be explained in Section 3.7.1). The latter task is straightforward when dealing with several waveguides but becomes challenging for as few as 19 waveguides.

3.7.1 Design Lantern GUI

A Matlab program was developed to design slit reformatting devices (source code included in Appendix B). The software designs the geometry and exports the data to the G-code, which enables the devices' inscription (see section 4.2.3). The program's Graphical User Interface (GUI) allows the user to easily set and change various geometrical parameters (Fig. 3.13), such as separation between the waveguides and length of each section. By default the photonic lantern has a circular-like input, where each of the rings contains a multiple of six waveguides. The isolated waveguides section is a replica of the input with increased separation between the waveguides and the output of the device forms a slit (fanout).

Based on the `Geometry Parameters` and `Sample Length Parameters` the program creates a photonic lantern (`Create 3D lantern`). The key function has to remap the

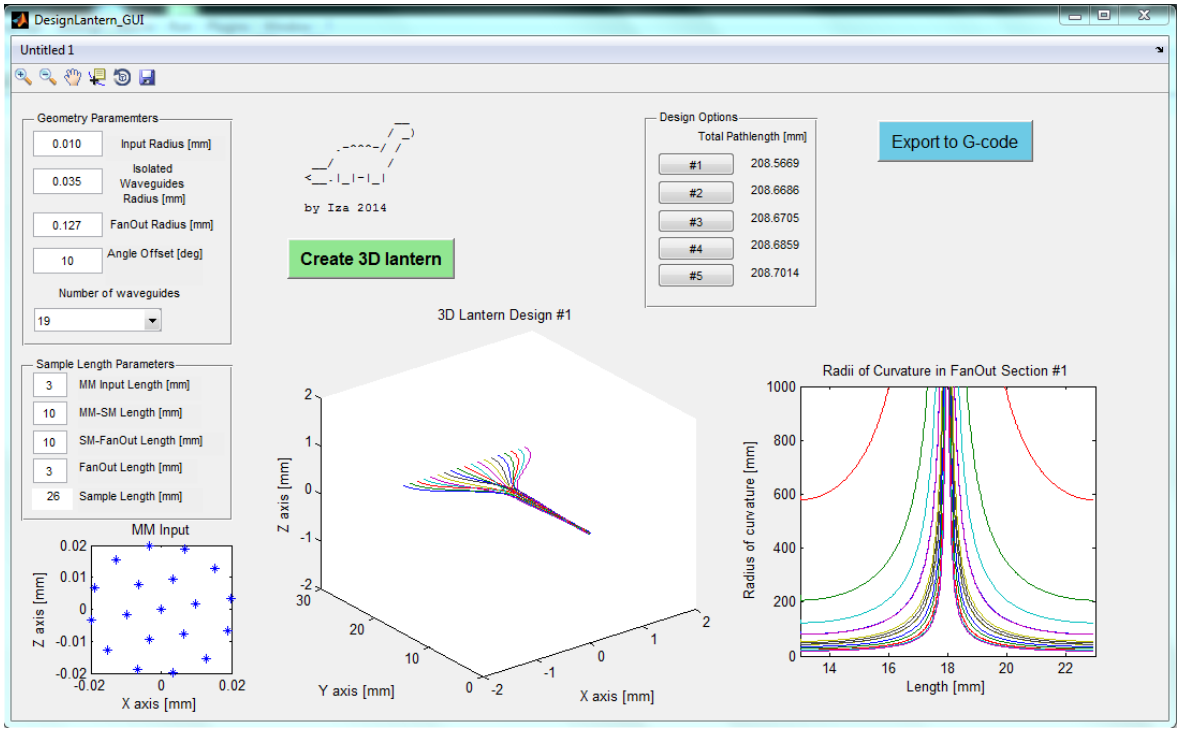

Figure 3.13: Screenshot of the DesignLantern GUI. The user can define geometrical parameters of each section of the slit reformatting device, inspect best solutions and export the coordinates to G-code.

circular isolated waveguides pattern into a slit-like linear pattern. For that, the function finds a number of random combinations of connections, calculates their cosine path lengths and shows the best solution. *The best* solution is defined as the one where the sum of the cosine path lengths is the smallest. This condition ensures that no waveguides are intersecting and the closest connections are selected. The program also calculates and displays the radii of curvature along the isolated waveguide-slit section. The user can select between five best designs (in terms of the path length), which have different radii of curvature and chose the one to be exported to the G-code coordinates.

4

Experimental methods

This chapter describes the methods, procedures and equipment used to fabricate and characterise the photonic lanterns fabricated with the femtosecond direct-write technique. As the devices are inscribed in a glass block, the sample has to first undergo mechanical preparation by cutting the glass to the desired size. The waveguides' are then fabricated on the high-power oscillator (HPO) system. As the final step of the fabrication process, the glass sample undergoes mechanical-chemical post-processing in a form of grinding and polishing to reveal the ends of the waveguides and achieve high optical quality end facets. The devices are then characterised visually by an optical microscope to verify the waveguides geometry. Finally their physical and optical properties are determined using specialised optical setups.

The chapter is divided in three sections describing mechanical-chemical pre- and post-processing, waveguide laser fabrication, and waveguide characterisation.

4.1 Sample preparation

The glass sample requires some preparation before and after laser fabrication. The glass used in the work presented here is Corning Eagle 2000 which usually comes in large plates of a thickness of 1.1 mm. The top and bottom surfaces are normally pre-polished by the supplier. The sample needs to be cut to the desired dimensions and then it is ready to be used for laser writing. Special care is taken while aligning the glass block for dicing to achieve square edges as well in the laser writing to produce waveguides parallel and perpendicular to the glass edges. Once the laser writing is done, the front and back faces of the sample need to be ground and polished.

4.1.1 Dicing

A SYJ-400 CNC dicing saw (MTI Corporation, Richmond, CA) was used to cut the glass. First the glass plate is mounted on a sacrificial glass disc using hot wax and then it is assembled on a translation stage. To ensure high rigidity of the assembly, the bottom surface of the glass is covered with a small amount of silicon high vacuum grease (Dow Corning®) and placed on the vacuum chuck of the XYZ translation stage. To ensure the square edges of the glass sample, the glass block is aligned by eye as best as possible to be parallel to the dicing blade. The stage is controlled by a computer driven motion system and the sample is cut using a 350 µm thick diamond disc blade. In order to achieve smooth cuts/edges and prevent potential cracks and stresses in the glass, the stages are moved at low speed and the disc blade is cooled with water.

4.1.2 Griding/lapping and polishing

After the waveguide structures are fabricated, the front and back face of the sample need to be ground and polished. The sample has to be ground back by about 300 µm because during the fabrication process the waveguides suffer from a tapering down effect when the laser beam gets close to the glass edge. Smooth faces of the sample, achieved by polishing, improve coupling in and out of fibre as well as free space coupling.

Logitech PM5 and Logitech PM4 Grinding/Lapping and Polishing Machines were

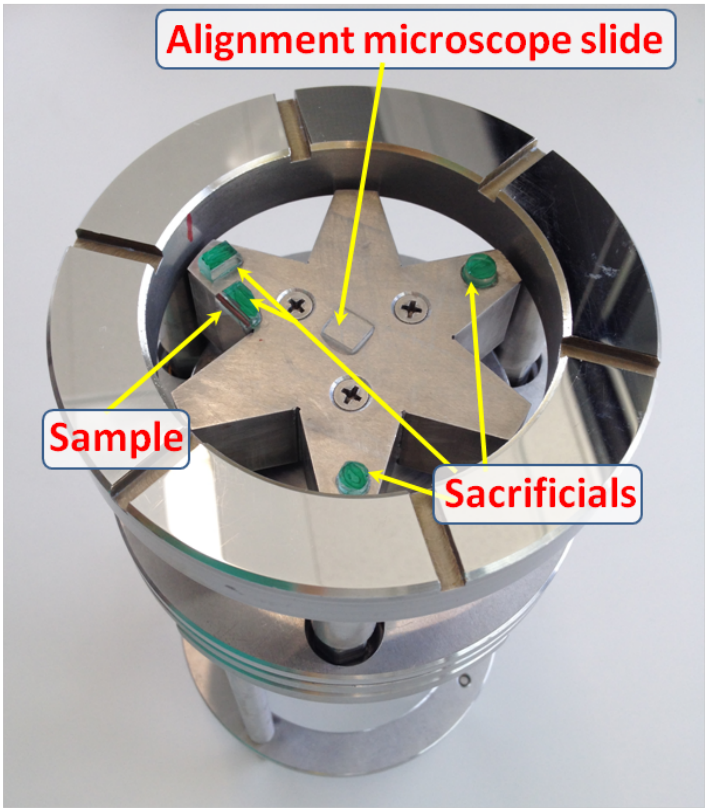

Figure 4.1: Lapping/polishing jig with mounted sample and sacrificials. A green-colour marker is used to paint the sacrifilas and the sample to give a reference of the griding progress.

used for the glass post-processing. The main features on both machines are identical, therefore the description applies to either of them. The process consists of the four steps: sample mounting, grinding, polishing, debonding. The sample is first mounted onto a PM4/PM5 jig (Fig. 4.1), in a way that the pressure is applied in direction perpendicular to the waveguides. As protection, 170 µm thick microscope cover slips are glued with Norland Optical Adhesive 61 to both surfaces of the sample and the entire assembly is glued to a star-shaped metallic sample holder. In order to reduce the amount of direct pressure on the sample and reduce the risk of chopping off the edge, sacrificial pieces of glass are glued to the top and bottom surfaces of the star sample holder. The grinding jig allows control of the pressure applied on the sample as well as squaring the sample, so that the front face of the sample is perpendicular to the waveguides. The pressure applied is a compromise between the speed of the grinding

process and the risk of damaging the edge of the sample. The squareness of the sample is measured by reflection of the laser light from a piece of microscope slide on the top surface of the sample holder, and adjusted by three angular adjustment screws in the grinding/polishing jig.

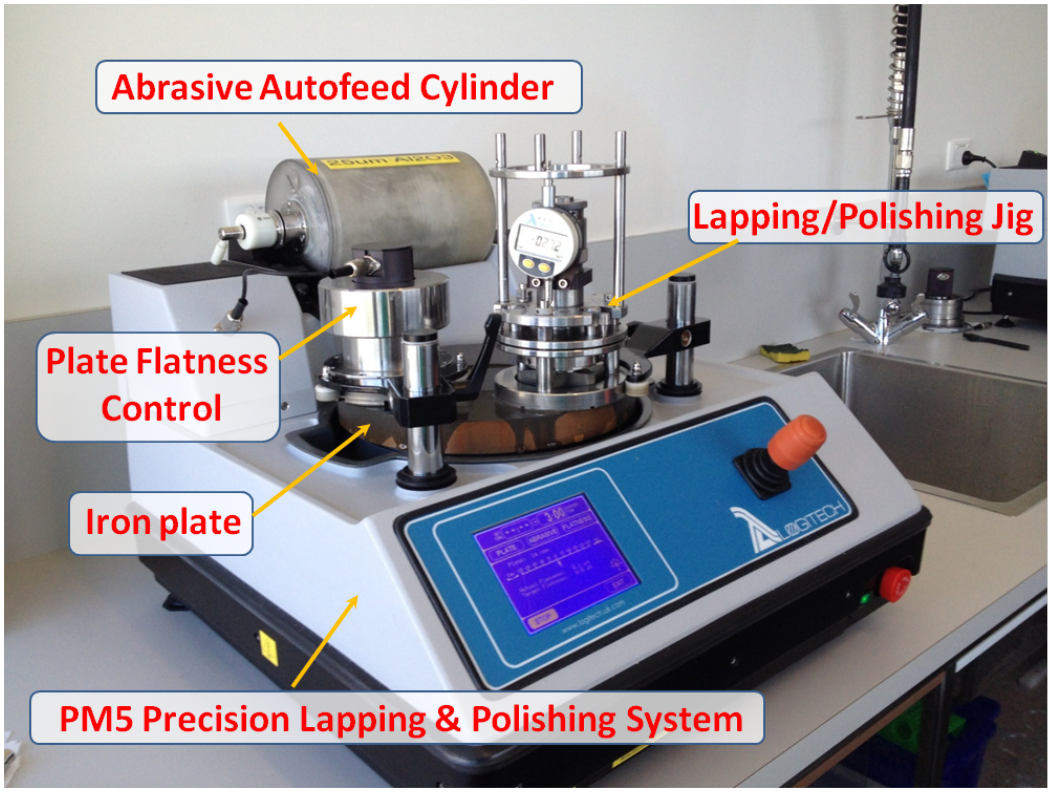

Figure 4.2: Photograph of the lapping setup. The sample is mounted on the lapping/polishing jig. The cylinder with the abrasive continuously feeds the abrasive onto the rotating iron plate. The plate flatness jig is connected to the system and measures the flatness of the iron plate.

The grinding process consists of two steps: coarse grinding with a 25 µm grit size Al_2O_3 (Micro Abrasives Corporation, MA) abrasive and fine grinding with a 5 µm grit size abrasive. The coarse grinding removes most of the excess material (about 300-400 µm) and reveals the ends of the waveguides. The 5 µm grit size abrasive is used to smooth the glass faces to $\sim$ 25 µm surface roughness. The abrasive is mixed with reverse osmosis filtered tap water in an autofeed cylinder to create the grinding solution. The cylinder is placed on top of the lapping machine and is rotating continually to ensure good mixing of the abrasive. The grinding jig with the sample is placed on the rotating

cast iron plate, which is continually lubricated with grinding solution (Fig. 4.2). The machine is equipped with an automatic plate flatness control system which continually monitors the plate shape and automatically corrects any deviations from the pre-set shape. An electronic micrometer monitors the amount of material removed. After the coarse grinding all the parts of the system are cleaned to avoid transferring the residuals between the steps. The 5 µm grit size abrasive is then used to remove ∼ 30 µm of the material and smooth the surface.

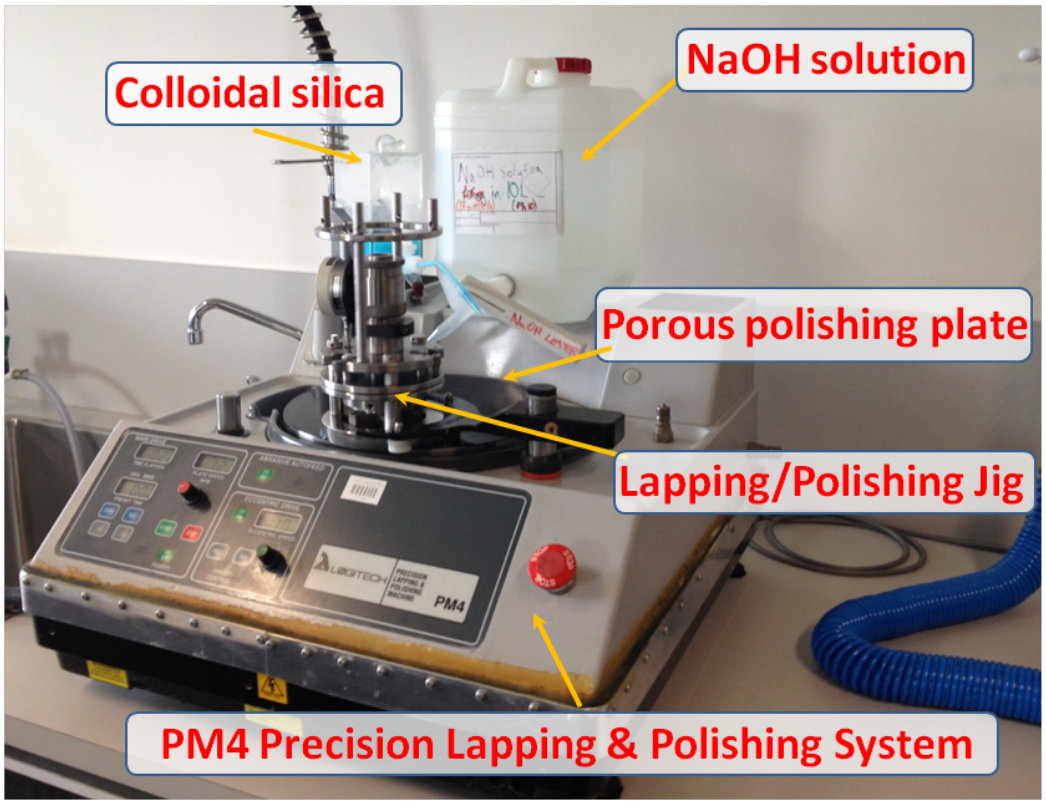

Figure 4.3: Photograph of the polishing setup. The sample is mounted on the lapping/polishing jig. The solution of colloidal silica and NaOH create the polishing suspension and lubricate the rotating polishing plate.

After the grinding process, the sample and jig are cleaned carefully again and the lapping/polishing machine is rearranged for the polishing mode (Fig. 4.3). The iron plate is replaced by an iron plate covered with a porous polishing cloth. A solution of an aqueous colloidal silica slurry (Ultra-Sol 500S, Eminess Technologies Inc., AZ) and pure water with NaOH pellets dissolved was used as a polishing suspension. Once the

desired surface roughness is achieved, the sample is debonded and cleaned by immersing the star adaptor with the sample in acetone and, if required, in an ultrasonic bath.

4.2 Waveguides fabrication setup

The devices were fabricated using the high repetition rate laser writing system which consists of three main parts: the laser, a set of optical elements and an air-bearing 3-axis stage. The entire system sits on top of an air-suspended optical table in a temperature stabilised air-conditioned room. The following subsections describe each of the main subsystems.

4.2.1 Laser

The laser is an ultrafast titanium sapphire (Ti:sapphire) high peak power oscillator (HPO) from Femtolasers GmbH, model FEMTOSOURCE XL 500. The laser produces short light pulses with central wavelength of 800 nm, <50 fs pulse duration at a 5.1 MHz repetition rate. The maximum pulse energy is 550 nJ, which corresponds to 11 MW of peak power and 2.75 W average power. The high repetition rate and relatively high pulse energy enable the laser to operate in the cumulative heating regime (as explained in Section 2.2.2). As a consequence the waveguides can be written at a speed of 500-2000 mm/min (≈ 8-33 mm/s), which is relatively high and thus particularly important for devices with a large number of waveguides such as photonic lanterns.

Figure 4.4 depicts the optical layout of the FEMTOSOURCE XL 500. The Ti:sapphire crystal is cooled with a peltier element to -33°C to reduce t reduce the thermal lensing at the high pump powers and sits in a dry air system chamber to prevent condensation on the crystal end faces. The crystal is pumped with a diode intra-cavity frequency doubled continuous wave (CW) Nd:YVO_4 laser (Spectra-Physics Millenia XV, 532 nm, 12.2 W). The laser cavity is an x-folded configuration. The shorter arm of the cavity has a saturable Bragg reflector (SBR) which stabilises the mode-locked operation. The longer arm of the cavity includes a multi-pass cell type Herriott (MPC) which stretches the cavity length. The use of the long cavity length allows a decrease of

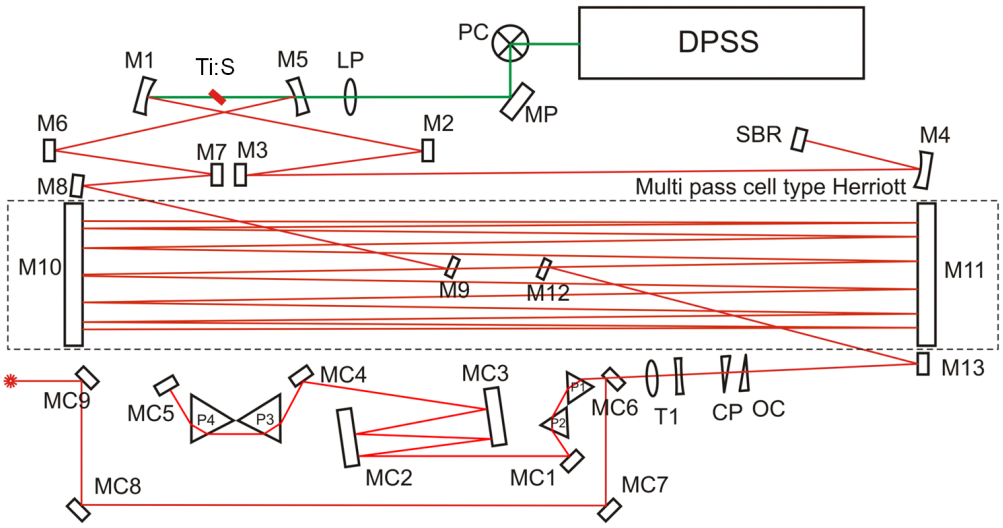

Figure 4.4: Schematic of the Ti:sapphire oscillator FEMTOSOURCE XL500 (image courtesy of Femtolasers GmbH). DPSS is the diode-pumped laser, Ti:S is the crystal, M# are the mirrors, SBR is the saturable Bragg reflector.

the laser repetition rate and an increase of the laser output pulse intensity. The beam makes 12 round-trip passes between the MPC mirrors and the cavity length is stretched to $\sim$ 30 m. Due to the long length of the cavity, the group velocity dispersion from the air is significant and causes a short pulse to spread in time. In order to generate femtosecond pulses, one has to compensate for dispersion by introducing a delay line. In the HPO system it is realised by 2 prism pairs (P1&P2, P3&P4) which extend the cavity length by 1.5 m. The pulse duration is measured by the autocorrelator and can be adjusted by translating the second prism pair. Figure 4.5 shows a typical output spectrum and the corresponding interferometric autocorrelation of the oscillator.

4.2.2 Optical train

The optical train permits shaping, modulating and preparing the beam for waveguide fabrication. It consists of a number of optical elements (Fig. 4.6, Fig. 4.7). At the output of the laser subsystem there is a motorised variable attenuator consisting of a zero-order half-wave plate and two polarising beam splitters. The half-wave plate is mounted on a rotation stage and therefore it allows adjustment of the laser power

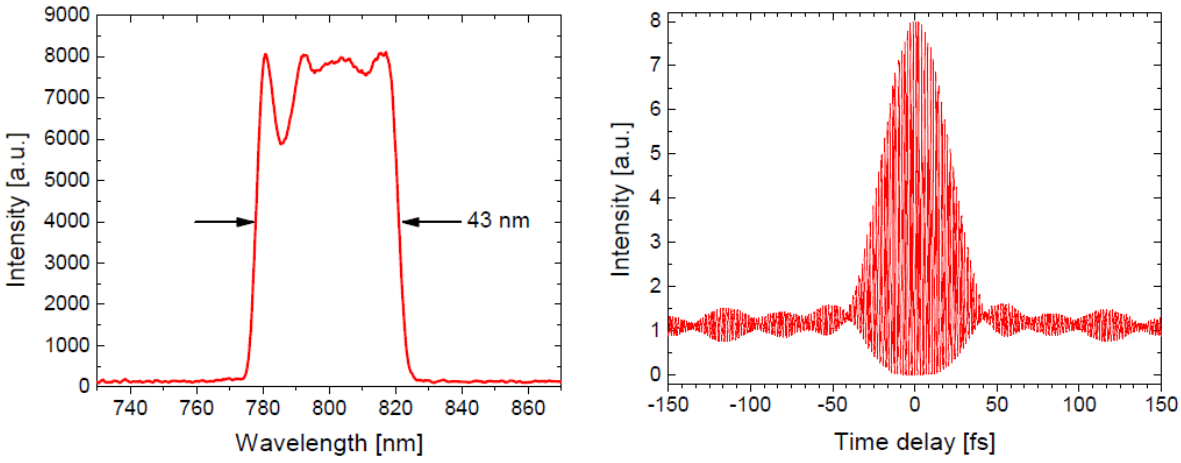

(a) Output spectrum. (b) Interferometric autocorrelation

Figure 4.5: Output spectrum of the oscillator showing the steep spectra edges that are typical for a chirped pulse oscillator, and the corresponding interferometric autocorrelation. The pulses are *sinc*-shaped due to the rectangular spectrum. Image courtesy: Dr. Simon Gross.

to the desired pulse energy for the fabrication process. A 2:1 telescope is used to reduce the beam diameter before it enters the pulse picker – Pockels cell, which has a clear aperture that is only 3 mm wide. The pulse picker is used when structures like waveguide Bragg gratings are being fabricated. More information on the grating fabrication is provided in Section 4.2.4.

A second telescope is placed after the pulse picker to increase the beam diameter. The magnification ratio (1:2, 1:2.5, 1:3, 1:3.5, 1:4, 1:5) is selected based on the desired numerical aperture of the objective lens which focuses the light into the sample. The type of the objective lens depends on the type of glass substrate in which the waveguides are inscribed and the type of the waveguides themselves. The second telescope is followed by a second zero-order half-wave plate and a polarising beam splitter which are required for pulse picking with the Pockels cell. The next component is a removable turning mirror. When the mirror is removed the beam is directed into an interferometric autocorrelator, which is used for characterising the pulse duration (Fig. 4.5b). When the mirror is up it sends the beam to a quarter-wave plate to produce circular

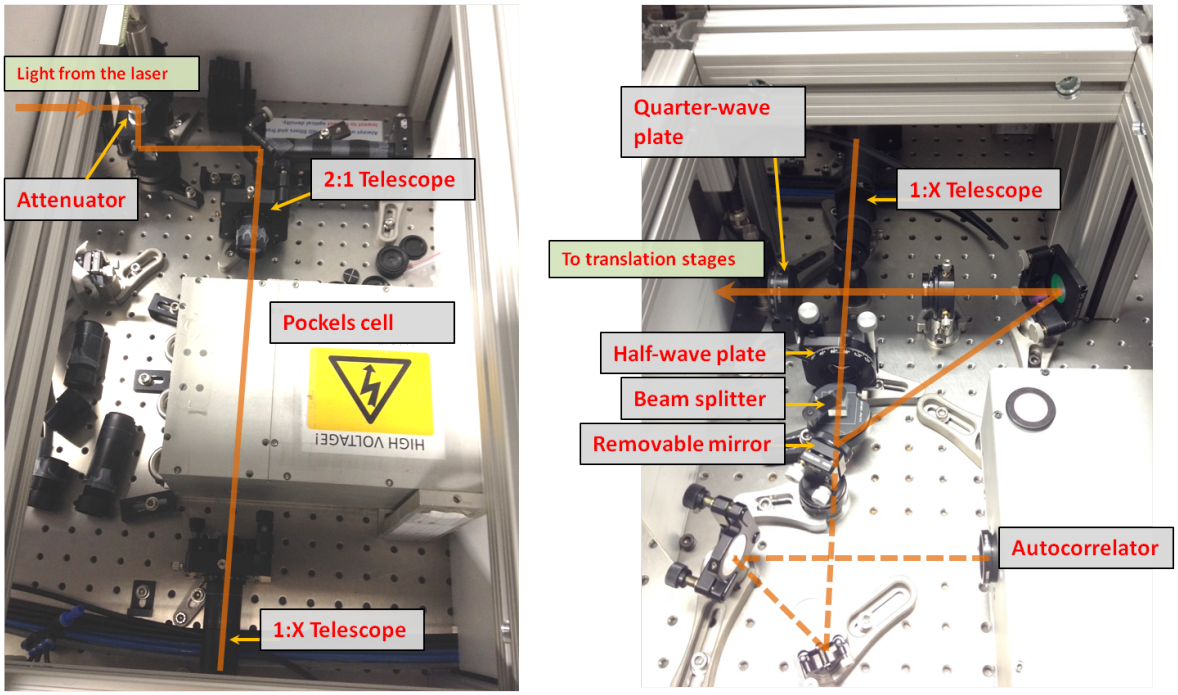

Figure 4.6: Photos of the optical train of fabrication setup and its optical beam path, which is indicated by the orange lines.

polarisation and then to a periscope, which directs the beam to a 45° dichroic mirror, the focusing objective and translation stages. The dichroic mirror enables the online monitoring of the fabrication process as it is highly reflective for the laser wavelength and transmissive for the visible. A Wollensak Raptar 15 cm f/4.5 lens and a Sony colour CCD CCTV camera form a vision system to monitor the fabrication process and aid alignment of the laser beam with respect to the sample. The sample is held by a vacuum chuck, which is attached to a mirror mount for aligning the sample's top surface parallel to the translation stage.

4.2.3 Stages

The stages are a crucial part of the laser writing system when writing complex photonic circuits. The glass sample is placed on a vacuum chuck which holds the sample in a stable position. The vacuum chuck is attached to a mirror mount, which permits the

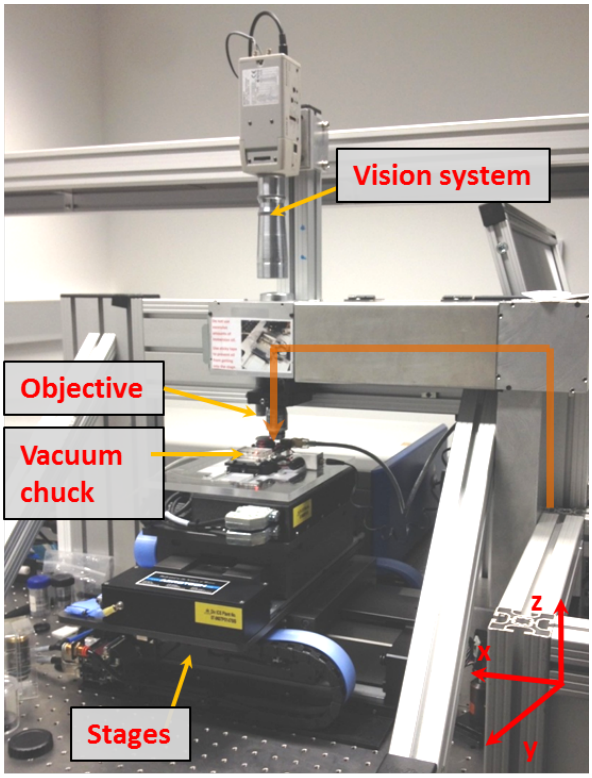

Figure 4.7: Photos of the optical train for the fabrication setup and the translation stages.

adjustment of the tip/tilt of the sample. Such assembly is placed on a set of high-precision XYZ linear Aerotech stages (Fig. 4.7). At the base of the setup there is an Aerotech ABL2000 air-bearing direct-drive linear stage which has 100 mm of travel range along the X axis. On top of it is a more compact Aerotech ABL1000 air-bearing direct-drive linear stage with 100 mm travel range along the Y axis. The top translation stage is an Aerotech WaferMax Z mechanical-bearing lift stage which moves the sample in the vertical direction (Z axis). Although the stage travel range along the Z axis is 5 mm, the waveguides can be written only within a vertical range of $\sim$ 400 µm. The limiting factor comes from the physical working distance of the objective which focuses the beam into the sample. Overall the waveguides and 3D optical circuits can be written within a volume of 100 $\times$ 100 $\times$ 0.4 mm^3. High precision, high accuracy and smoothness of both positioning and acceleration/deceleration of the stages is crucial to fabricate high quality, uniform waveguides which ultimately leads to high transmission

structures. It is especially important while writing at high speed as is the case in this work.

All stages are controlled by an Aerotech UNIDEX 500 system consisting of a PC-based motion controller and the interface software. The motion controller interprets the G programming language (G-code) which is a computer numerical control programming language. The G-code describes the theoretical trajectories and sends the commands to the translation stages. The motion control can move the stages in a velocity profiling mode which allows the contour type motion to blend consecutive motions into one continuous path. This function permits the inscription of smooth 3D waveguide structures.

4.2.4 Waveguide Bragg grating fabrication

The HPO system is also used to write the waveguide Bragg gratings using the point-by-point technique. The strong heat diffusion in the cumulative heating regime inhibits the fabrication of micrometre- or sub-micrometre sized structures of void-like nature, which are required for waveguide Bragg gratings. Therefore the setup is equipped with an external high-speed pulse picker to reduce the 5.1 MHz pulse repetition rate. The pulse picker consists of a rubidium titanyl phosphate (RTP) Pockels cell (Leysop Ltd., UK) capable of high speed switching. To fabricate the first order waveguide Bragg gratings at wavelengths around 1550 nm the repetition rate was reduced to 55.022 kHz and the translation speed set to about 1620 mm/min. The pulse energy had to be high enough to create micro-explosions and produce micro-voids. More details on the fabrication parameters are given in Section 6.4.

4.2.5 Pigtailing of the slit reformatting devices

Some of the slit reformatting devices were pigtailed to enable their use on a telescope with its fibre feed (see Chapter 7). A glass ferrule (~ 7 mm long and 127 µm of the inner diameter) and optical adhesive (Norland Optical Adhesive 61) were used to connect the sample and the multimode fibre. Figure 4.8 shows the pigtailing process. First the

coupling between the slit reformatting device and the multimode fibre is optimised, followed by inserting the glass ferrule on the end of the stripped fibre. The optical adhesive is applied from the end further away from the sample and the ferrule's tapered end and the glue fills the whole ferrule. While monitoring the coupling between the fibre and the sample, the UV curing is gradually applied and the fibre position adjusted as required. As an extra protection, the device is assembled on a supporting microscope slide.

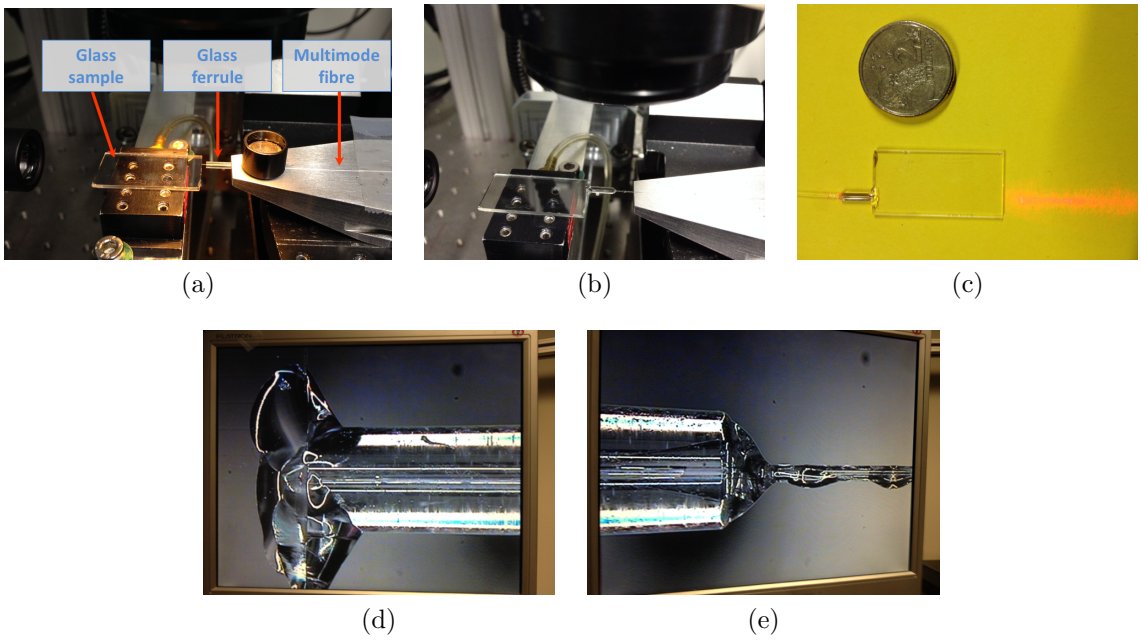

Figure 4.8: Sample pigtailing process: (a) optimising the coupling into the sample, (b) applying and curing the optical adhesive while monitoring the coupling, (c) pigtailed glass sample with injected red laser light, (d) close-up look of the connection between the sample and the glass ferrule, (d) close-up look of the connection between the fibre and the glass ferrule.

4.3 Device characterisation

After the waveguides are fabricated they undergo post-processing: grinding, to reveal the ends of the waveguides, and polishing, to improve the optical quality of the end facets. The devices are then ready to be tested and characterised: they are first visually inspected using a microscope to confirm that the waveguide geometry matches

the design, then characterised to quantify their physical and optical properties.

This section gives the details of the methods and techniques and a description of the equipment.

4.3.1 Optical microscopy

The fabricated waveguides were inspected visually using a transmission differential interference contrast (T-DIC) microscope (Olympus IX81). This microscope uses the beam-shearing interference technique and gains information from measuring very small optical path differences in the sample to enhance the contrast of transparent samples. Figure 4.9a shows the principles of the DIC technique. The technique requires the incident light to be polarised, therefore the light source is directly followed by a polariser. The Wollaston (or Nomarski) prism separates the light into two diverging orthogonally linearly polarised beams which are then focused into the sample by a condenser. The two beams are slightly separated (by the shear) and experience different optical path lengths while passing through the sample. The difference in the optical path originates from the difference in either the thickness or refractive index in the sample. When the light is focused again by an objective lens into the second Wollaston (or Nomarski) prism, the light is recombined into one beam (two beams once have again have the same polarisation) and interferes. The resulting image is characterised by bright and dark areas according to the optical path difference between. The second polariser is set orthogonal to the first polariser and removes the directly transmitted light.

The microscope is fitted with objectives of 5×, 10×, 20×, 40×, 100× and 150× magnification. It allows for bright field (no prism in the beam path) or DIC operation. The image can be viewed through the eye-piece or an Olympus DP72 camera which is capable of producing good quality micrographs, as will be shown in the next sections. Figure 4.9a shows the image of an Olympus IX81 microscope.

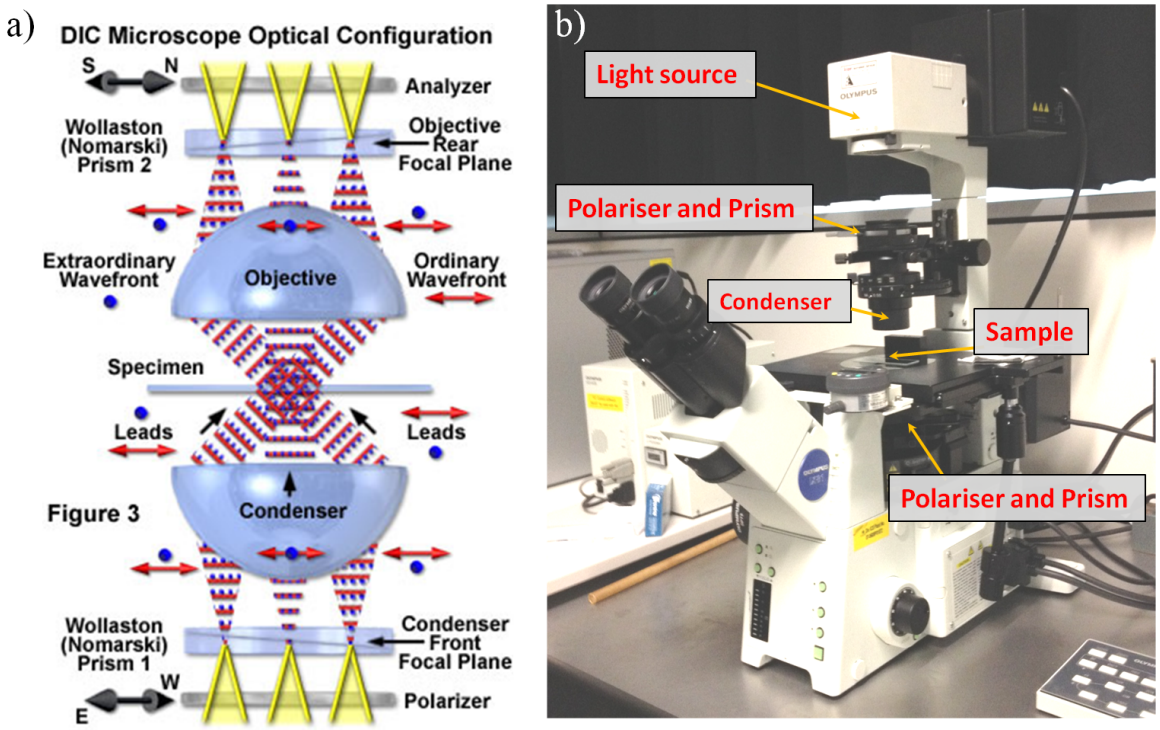

Figure 4.9: (a) Schematic (image courtesy of Olympus America Inc.) and (b) a photograph of the transmission differential interference contrast microscope Olympus IX81.

4.3.2 Photonic lanterns

The objective of the photonic lantern characterisation was the throughput measurements as a function of the injected focal ratio $F/\#$. This imposes two requirements on the system: (i) ability to control $F/\#$ of the injecting beam and (ii) ability to couple all the light emerging from the sample and isolate the guided light from the scattered beam. Both requirements prohibit the use of a typical waveguide/fibre characterisation setup, which is based on in/out fibre butt-coupling [73]. As a result a custom setup was developed.

The transmission properties of the photonic lanterns were characterised using the setup depicted in Fig. 4.10. An IR light emitting diode (LED) with a centre wavelength of 1550 nm and a FWHM bandwidth of 0.115 µm was used as the probe source (Thorlabs-LED1550E). It was driven by a 60 mA current source. The light was directly coupled into a 400 µm core diameter multimode fibre and the output of the fibre was

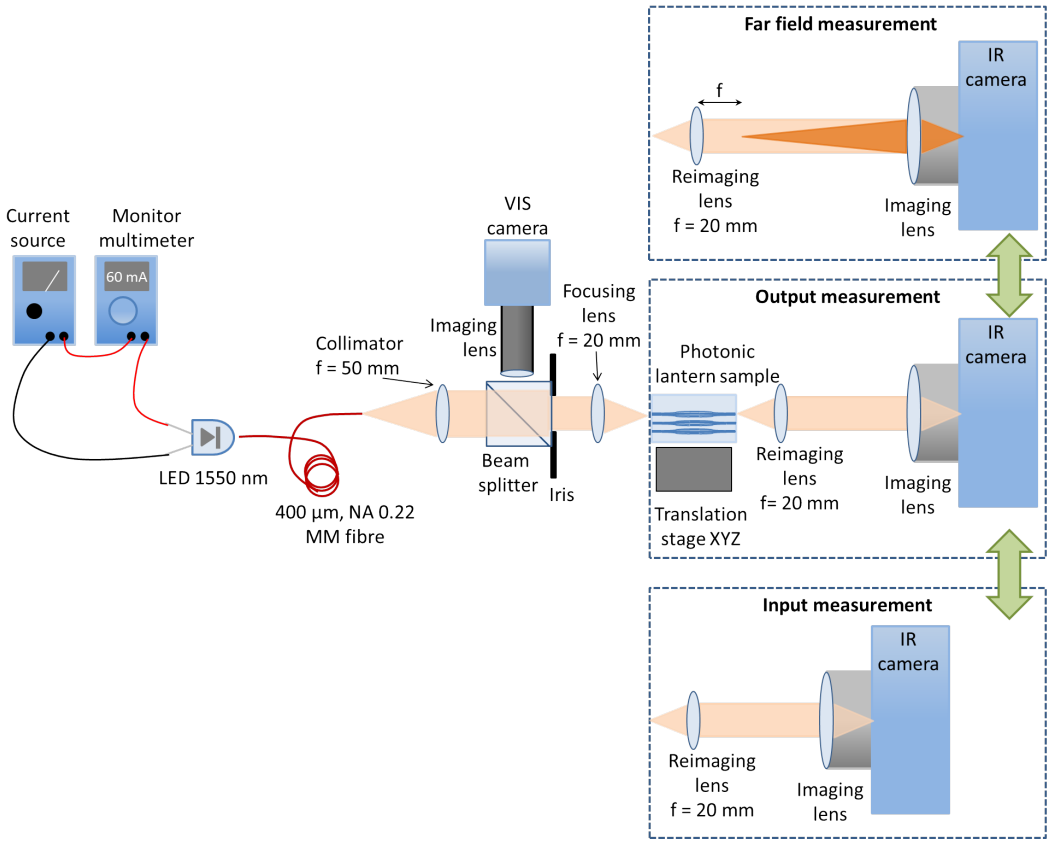

Figure 4.10: Schematic diagram of the setup for characterising photonic lanterns.

collimated with a 50 mm focal length IR achromat (Thorlabs-AC127-050-C). In order to control the focal ratio $F/\#$ of the injected beam, a calibrated iris (Thorlabs-SM1D12C) was placed in the collimated beam. A 20 mm focal length lens (Thorlabs LA5315) was used to focus the light into the sample. The sample was placed on an XYZ precision translation stage (Newport, M-462-XYZ-M). In order to align the sample with the injecting beam a cube beamsplitter (CM1-BS015) was placed in the collimated beam, so that a camera imaged the input facet of the glass sample. The IR LED was temporarily replaced with a green LED and the sample aligned until the image of the input beam (green spot) overlapped with the photonic lantern input. The sample was then moved away from the focusing lens to compensate for the chromatic aberrations of the lens. In order to perform throughput measurements the near-field output of the photonic lanterns was re-imaged onto an IR camera (FLIR SC7000) with a 20 mm focal length lens (Thorlabs LA5315). The normalisation was done by comparing near-field images

of the output of the photonic lantern (multimode output) and the input beam itself. For this step the photonic chip was removed and the re-imaging lens was moved toward the injection lens by the length of the chip.

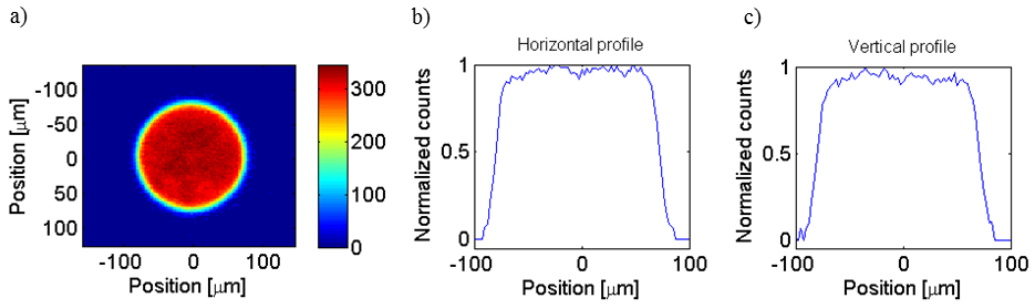

Figure 4.11: (a) Near field energy distribution of the launch field at the point of focus (input plane of the chip) for a $F/9$ beam and (b-c) its horizontal and vertical line profiles.

Measurements of the $F/\#$ of the launch (input beam) were carried out by using the assembly depicted in the top right of Fig. 4.10. The IR camera imaging lens was focused onto a plane 1 focal length behind the reimaging lens (its pupil plane), creating an image on the detector which represents the far-field of the probed beam. Dark frames were subtracted from the data initially and then the 90% encircled energy spot size was calculated for each image. The image scale was calibrated by means of a ruler placed in the same plane as the re-imaging lens. The numerical aperture NA was calculated as NA = spot size on the detector/(2 × focal length of the re-imaging lens). The $F/\#$ was determined by using Eq. 1.14.

4.3.2.1 Transmission analysis

The device throughput was computed by comparing the near field images of the photonic lantern (or slit reformatting device) and the input beam. The size of the input beam (Fig. 4.11) was larger than the size of the multimode input, therefore in order to calculate the correct input signal, a virtual aperture matching the input of the multimode waveguide ($\sim 54\,\mu m$) was applied to the input beam in data processing, which accounted for coupling losses due to the spot size mismatch.

The normalised throughput was rescaled to remove the effect of absorption by the Eagle2000 substrate, so that the true performance of the photonic lanterns could be assessed. Based on the 0.0065 mm^{-1} absorption coefficient in Eagle2000 at 1550nm [115], the maximum possible throughput for the 28.3 mm long sample was limited to 83.0%. As the final step, the throughput measurements were corrected for Fresnel reflection from two air/glass interfaces (in and out of the sample), each resulting in $\sim$4% loss for a glass refractive index of 1.4877.

4.3.3 Pigtailed slit reformatting devices

The pigtailed devices were characterised using the setup as described in section 4.3.2 with small changes as shown in Fig. 4.12. The free-space beam was injected into the bare fibre front of the multimode fibre (35 µm , NA 0.22) and the near-field of the output of the slit reformatting device was reimaged onto the IR camera (FLIR SC7000) for various injection $F/\#$. The following step was to cut $\sim$ 30 cm off the front of the fibre and replace the glass chip by the other end of the multimode fibre. Then the near-field of the end of the multimode fibre was reimaged onto the camera for appropriate $F/\#$. The throughput of the slit reformatting device was calculated as a ratio of the output of the slit reformatting device and the output of the multimode fibre. This procedure ensures that the injection to the fibre does not change and the calculated throughput represents only the losses of the slit reformatting device.

4.3.4 Grating devices

The photonic lantern with waveguide Bragg gratings devices were characterised using a setup as depicted in Fig. 4.13. The spectral response was measured using a swept wavelength system (SWS15100, JDS Uniphase). The system consists of the following components: tunable laser with a range between 1520 nm and 1570 nm and a resolution of 3 pm, source module, polarisation controller to enable polarisation dependent loss

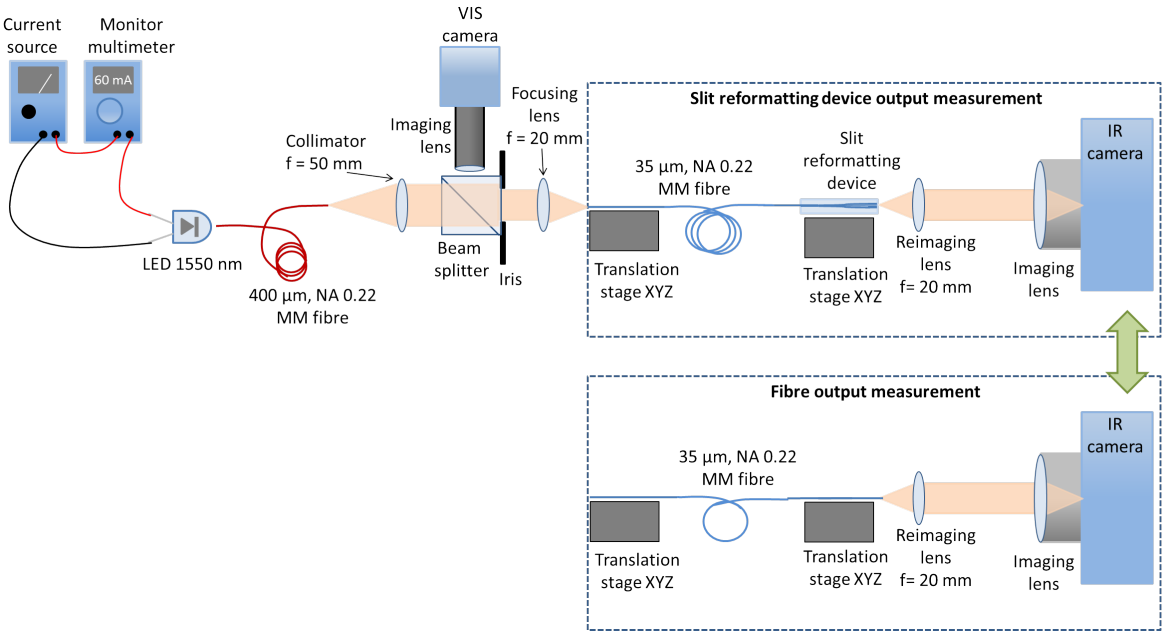

Figure 4.12: Schematic diagram of the setup for characterising the 1×7 pigtailed slit reformatting device.

measurement, and detector unit. The light is coupled into a SMF28 fibre and propagates through a 3-port circulator, which acts as an optical insulator. The mode-field-diameter of SMF28 fibre is 10.4 µm, whereas the multimode input diameter is ∼ 50 µm. To ensure even illumination of the multimode input the output of the SMF28 fibre was reimaged and magnified by means of free-space optics consisting of two lenses of focal lengths of 3 mm and 15 mm, to match the size of the input multimode waveguide. The transmitted light was collected with a 100 µm multimode fibre pigtail and fed into one of the ports of the detector of the swept wavelength system.

The characterisation setup also permits the measurement of the part of the spectrum that was reflected by the sample, by recording the signal going to the 3rd port of the circulator and another port of the detector of the swept wavelength system. The devices presented here were however characterised only in transmission. Prior to performing measurement the system was calibrated for transmission by bypassing the sample with an optical fibre patch cord.

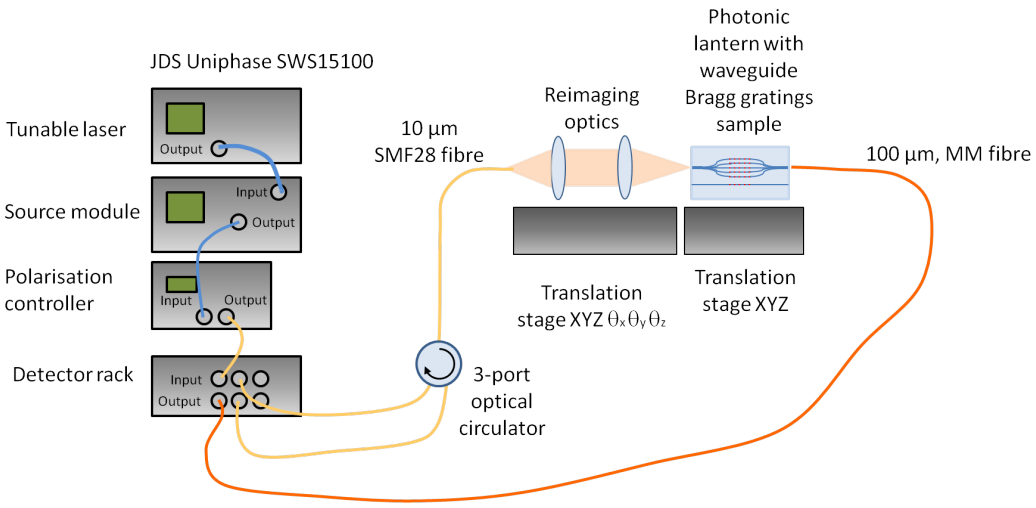

Figure 4.13: Schematic diagram of setup for characterising photonic lanterns with waveguide Bragg gratings.

5

Photonic lantern fabrication and characterisation

The feasibility of photonic lanterns fabricated with the femtosecond laser inscription has been demonstrated by Thomson et al. [10] but the devices exhibited relatively high losses and their transmission must be improved for astronomical applications. They identified the possibility of reducing the losses with careful optimisation of the fabrication process. However, the laser system used by Thomson et al. operates in the multi-scan, non-cumulative heating regime, which requires a relatively long time for fabrication of a single device (~ 2 hours [10]). Therefore the optimisation of the fabrication process by writing multiple devices is not feasible. By capitalising on the high writing speed of the HPO laser system (~ 3 s per waveguide, ~ 2 minutes per device) that we are using, it is possible to produce multiple devices and therefore

perform a detailed parameter scan to find the optimal low-loss design. Based on the modelling and simulations results presented in Chapter 3, a range of devices were fabricated and characterised.

This chapter focuses on investigating an optimal design for two types of devices operating at 1550 nm: back-to-back photonic lanterns and slit-reformatting devices. First, devices with different transition lengths separating the multimode and single-mode sections in a photonic lantern were explored, followed by a study investigating the transverse separation between waveguides in the multimode section on the device throughput. Finally, a range of slit-reformatting devices with a variable separation between the single-mode waveguides in the slit end were fabricated to examine their optimal design.

5.1 Fabrication parameters

All the devices were written using the HPO system (5.1 MHz repetition rate, < 50 fs pulse duration, 800 nm central wavelength). The waveguides were written with a pulse energy of 35 nJ at a translation velocity of 750 mm/min in order to create waveguides which were single-mode at 1550 nm. The laser was focused into a 30-mm-long alkaline earth boro-aluminosilicate (Corning Eagle2000) glass sample using a $100\times$ oil immersion objective lens Zeiss N-Achroplan, NA $= 1.25$, working distance $= 450$ µm. The waveguides were written from the bottom to the top, so that for each waveguide the laser beam is focused in a uniform refractive index glass sample as shown in Fig. 5.1. All throughput measurements were performed and analysed as described in Sections 4.3.2.

5.2 Transition length

In order to simplify the characterisation process, the structures comprised multimode - single-mode - multimode (MM-SM-MM) sections and two transition sections with length varying between 1 and 10 mm, as depicted in Fig. 5.1b. The pitch in the MM

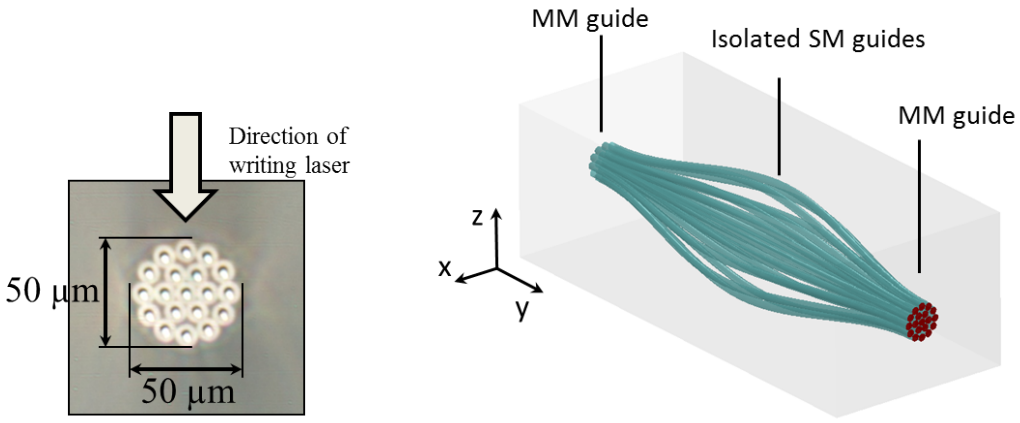

(a) (b)

Figure 5.1: (a) Microscopic image of the MM input of the photonic lantern and (b) CAD model of the back-to-back photonic lantern (MM-SM-MM)

section was set to 10 µm and the isolated waveguides separation to 37.5 µm. The front MM section and middle SM section were both 2 mm long; the length of the back MM section varied from 4 mm to 22 mm for transition lengths of 10 mm down to 1 mm. The throughput measurements were corrected for the glass absorption, Fresnel reflection and coupling (cf. Section 4.3.2.1). The normalised throughput as a function of the injected $F/\#$ for fabricated devices is shown in Fig. 5.2. For the reader's convenience we also reproduced the modelling results for a cosine type of transition from Section 3.5.2. The modelling results were squared (comparing Fig. 3.10) to present the throughput of a device with double transition. The experimental data show a similar trend to the theoretical data, i.e. the throughput strongly increases with increasing transition length up to 4-5 mm and then stabilises. In the experimental case the sampling set was too small to make detailed comparison with simulation results but nevertheless the overall functional form matches closely.

We expect essentially no light to couple into the guides beyond $F/4$, which is the cutoff $F/\#$ corresponding to the peak core Δn of 5×10^{-3}. For this reason, we did not make any measurements below F/4. The average Δn is 1.3×10^{-3} which corresponds to a cutoff of $F/9$ shown by Jovanovic et al. [1]. The increasing throughput between $F/4$ and $F/11$ is due to the smoothly increasing coupling of higher angles into

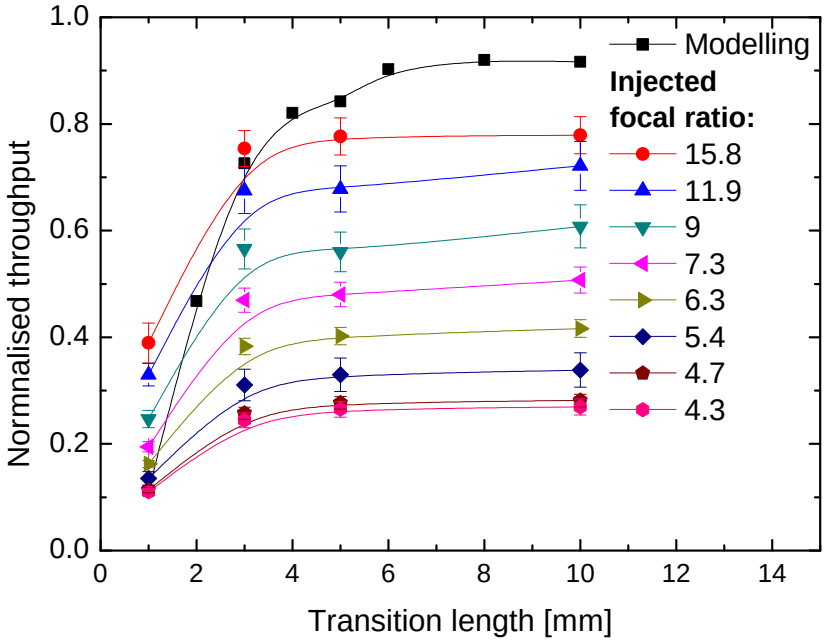

Figure 5.2: Normalised throughput of a back-to-back photonic lantern as a function of transition length for various injection $F/\#$ probed at 1550 nm.

our complicated multimode guide refractive index profile. The normalised throughput levels off at 0.77. Based on the modelling, the maximum expected throughput (in the case of no phase errors) for a double (MM-SM-MM) transition is 0.92 (0.96 squared). For the case where phase errors are present from either waveguide inhomogeneities or optical path differences between the waveguides, the main source of loss comes from coupling 19 modes in the SM section into a MM section which only supports 12 modes.

5.3 Waveguide separation in multimode section

A set of photonic lanterns, composed of MM-SM-MM sections and two transition sections of a fixed length of 10 mm were inscribed with varying pitches in the MM section ranging from 7 to 15 µm in order to investigate how well individual SMs couple back into the MM waveguide. Figure 5.3 summarises the normalised throughputs as a function of the injected $F/\#$. This figure shows that the throughput increases as a function

of pitch until it reaches a peak at 13 µm. Above this pitch the throughput seem to decrease. The reason for the throughput increase up to 13 µm is that, as we showed in Fig. 3.12, the 13 µm pitch supports almost all modes (17 out of 19). The throughput decreases for structures of a pitch > 13 µm, as the evenly illuminated input light does not couple fully to the spatial profile of the input. In addition we can see that the throughput also increases as the $F/\#$ value is elevated. This is predominantly due to the fact that the coupling efficiency is a function of $F/\#$ and high $F/\#$ couples better to the structures. The refractive index of the individual waveguides forming the multimode waveguides is complicated (cf. Fig. 3.7) and the effective waveguide area is larger for low NA (low Δn) than for large NA (high Δn, i.e. the waveguide cores only). As a result the throughput does not fully stop increasing above $F/8$. The throughput increases up to $F/15$ but slower than below to $F/8$. The smooth trend of the normalised throughputs across the multimode pitch displays slight discrepancies; these most probably originate from the minor physical differences between the waveguides inherent in the fabrication process.

5.4 Slit reformatting devices for diffraction-limited spectrographs

An ideal application for the photonic lantern is to convert the multimode light into single-mode light and then reformat it into a slit to be directly injected into a spectrograph [6, 29, 118, 119]. The slit reformatting device, which consists of a MM input, a transition section and isolated SM tracks which are remapped to a linear slit of SM waveguides is shown in Fig. 5.4a. Figure 5.4b shows a conceptual illustration of the spectra produced from a multiple SM-waveguide slit as viewed on a CCD detector. The figure depicts the architecture for optimum detector sampling.

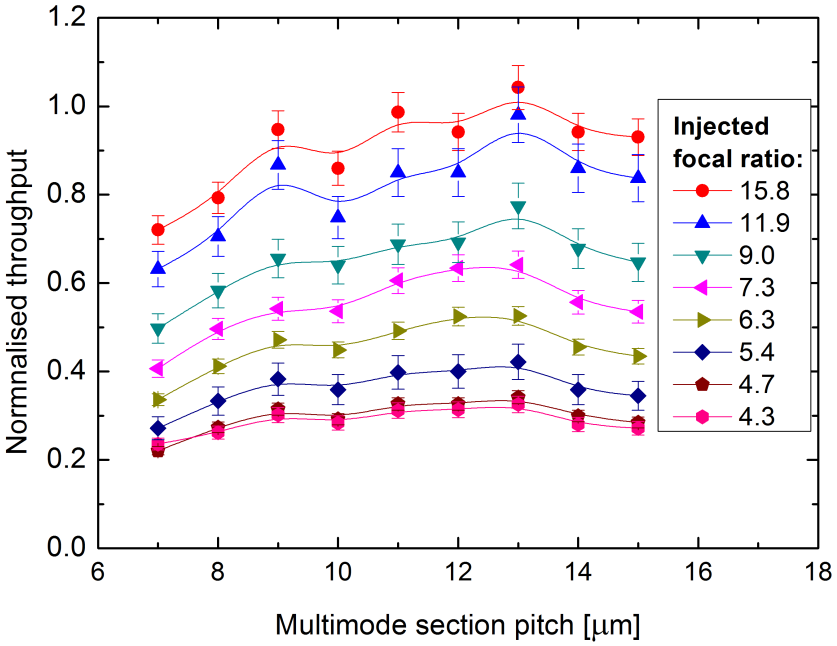

Figure 5.3: Normalised throughput of a back-to-back photonic lantern as a function of MM pitch for various injection $F/\#$ probed at 1550 nm.

5.4.1 Performance of the slit-reformatting devices

A set of slit-reformatting devices was inscribed with different spacing between the SM waveguides in the slit end, i.e. slit pitches ranging from 7-17 µm. The input MM pitch was set to 10 µm and the length of the two transition sections was set to 10 mm. The normalised throughputs of the structures as a function of the injected $F/\#$ and the slit pitch are presented in Fig. 5.5. The maximum normalised throughput is obtained for slit pitches ≥ 13 µm. This coincides with the theoretical value discussed earlier as the part of the design of the slit reformatting devices (Fig. 3.12, Section 3.7). Most notably it can be seen for slow beams (high $F/\#$) that have fewer spatial modes, that the normalised throughput is $\sim 100\%$ to within uncertainty at 1550 nm. This means that aside from the coupling and absorption losses the MM to SM conversion and reformatting is near lossless.

The high efficiency of devices with 13 µm separation between tracks in the slit means

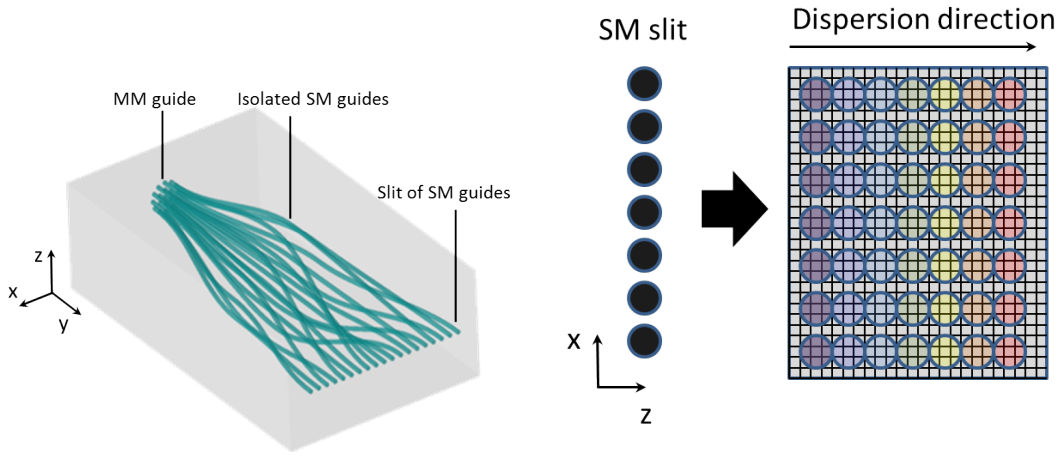

(a) (b)

Figure 5.4: (a) A CAD model of a slit-reformatting device for a diffraction-limited spectrograph. Three key regions are highlighted; the MM guide that collects the seeing-limited light from the focus of the telescope, the isolated SM guides and the slit formed from the SM guides. (b) Conceptual illustration of the spectra viewed on a CCD detector produced by a long thin SM slit. The sampling required from the Nyquist sampling theorem should be at least 2.4 pixels per resolution element (3 pixels in the diagram). A SM-waveguide slit allows for optimal use of the detector area.

that the total slit size would be $\sim 12\,\mu m$ (mode field diameter) $\times\, 240\,\mu m$ (slit length), in contrast to the similar device based on 19 standard SMF28 fibres with 125 µm cladding, which would be $\sim 10.5\,\mu m$ (mode field diameter) $\times\, 2400\,\mu m$ (slit length), so a factor of 10 along the slit. As a result, the higher density of the waveguides will allow for better utilisation of the detector area.

5.5 Conclusions

We have evaluated the design and fabricated a series of photonic lanterns and slit reformatting devices in order to find a recipe for low-loss devices. The simulations showed that out of linear, cosine and raised sine bend types the cosine one has the lowest losses. The throughput measurement showed that devices with a MM-SM transition as short as 4-5 mm are practical and exhibit efficiencies at the 75% level (62% if including glass absorption losses). The study of the pitch of the MM section demonstrated that

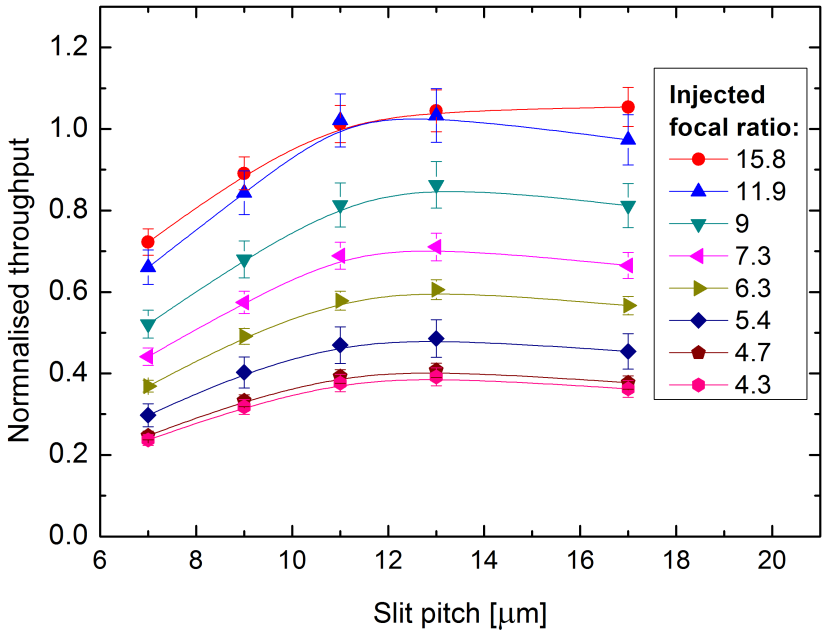

Figure 5.5: Normalised throughput for the slit reformatting device for various slit pitches (separation between SM waveguides in the slit end) as a function of the injected $F/\#$ probed at 1550 nm.

it is critical to optimise the pitch for efficient coupling. In our case this corresponded to a pitch of $\geq 13\,\mu m$ which supported all the modes. In addition, we minimised the length of the slit in the reformatting device by using a 13 µm pitch which made the slit multimode and maintained the throughput of 95% for $F/\#>12$ when excluding glass absorption losses and 82% for $F/\#>12$ when including glass absorption losses.

The promising performance of the integrated photonic lanterns and slit reformatting devices opens up the possibility of using them to deliver the light from the telescope focus to single-mode spectrographs, either in the form of integrated photonic spectrographs or bulk optics-based single mode spectrographs. Now that efficient photonic lanterns can be realised in an integrated platform, astrophotonic devices can be greatly miniaturised and hence made more thermally and environmentally stable. Such an instrument can greatly enhance the efficiency and performance of seeing-limited telescopes.

6

Photonic lanterns with waveguide Bragg gratings

The fabrication of fibre photonic lanterns incorporating fibre Bragg gratings for atmospheric OH filtering has proven to be expensive and/or challenging. There have been two methods investigated so far. The first one requires multiple, individually fabricated FBGs, which are then spliced to the single-mode ends of a photonic lantern [46]. However, this technique is complex, expensive and labour-intensive. The second approach is to write the gratings simultaneously across all the cores in a multi-core fibre and then taper down its ends to create a back-to-back photonic lantern. Such an approach shows promise but has thus far not been demonstrated at a satisfactory level [48, 52, 53]. The main issue is that each of the single-mode fibre gratings exhibits a different response in terms of the Bragg wavelength and grating strength, as illustrated

in Fig. 6.1. This non-uniformity is attributed to the refraction of the focusing beam by the curved fibre surface as well as by the intermediate cores. Even though it has been shown that the FBG inscription in all cores of a multi-core fibre is possible, significant further work is required to improve the uniformity of the FBG characteristics in order to be suitable for astronomical applications.

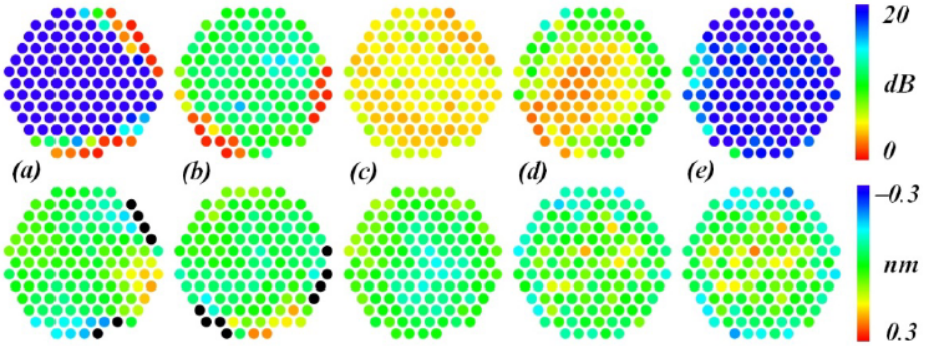

(a)

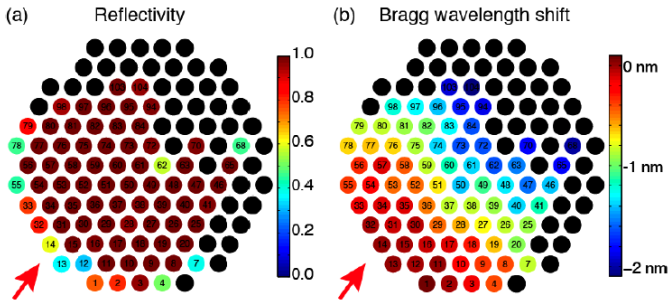

(b)

Figure 6.1: Notch characteristics of the FBGs fabricated in multi-core fibres consisting of 120 single-mode cores using (a) a UV phase mask writing process [48], and (b) a femtosecond phase mask laser inscription [52].

Waveguide Bragg gratings (WBGs) are one of the many devices which can be fabricated with the femtosecond direct-write technique. At this stage several groups have reported strong WBGs in the telecommunication C-band [61, 76, 101, 120]. However, devices integrating multiple WBGs of the same spectral characteristics have not been reported before, therefore the reproducibility of WBGs was unknown. Benefiting from the ability of the femtosecond laser system to write both 3D optical circuits and WBGs [76, 101], photonic lanterns with WBGs were fabricated to test the reproducibility of

WBGs and verify the possibility of a fully integrated device for spectral filtering of multimode light.

This chapter presents the results of 1×19 integrated photonic lanterns with multi-notch waveguide Bragg gratings. Firstly, the background of the waveguide Bragg gratings is given, followed by the details of the device fabrication and results. Finally, applications for the devices are proposed.

6.1 Waveguide Bragg gratings – background

Waveguide Bragg gratings (WBG), similarly to fibre Bragg gratings, consist of periodic modifications of the refractive index along the waveguide core. The primary application for waveguide Bragg gratings has been to realise monolithic integrated waveguide lasers, where WBGs replace the discrete mirrors or thin-film coatings, and together with a straight waveguide between the WBGs they form the laser cavity.

The refractive index modification in WBGs is introduced by femtosecond laser pulses. There are two main approaches to the fabrication: (i) point-by-point method and (ii) square-wave modulated pulse train method, as illustrated in Fig. 6.2.

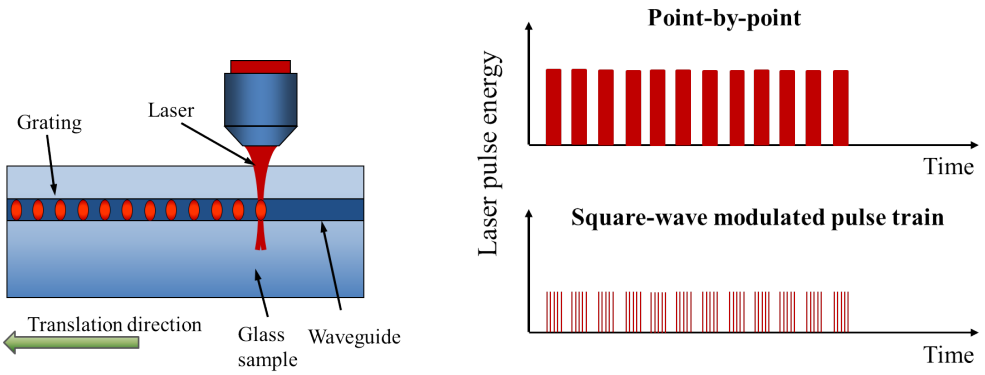

Figure 6.2: (a) Illustration of the waveguide Bragg gratings written with a femtosecond laser; (b) illustration of the laser pulse delivered to the glass for point-by-point and square-wave modulated pulse train methods.

The point by point method is a two-step process, where first a waveguide is created and then overlaid with a grating modification [61, 121]. Each of the laser pulses creates

one grating period and the Bragg wavelength λ_B is regulated by the stage translation speed, according to the Bragg equation:

$$\lambda_{\mathrm{B}} = 2 \cdot n_{\mathrm{eff}}\Lambda = \frac{2n_{\mathrm{eff}} \cdot v_{\mathrm{trans}}}{f_{\mathrm{rep}}}, \tag{6.1}$$

where Λ is the grating period, v_{trans} is the translation velocity of the stage, f_{rep} repetition rate and n_{eff} is the effective refractive index. In order to create high enough refractive index contrast in one pulse, the laser beam has to be tightly focused and the laser pulse energy has to be relatively high, which results in the creation of micro-voids. Such gratings were shown for the first time shown by Marshall et al. [61] in fused silica.

The second approach, the square-wave modulated pulse train method, is a single-step process. It uses an acousto-optic modulator to modulate the incoming beam and create windows when bursts of the laser pulses are transmitted. By using a slow translation speed, the multiple modifications partially overlap and build up a strong refractive index modification. Such gratings have been demonstrated in phosphate glass [62, 122] and fused silica [120].

Although WBGs have been mostly fabricated in the kHz regime, Miese et al. [101] showed the possibility of their fabrication in borosilicate glass using a 5.1 MHz laser repetition rate and the square-wave modulated pulse train method. Recently Gross [76] fabricated point-by-point WBGs in borosilicate glass using a 5.1 MHz pulse repetition rate to fabricate the waveguides and a reduced the repetition rate (55.022 kHz) to fabricate the gratings.

6.2 Waveguide Bragg gratings efficiency

The strength of the waveguide (or fibre) Bragg grating depends on two parameters: (i) the length of the grating along the fibre and (ii) the coupling constant κ, according to the equation [76]:

$$R_{\mathrm{max}} = \tanh^2(\kappa L), \tag{6.2}$$

where $R_{\max}$ is the maximum reflectance, L is the length of the grating and κ is the coupling constant, which is usually expressed in cm^{-1}. The strength of the grating can be tailored by adjusting these two values. The coupling constant is a quantity depending on the overlap between the mode propagating in the fibre with the index perturbation and the magnitude of the index perturbation. The amount of the overlap between the mode and the perturbation can be changed by modifying the geometry of the grating in the direction perpendicular to the propagation direction. The magnitude of the grating depends on the index contrast between the core and perturbation. Because of the relatively high absorption of the glass of choice in the IR range [115], the length of the grating should be kept short and the coupling coefficient should be optimised to find the maximum reflectance.

6.3 Coupling coefficient optimisation

Prior to fabricating the back-to-back lantern devices, a pulse energy scan was performed in order to determine the optimal pulse energy for grating inscription. A set of WBGs in single-mode waveguides was written with pulse energies of 100, 150, 200, 250 and 300 nJ, chosen based on a previous study [76]. Figure 6.3 shows the grating strength of the 20-mm-long WBGs and the corresponding coupling strength κ. The strongest Bragg-resonances were obtained with 100 nJ and 150 nJ energy, resulting in 14 dB and 15 dB deep transmission dips and κ values of $1.15\,\mathrm{cm}^{-1}$ and $1.20\,\mathrm{cm}^{-1}$, respectively. Therefore 125 nJ pulse energy was chosen for the gratings presented in this work. It is worth mentioning that the gratings are operating in a strong grating regime [76], hence the length of the grating does not affect the grating bandwidth.

6.4 Devices fabrication

The fabricated chip contains multiple devices, each consisting of back-to-back lanterns with a horizontal array of straight waveguides in the middle as illustrated in Fig 6.4. Each photonic lantern is composed of 19 individual SM waveguides which are brought

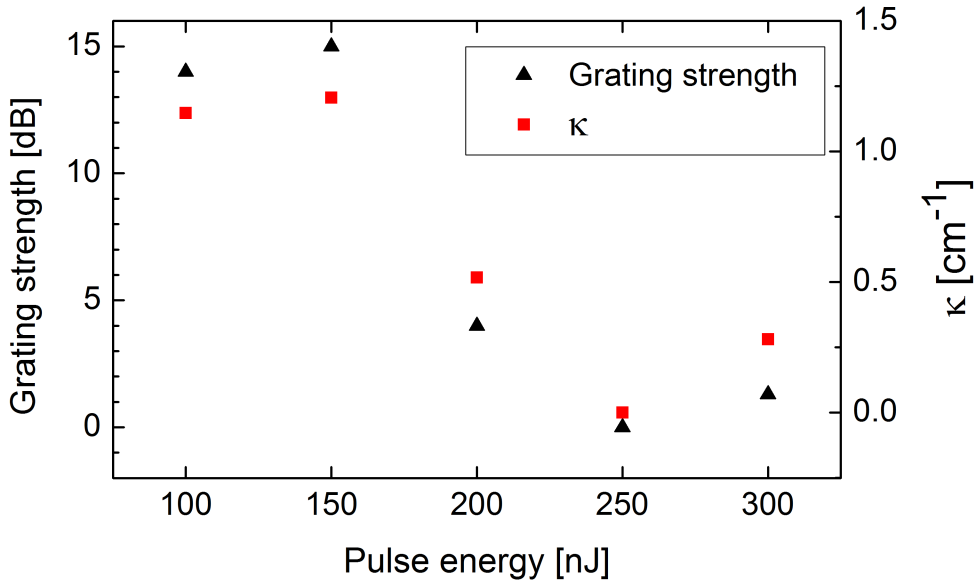

Figure 6.3: Strength of the transmission dip and κ as a function of the pulse energy for 20-mm-long single WBGs.

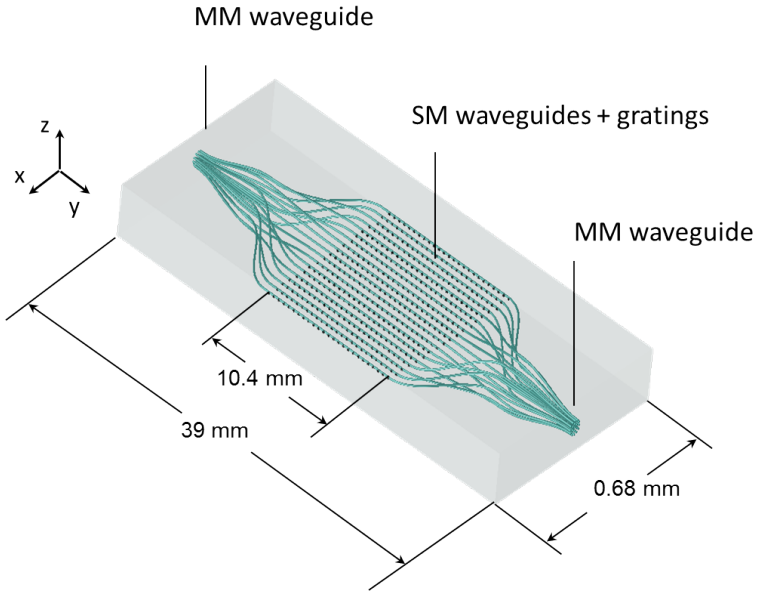

Figure 6.4: CAD drawing of the back-to-back photonic lantern device with the waveguide Bragg gratings with indicated dimensions.

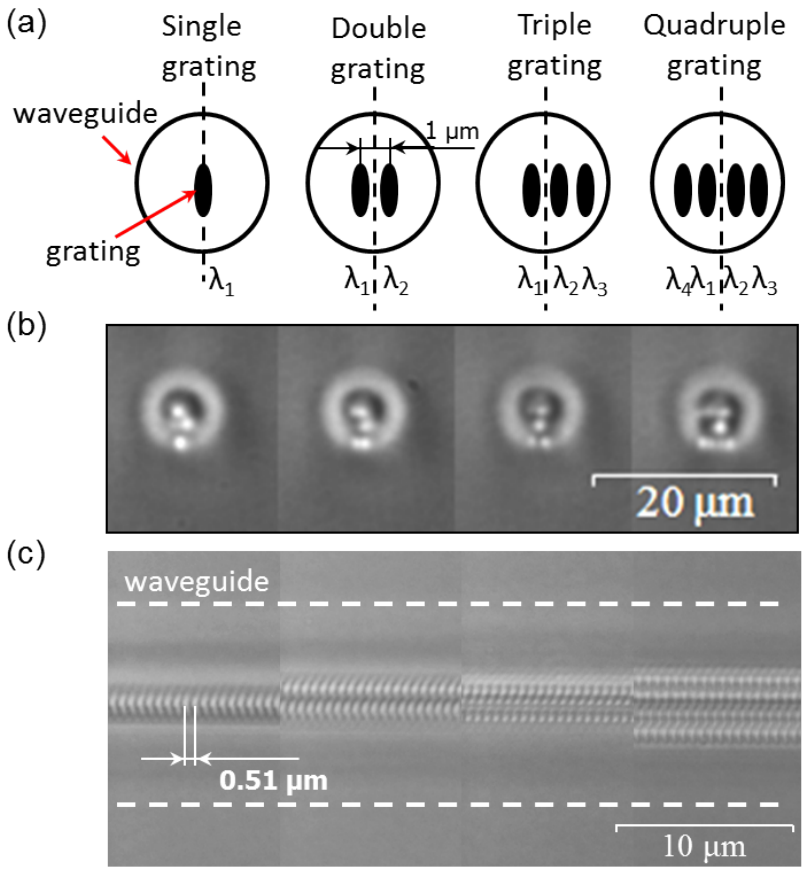

Figure 6.5: (a) Sketch of the cross-section of the waveguides (circles) with the gratings (ellipses) with indicated position of the centre of the waveguide (dotted line); $\lambda_1 = 1545\,\text{nm}$, $\lambda_2 = 1552\,\text{nm}$, $\lambda_3 = 1559\,\text{nm}$, $\lambda_4 = 1563\,\text{nm}$; microscope images of the SM waveguides seen from the (b) front and (c) top with one, two, three and four gratings.

close to each other to form the MM waveguide input [1]. These 19 waveguides then fan out into a horizontal array of straight isolated SM waveguides. Each SM waveguide either contains one, two, three or four gratings with different Bragg resonances placed next to each other in the SM waveguide core (Fig. 6.5(a)). The SM waveguides were placed 37.5 µm apart, which is a minimal distance for isolating the waveguides. The total chip length of 39 mm includes: 2-mm-long MM waveguides at both ends, 12-mm-long transitions from MM waveguides to the horizontal array of straight SM waveguides and the 10.4-mm-long straight WBG section in the middle. The WBG section was chosen to be shorter than in the test WBGs (Section 6.3) in order to accommodate the

entire photonic lantern in a 40-mm-long glass sample with maximising the bend radius of the waveguides and maximising the length of the WGB. As a result the minimal bend radius in the devices is 30 mm.

The devices were inscribed into a boro-aluminosilicate glass (Corning Eagle2000) as described in Chapter 4. A 100× 1.25 numerical aperture (NA) oil immersion objective (Zeiss N-Achroplan) was used to focus the circular polarised laser beam 300 µm below the sample's top surface. The photonic lantern structures were written in the cumulative-heating regime with the laser's repetition rate of 5.1 MHz at a pulse energy of 35 nJ and a translation speed of 750 mm/min. In a second step following the waveguide inscription, the laser repetition rate was reduced to 55.022 kHz with an external electro-optic pulse picker to place point-by-point modifications for the gratings into each of the SM waveguides. Due to the high focusing NA, the point-by-point features are only ∼1×4 µm in cross section, multiple gratings can then be placed side-by-side spaced by 1 µm within the ∼ 10 µm diameter SM waveguide, as shown in Fig. 6.5 (a, b, c). The gratings were fabricated with a pulse energy of 125 nJ as found in section 6.3. Using Equation 6.1, the period and therefore the Bragg wavelength (λ_B) of the gratings was tuned by changing the translation speed of the stages according to,

$$v_{\text{trans}} = \frac{\lambda_B \cdot f_{\text{rep}}}{2 \cdot n_{\text{eff}}}, \tag{6.3}$$

where v_{trans} is the stage translation velocity, f_{rep} is the repetition rate and n_{eff} is the effective refractive index. In this fashion four photonic lantern structures were written with single ($\lambda_B = 1545$ nm), double ($\lambda_B = 1545$ nm & 1552 nm), triple ($\lambda_B = 1545$ nm, 1552 nm & 1559 nm) and quadruple ($\lambda_B = 1545$ nm, 1552 nm, 1559 nm & 1563 nm) WBGs. The typical translation speed was 1620 mm/min (27 mm/s), hence the fabrication process of the triple grating photonic lantern took ∼ 6 minutes.

6.4.1 Device performance

In order to quantify the spectral performance of the photonic lanterns, identical WBGs were inscribed into isolated SM waveguides for reference purposes. The devices were

spectrally characterised using a swept wavelength system (SWS15100, JDS Uniphase) with 3 pm resolution. To ensure even illumination of the MM input ($\sim 50\,\mu m$) the light was free-space coupled into the chip with a focal spot size on the order of the input MM waveguide diameter. The transmitted light was collected with a MM fibre and fed into the detector of the swept wavelength system.

Figures 6.6 and 6.7 show the normalised transmission spectra of the 19-channel photonic lanterns and the reference SM waveguide with 10.4-mm-long first order gratings at 1545 nm (Fig. 6.6(a)), 1552 nm (Fig. 6.6(b)), 1559 nm (Fig. 6.7(a)) and 1563 nm (Fig. 6.7(b)). Table 6.1 summarises the transmission dip strength for the gratings. As seen from the figures and the table, the gratings in the photonic lanterns exhibit a similar performance to the gratings in the reference SM waveguide. This result proves an efficient and symmetrical performance of each of the gratings in the photonic lantern, which demonstrates that the femtosecond direct-write process provides excellent reproducibility. In contrast, the fibre Bragg gratings so far inscribed into multi-core fibres [48] suffer from non-uniform strength and resonance wavelengths across the different cores. These effects are attributed to problems with achieving a uniform illumination of all the cores during the fabrication process.

The strongest resonances for our gratings are obtained from the modifications located closest to the centre of the core because of the strongest overlap with the guided mode (i.e. 1545 nm and 1552 nm as seen in Fig. 6.5(a)). However an optimised arrangement of the grating modifications could be used to obtain more even resonances. For the layout of modifications in the waveguides used in this work, the triple grating photonic lantern offered the best performance as it exhibited strong transmission dips simultaneously at multiple wavelengths. Slight Bragg wavelength shifts are present (Fig. 6.6(a)). This is consistent with the expected change in the guided mode's effective index n_{eff} as more gratings are placed within the waveguide cores. The FWHM of the grating resonances are in the order of 0.1 nm, and as such sufficiently narrow to be used for OH emission filtering [46]. The number of filter lines could be increased by inscribing complex aperiodic [45], amplitude- or phase-sampled WBGs [123].

Figure 6.8 presents normalised transmission spectra of multiple notches for the triple

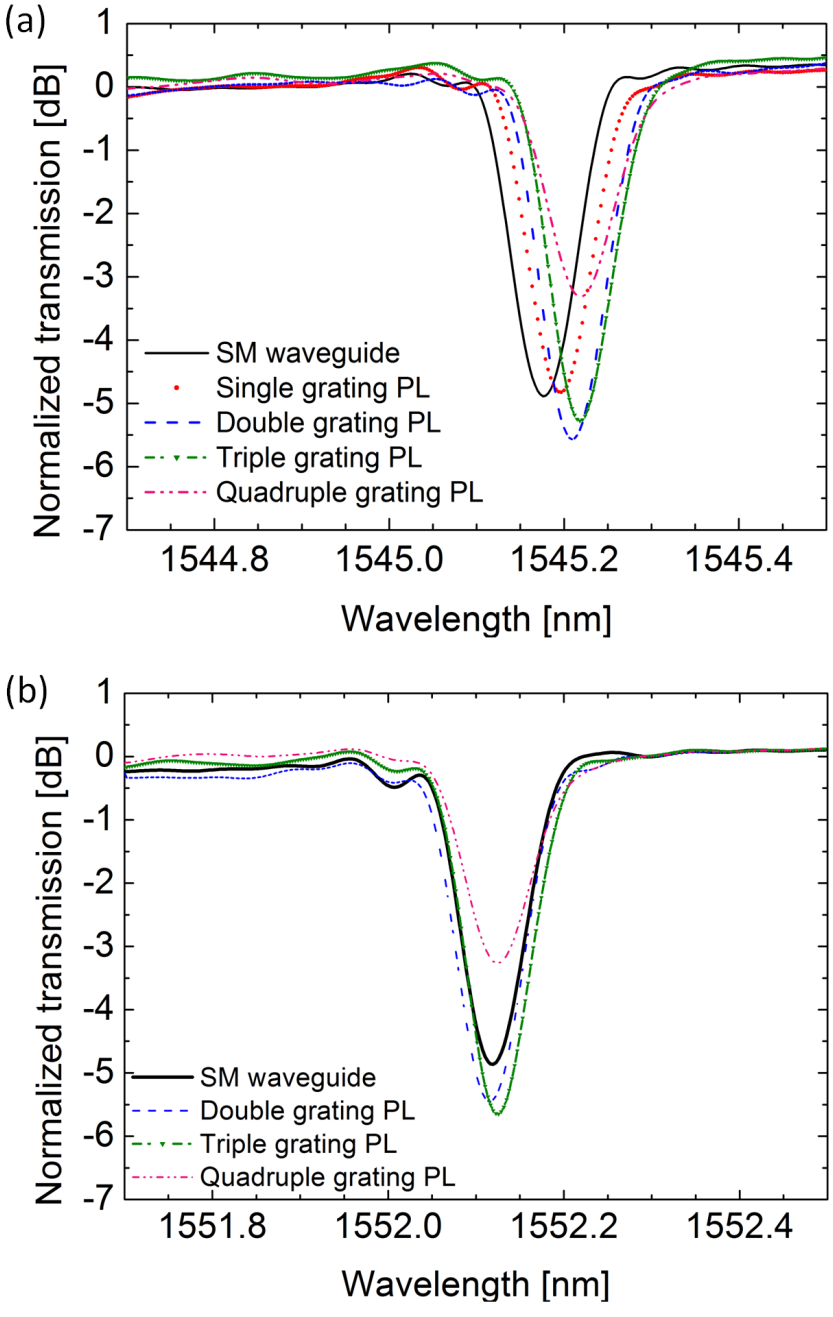

Figure 6.6: Normalised transmission spectra of the photonic lanterns (PL) and SM waveguides at (a) 1545 nm, (b) 1552 nm.

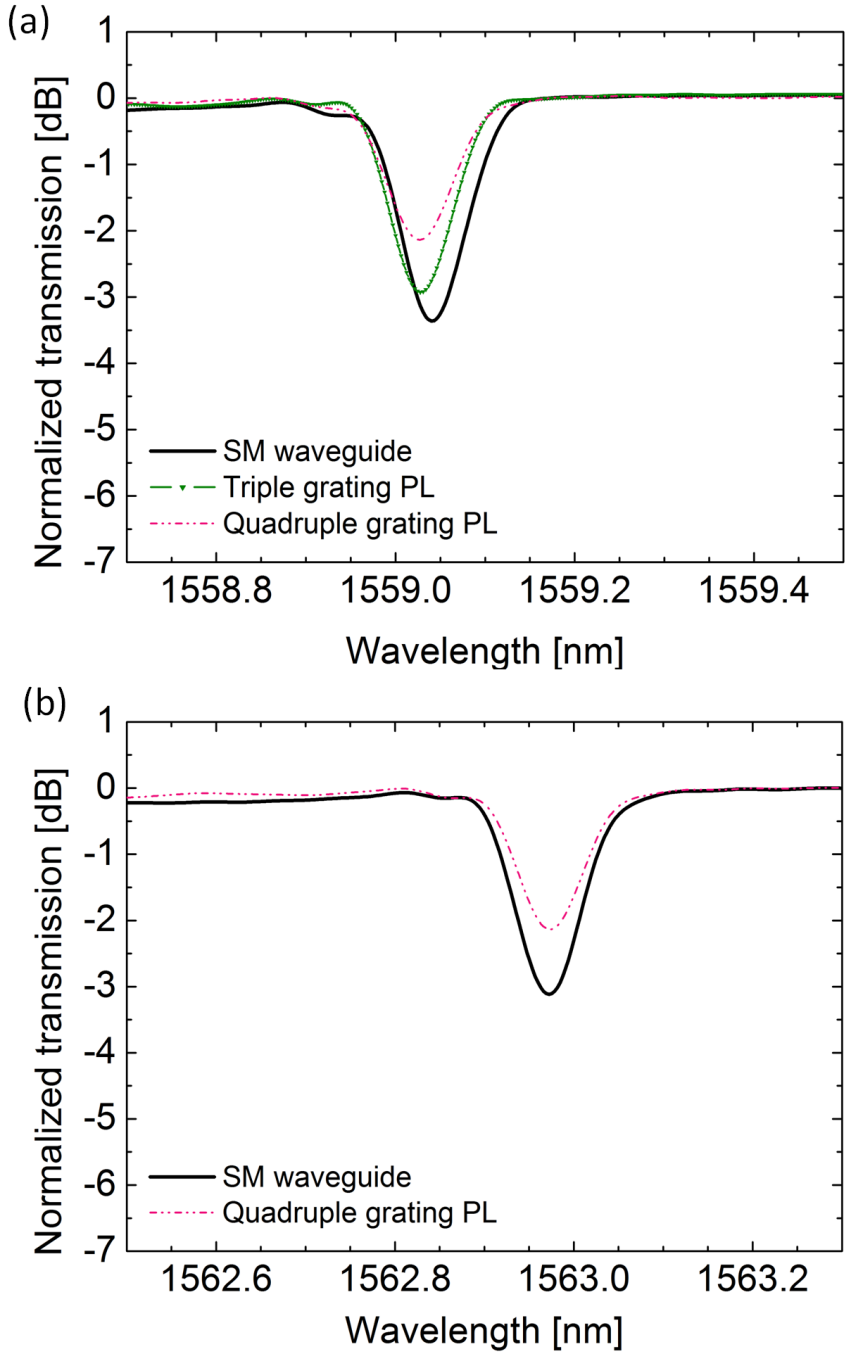

Figure 6.7: Normalised transmission spectra of the photonic lanterns (PL) and SM waveguides at (a) 1559 nm, and (b) 1563 nm.

Table 6.1: Summary of the depths of the gratings' transmission dips in the photonic lanterns (PL) and SM waveguide (SM WG).

Structure type	**Dip depth [dB]**			
	Wavelength [nm]			
	1545	1552	1559	1563
Single grating (PL)	4.89			
Double grating (PL)	5.49	5.38		
Triple grating (PL)	5.12	5.60	2.87	
Quadruple grating (PL)	3.25	3.26	2.03	2.14
Single-mode waveguide (SM WG)	4.86	4.42	3.30	3.12

grating photonic lantern and reference triple grating SM waveguide. Transmission losses of $\approx 0.3-0.4$ dB/grating/cm are apparent on the short wavelength side of each resonance due to coupling into the continuum of radiation modes. These losses can be reduced by better matching the grating and waveguide spatial profiles or by applying the conventional phase mask technique using infrared femtosecond laser pulses [124].

The calculated coupling strength coefficients for the triple photonic lantern are $\kappa_{1545\text{nm}} = 1.15\,\text{cm}^{-1}$, $\kappa_{1552\text{nm}} = 1.21\,\text{cm}^{-1}$ and $\kappa_{1559\text{nm}} = 0.83\,\text{cm}^{-1}$. Therefore the grating of length 20 mm would be expected to deliver 15 dB strong notches at 1545 nm and 1552 nm and 9 dB at 1559 nm. The required strength for OH suppression is of the order of 20-30 dB, which can be obtained with a grating of about 35 mm. This can be achieved with longer glass samples. However, due to the relatively high absorption in the Eagle2000 glass such long devices would have high losses making them unsuitable for use in astronomy. As a solution, AF45 glass could be used instead, as it features much lower absorption coefficient (cf. Fig.2.9b, Section 2.2.4). A 70-mm-long photonic lantern without gratings due to the glass absorption would have a maximum transmission of 63% and 99% in Eagle2000 and AF45, respectively.

The main advantages of integrated photonic lanterns over photonic lanterns based on multi-core fibres, include the flat top surface of the glass chip, and the ability to planarise the section of single-mode cores so that the laser beam is subjected to the same refraction effects when fabricating each of the waveguides and gratings. Such geometry enables the use of any of the femtosecond waveguide Bragg grating inscription

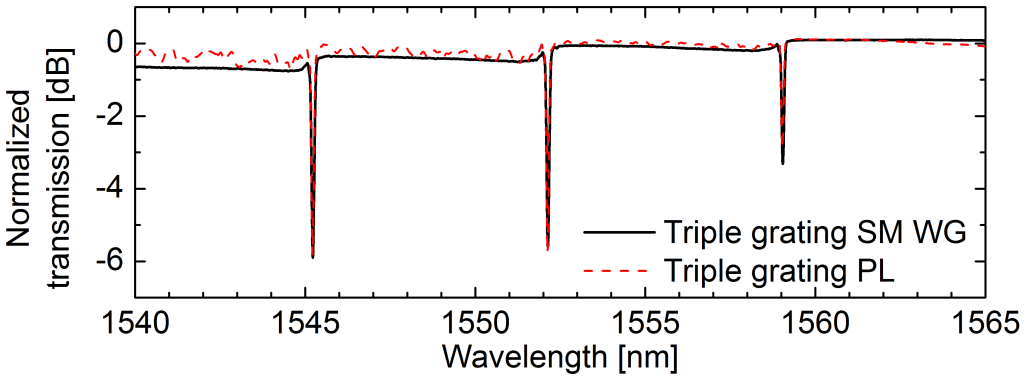

Figure 6.8: Normalised transmission spectra of the triple grating SM waveguide and triple grating photonic lantern. The transmission losses on the short wavelength side are caused by coupling into radiation modes.

methods. In order to achieve stronger gratings and reduce losses due to the coupling into the continuum of radiation losses, instead of using the micro-void point-by-point technique we suggest the use of either the core-scanning method (Fig.6.9a) [125] or the phase mask technique using IR femtosecond laser pulses (Fig. 6.9b) [126, 124], which are commonly used in the fibre Bragg gratings fabrication and can be also applied for the waveguide Bragg grating inscription.

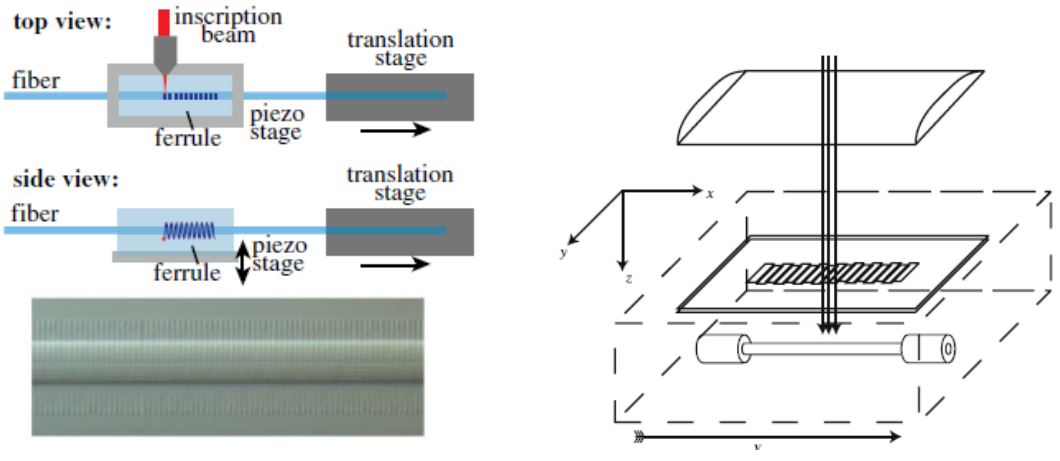

(a) (b)

Figure 6.9: (a) Illustration of the core-scanning FBG-inscription technique and a micrograph of the core-scanned FBG in SMF-28e fibre [125]. (b) Illustration of the phase mask technique using IR femtosecond laser pulses [126].

To suppress all coupling to cladding modes, it is vital to provide a homogenous grating cross section that covers the core and its surrounding [127]. The core-scanning technique is similar to the point-by-point technique with the difference that the glass ferrule is placed on a piezo stage driven by a sine wave, resulting in a sinusoidal inscription across the core (Fig. 6.9a). The amplitude of the sine wave is significantly greater than the core diameter, creating almost parallel lines of the period index modification. Because of the large overlap between the core and the modification, the technique produces strong gratings of low (0.1 dB) scattering to the continuum of radiation modes. In the phase mask technique the femtosecond laser pulses are focused through a cylindrical lens onto a phase mask placed between the fibre and lens. The periodic intensity variation pattern along the fibre causes the periodical change of the refractive index in both core and cladding. The loss due to scattering to the continuum of radiation modes can be as low as < 0.1 dB [128]. Multi-wavelength waveguide Bragg gratings can be produced using the above techniques by placing the grating structures one after another [121, 129].

One obvious vision for the structures presented here is future development of long, complex gratings used to filter out all the OH lines before the signal is injected into an astronomical spectrograph (as it done in GNOSIS instrument [46]). An alternative vision is to use devices similar to the ones presented here to perform spectral filtering of only a few OH lines after the light is dispersed in a low spectral resolution multi-object or integral field unit spectrograph. The high speed of the direct-write method (more than 20 mm/s in this paper) means that it is possible that after a spectrum is dispersed, a very large number of structures, such as that shown in Fig. 6.4, could be place on top of each other (or rotated 90 degrees about the injection axis and placed side by side). This would essentially mean that a separate photonic lantern device is tailored for every spectral resolution element of each object observed. For this application, complex gratings *are not required*, with only a few strong lines in the $\sim$1 nm spectral bandwidth represented by each pixel. This also has a great advantage over direct geometric OH suppression (e.g. an image-plane mask) because the spectrograph itself is only low-resolution – the high dispersion part of the instrument would be fully contained in the

integrated optics fibre Bragg gratings. The simplified idea of the device is presented in Fig. 6.10.

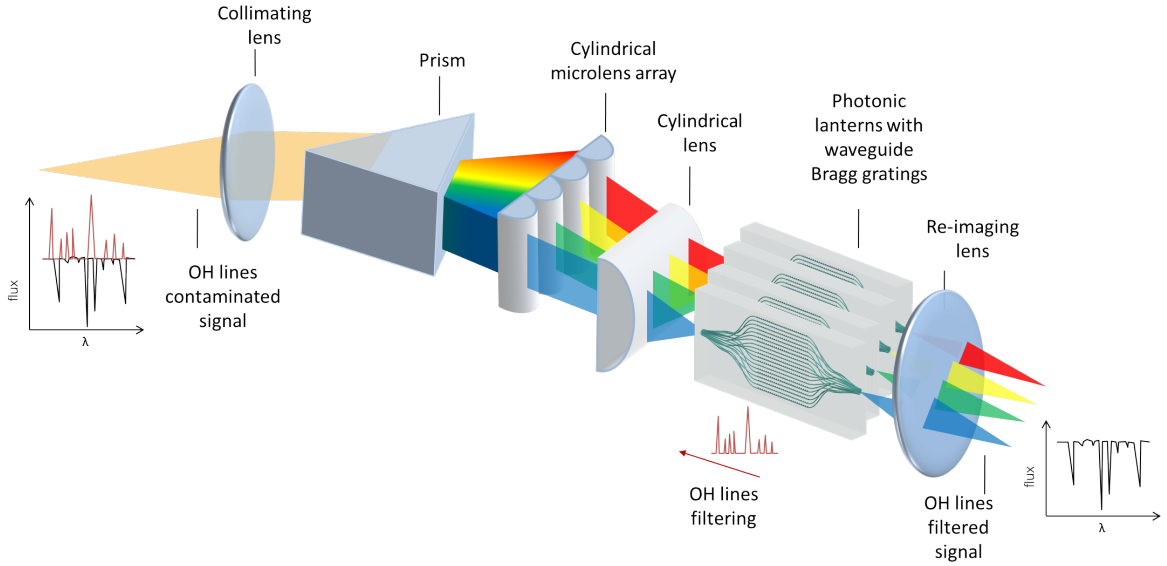

Figure 6.10: Schematic of the device utilising multiple integrated photonic lanterns with waveguide Bragg gratings for a single object. The light is pre-dispersed before injecting to the photonic lanterns, so that each of the photonic lanterns has to suppress only a few OH lines.

6.5 Conclusions

An integrated back-to-back photonic lantern structure with multiple integrated spectral filters has been demonstrated. The spectra characteristics of the WBGs match those of existing astrophotonics devices. By planarising the array of single-mode waveguides, the laser illumination conditions remain the same for each waveguide and grating, enabling the creation of multiple WGS of identical spectral characteristics. However, higher device transmission, lower scattering losses and stronger gratings could be achieved in a device inscribed in AF45 glass and fabrication of the gratings by the core scanning method or the phase mask technique using IR femtosecond laser pulses. Such devices will be inherently robust and offer flexibility with regard to the number

of the waveguides and their arrangement. Ultrafast laser inscription enables the miniaturisation of existing astrophotonic components by a few orders of magnitude as well as realising integrated add/drop filters in multiple-input multiple-output systems.

7

High-resolution spectra with slit reformatting devices

As introduced in Section 5.4, a slit reformatting device transforms the multimode input into a slit – an array of single-mode waveguides. Such a slit can be used as the input to a spectrograph, where each of the single-mode waveguides produces a spectrum once dispersed. When the single-mode waveguides are put close to each other, e.g. 13 µm apart, it creates a PSF in the form of a continuous slit, which is single-mode in the dispersion direction. The fibre photonic lantern cannot create such a compact slit, due to the large cladding (127 µm) surrounding each single-mode fibre. The integrated slit reformatting device does not require such high cross-dispersion as the fibre devices. In order to demonstrate this idea, we designed and set up a system

consisting of an integrated 1×7 slit reformatting device and a high-resolution DIR-RHEA (Diffraction-limited IR Replicable High-resolution spectrograph for Exoplanets and Asteroseismology) spectrograph.

This chapter firstly discusses the telescope which was available for the test, then the performance of the 1×7 slit reformatting device and the design and performance of the DIR-RHEA spectrograph. We discuss and propose a solution for the modal noise which appeared in the high-resolution spectra. Finally, we present the results obtained by injecting sunlight and starlight (Antares) into the slit reformatting device.

7.1 System description

The system used for stellar observations consists of the following parts: (i) telescope with a fibre feed, (ii) slit reformatting device, and (iii) spectrograph. The following sections describe each of these subsystems.

7.1.1 Telescope and fibre feed

The slit reformatting device was designed to be used on the 16" (406.4 mm) LX200 Meade Telescope at the Macquarie University Observatory, which is situated at the Macquarie University North Ryde campus located in the northern part of Sydney. The back of the telescope is equipped with a fibre feed unit (Fig. 7.1), which enables starlight injection into the fibre. The fibre feed has two fibre ports: one to link the telescope focus with the spectrograph, and the second to deliver the calibration spectrum to the fibre feed. Part of the fibre feed is a focal reducer which reduces the telescope focal ratio F/10 down to F/5 to reduce the size of the focal spot so that it is smaller than the multimode fibre, as well as reduce the size of the fibre feed so that it is feasible to be attached at the back of the telescope. The telescope operates in the seeing-limited regime with the typical seeing for the site ~ 2.5 arcsec. This value corresponds to a 49 µm focal spot diameter at $F/10$ and 25 µm at $F/5$. The latter allows for most effective capture of the light by the 35 µm core diameter fibre available for the experiment.

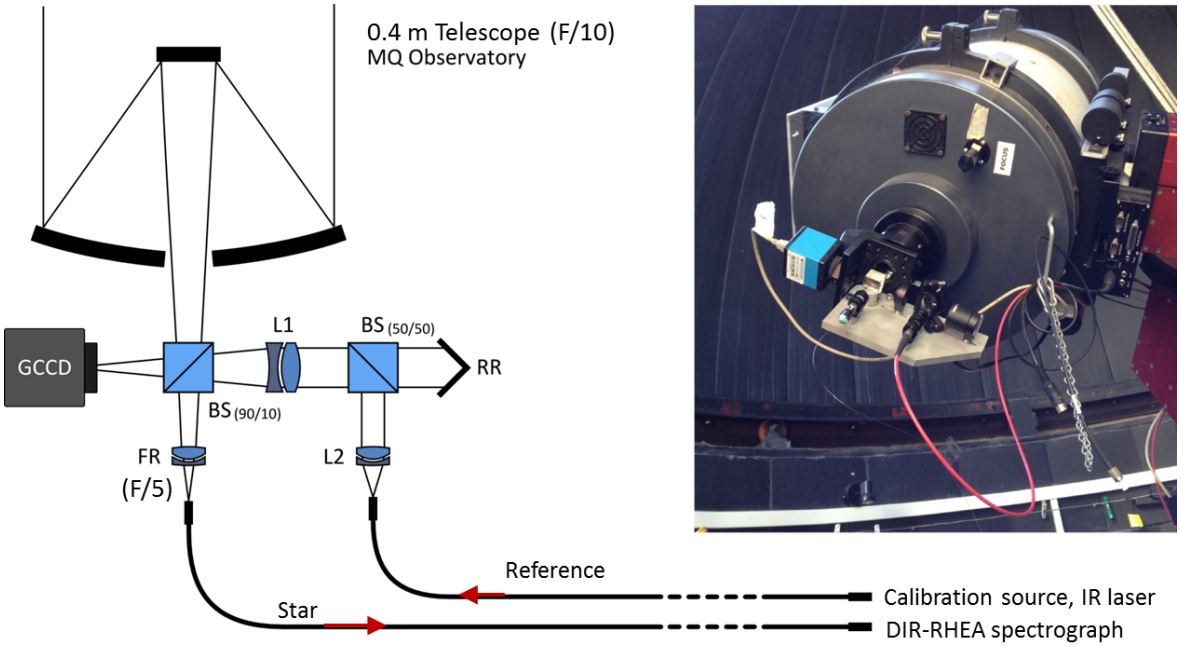

Figure 7.1: Schematic and picture of the fibre feed mounted on the telescope [130].

Fig. 7.1 shows the schematic diagram of the fibre feed [130]. The light coming from the telescope is split by a 10/90 beam splitting cube. 90% of the light goes straight through to the spectrograph fibre. The remaining 10% of the starlight is reflected to the side to the GCCD ImagingSource detector to monitor and adjust the telescope focus. The position of the fibre linking the spectrograph can be adjusted when the fibre is back illuminated. The beam is then split by the cube, collimated by a 100 mm lens and reflected back by a corner cube to be focused onto the ImagingSource detector. The calibration spectral lines are delivered by the fibre connected to the second fibre port. The light passes two lenses which change the focal ratio to $F/10$, then it hits the 50/50 splitter, passes the collimator and the beam splitting cube sends the light into the spectrograph fibre. These optics are all optimised for visible light; we chose not to insert in IR optimised optics because of the demonstrator status of this experiment.

7.1.2 1×7 slit reformatting device

The slit reformatting device was designed to match the standard number of modes produced at the focus of the telescope. Using Eq. 1.20 the number of modes N_m is 6 at wavelength of 1550 nm and seeing of 2.5 arcsec and 8 for seeing of 3.0 arcsec. Therefore the slit reformatting is composed of 7 single-mode waveguides, and forms $\sim$30 µm multimode input (Fig. 7.2). The waveguides at the output of the device are separated by 13 µm (as this was found to give the best results for 1×19 slit reformatting device in Section 5.4.1) and form a 88 µm-long slit. The length of each of the two transition sections is 10 mm.

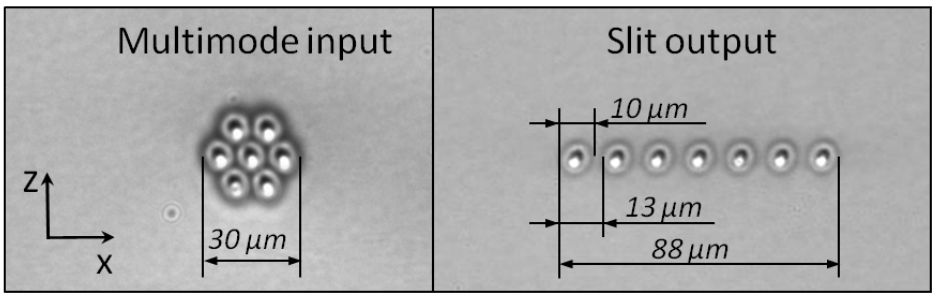

Figure 7.2: Cross-sectional micrograph of multimode input and slit output of the 1×7 slit reformatting device. The multimode input waveguide is composed of 7 single-mode waveguides separated by 10 µm, whereas the single-mode waveguides in the slit output are separated by 13 µm. The angle in each individual refractive index modification originates from the off-centre position of laser beam in the objective aperture during the fabrication process.

The waveguides were written with a pulse energy of 40 nJ at a translation velocity of 750 mm/min in order to create $\sim$10 µm diameter waveguides which were single-mode at 1550 nm. The laser was focused into a 30-mm-long alkaline earth boro-aluminosilicate (Corning Eagle2000) glass sample using a 100× oil immersion objective lens Zeiss N-Achroplan, NA = 1.25, working distance = 450 µm.

The device was pigtailed to a 35 µm diameter, NA = 0.22 multimode fibre (CeramOptec Industries, Inc.) using a fibre ferrule and optical adhesive as shown in Fig. 7.3. The throughput of the device was measured after pigtailing as described in section 4.3.3. Figure 7.4 shows the throughput as a function of $F/\#$ injection. The

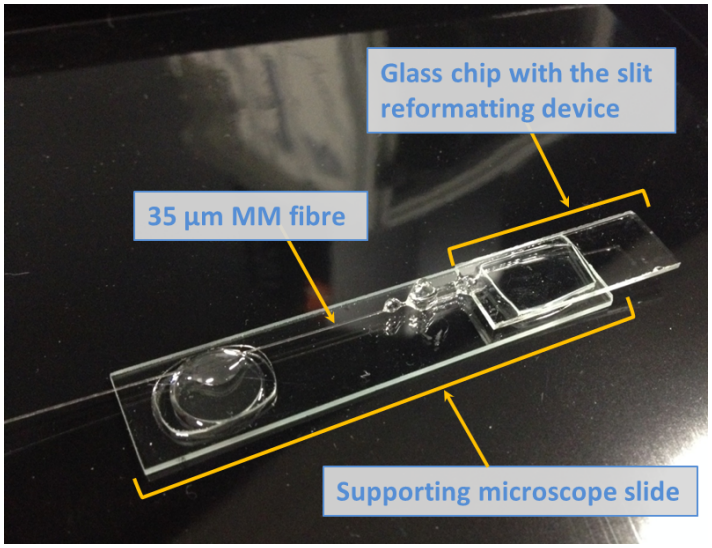

Figure 7.3: 1×7 slit reformatting device pigtailed to an optical fibre. The microscope slide is used to support and protect the sample.

normalised throughput of the slit reformatting device was measured to be 40%-70% (including glass absorption). However, when using a glass of lower absorption, we could achieve 50%-80% throughput. The number of modes in a MM fibre increases for increasing (faster) $F/\#$, therefore the throughput increases for increasing $F/\#$ since $F/\#$ represents a lower number of modes. The maximum of 80% throughput (taking into account the glass absorption losses) is not reached because the diameter of the multimode waveguide (30 µm) is smaller than the diameter of the multimode fibre (35 µm). When injecting a F/5 beam into the multimode fibre and slit reformatting device, we expect a transmission of 40% (Fig. 7.4).

7.1.3 Spectrograph design

DIR-RHEA spectrograph is a high spectral resolution instrument with R∼21,000 which operates over a wavelength range of 1400 - 1700 nm (the upper limit comes from the sensitivity cutoff of the detector). The design is based on the MIKE [131] and RHEA spectrographs [27, 130], which share the main feature of a double pass through the prism and collimator/camera, allowing reduction of both the footprint of the instrument and the number of optical elements. The use of reflective optics, such as off-axis parabolic

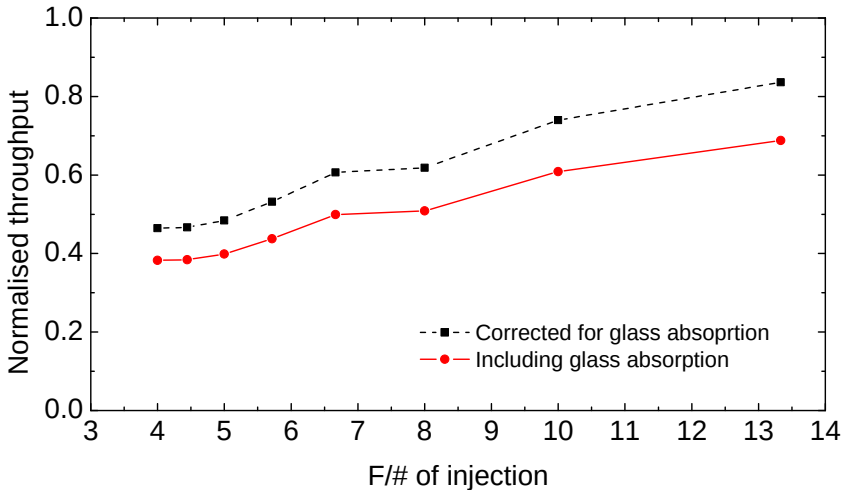

Figure 7.4: Normalised throughput of the 1×7 slit reformatting. Red line: values not corrected for glass absorption; black line: values corrected for glass absorption.

mirrors, in a double-pass spectrograph complicates the optical design and increases the cost. Therefore all the components apart from the échelle grating are refractive. All the optical components are off-the-shelf items from Thorlabs.

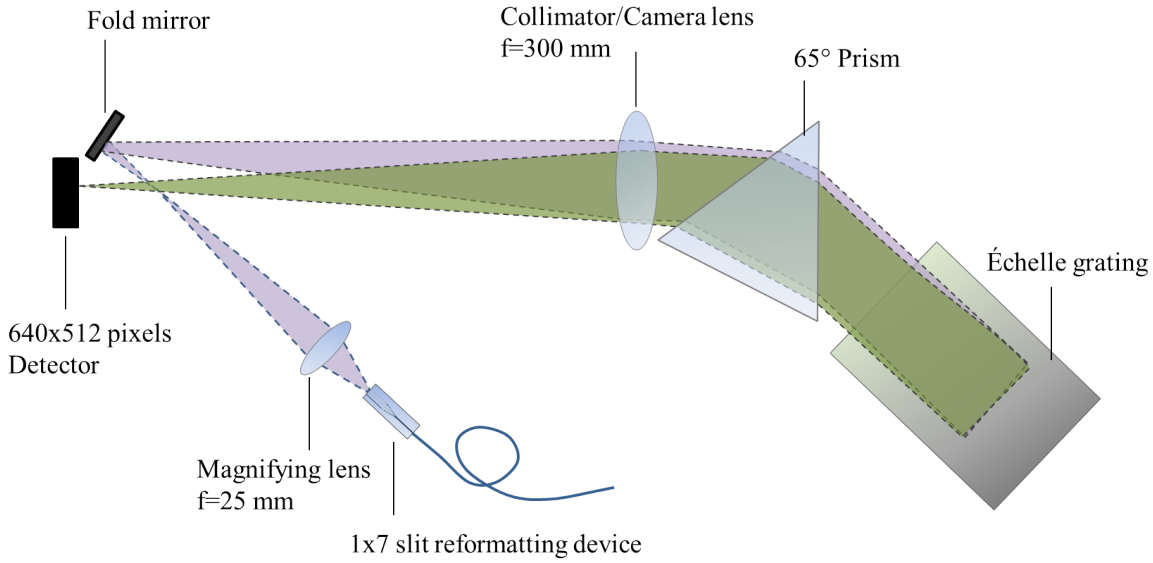

Figure 7.5: Optical layout of the DIR-RHEA spectrograph.

Figure 7.5 shows the optical layout of the spectrograph. The output of the single-mode waveguides in the slit reformatting device is at $F/8$ and 10 µm in diameter in

the single mode direction and it has to be magnified to provide sufficient sampling on the detector (Xenics Xeva-1.7-640) which has a 20 µm pixel size. A 25 mm focal length lens is used to give a factor of 3 magnification, which results in 1.5 pixel sampling and enlarges the focal ratio to $F/24$. The slit reformatting device and lens are positioned such that the beam would focus on the detector but instead it hits the fold mirror which directs it to the 300 mm collimator achromatic lens (Thorlabs AC508-300-A). The light is then slightly dispersed by a N-SF11 Equilateral Dispersive Prism (Thorlabs PS855) before hitting the échelle grating 31.6 Grooves/mm, 63° Blaze (Thorlabs GE2550-0363). The beam goes back through the prism which separates the orders, and again through the 300 mm lens which acts now as a camera and focuses the beam onto the detector. Figure 7.6 shows the DIR-RHEA spectrograph setup.

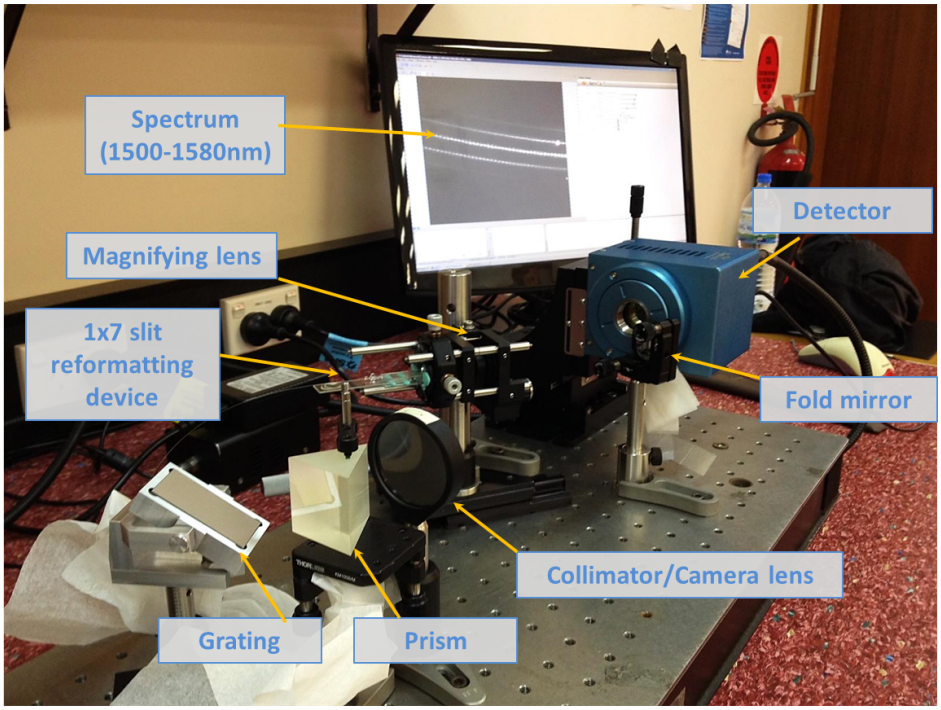

Figure 7.6: A photograph of the DIR-RHEA spectrograph and the produced spectrum in a 1500 - 1580 nm range.

The detector size (640×512) is not large enough to cover the entire spectral range produced by the spectrograph. For this reason the camera was rotated by 90°, so that the longer dimension is along the spectrograph dispersion direction and placed

on a translation stage to move it to three vertical positions to capture the whole spectrum (see Fig. 7.7). As a result the used detector area was about (3×640)×520 pixels. In order to be able to stitch the spectra together in the data post-processing, the calibration lines at the edges of two adjacent frames were taken. An external cavity tunable semiconductor laser TSL-210 (Santec Photonics Laboratories) was used as a calibration source. The laser operates within a wavelength range of 1500 - 1580 nm, with 0.01 nm resolution and 0.1 nm accuracy. The tunability of the laser gave us a high flexibility in the number of lines in the calibration spectrum. The laser source did not cover the entire spectral range of the spectrograph (1500 - 1580 nm out of 1400 - 1700 nm) but provided a sufficient number of lines to translate the raw image into a pixel-wavelength map using the Wavelength Scale Model (WSM) [27] and extract of the wavelength-intensity information (see Section 7.3.1).

7.2 Laboratory characterisation

The spectrograph and slit reformatting device were characterised to determine their performance. The first part of this section presents the results of the measurements of the spectral resolving power and spectrograph transmission, followed by the transmission estimation of the entire system on telescope. In the second part, we undertook detailed assessment of the coupling between the multimode fibre and the slit reformatting device.

7.2.1 Spectrograph resolving power

The spectral resolution of the spectrograph is computed by fitting a Gaussian function to the recorded laser line. Figure 7.8 shows a profile of the 1550.00 nm line. The horizontal axis in Fig. 7.8a shows the single-mode direction, whereas the vertical axis represents the multimode direction. Fig. 7.8b shows the normalised intensity profile in the single-mode direction of the line and fitted Gaussian function. The FWHM of the line is 2.26 pixels, which corresponds to 0.075 nm per resolution element. This value

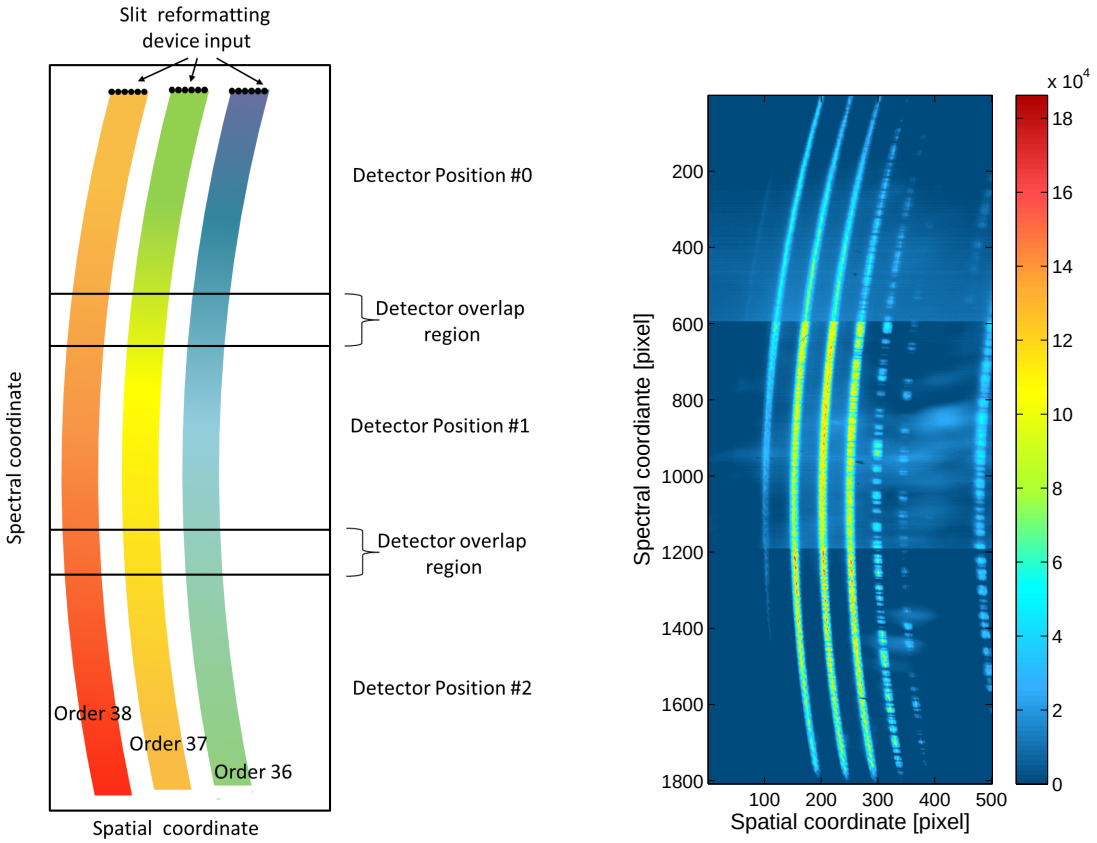

(a) (b)

Figure 7.7: (a) Illustration of the detector positions to capture the whole free spectral range. The overlap region between the detector positions permits data stitching for the full spectrum. (b) Raw data of the solar spectrum after stitching. The orders in the middle of the image represent the astronomical H-band (1650 ±180 nm), showing significant atmospheric absorption at the short wavelength range (right hand side). The order on the right hand side belongs to the J-band (1250 ±150 nm).

corresponds to $R \sim 21{,}000$ at 1550.00 nm. The maximum spectral resolution of the system, which was calculated as the maximum resolution of the grating illuminated with a non-truncated Gaussian beam, is $R \sim 35{,}000$ [132]. However the maximum resolution with a sampling of 2 pixels per resolution element is $R \sim 26{,}000$. The discrepancy between the achieved and ideal spectral resolution comes from the collimator/camera lens, which was not optimised for the IR wavelength regime. The details of the spectrograph parameters are given in Tab. 7.1.

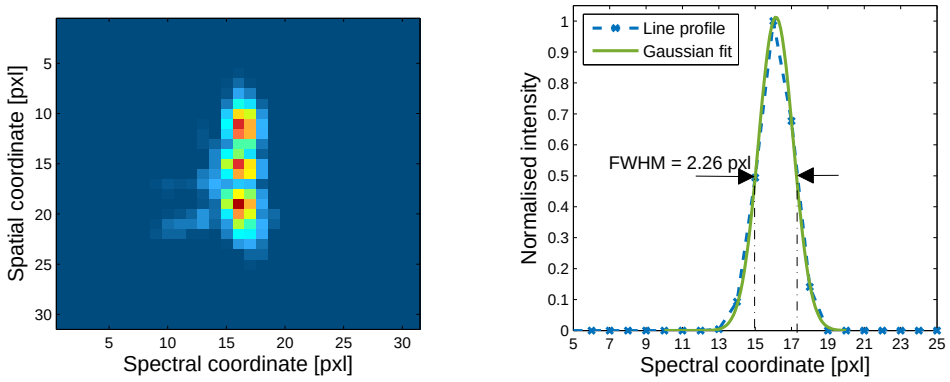

(a) (b)

Figure 7.8: (a) Point spread function at 1550.00 nm of the DIR-RHEA spectrograph fed with the 1×7 slit reformatting device and (b) the profile along pixel 15 in the horizontal direction showing the FWHM of 2.26 pixels.

7.2.2 System transmission

Based on the optical properties of the spectrograph components, the throughput of the optics in the DIR-RHEA spectrograph was estimated to be maximum of 10%. (see Tab. 7.2 for details). The TSL-210 (Santec Photonics Laboratories) laser tuned to 1550.00 nm and the spectrograph detector were used to measure the throughput of the spectrograph. Because the launching conditions of the laser beam into the multimode fibre highly influence the throughput of the slit reformatting device (as shown in Fig. 7.4), the slit reformatting device was replaced with a single-mode fibre (Thorlabs SMF28). The throughput was measured by comparing total counts from the single-mode fibre in two images: (i) the image of the 1550.00 nm beam going through the whole spectrograph and (ii) the image of the injecting beam obtained by placing the detector in the focus of the single-mode fibre with the magnifying lens. The throughput was measured to be $(7 \pm 1)\%$, which is slightly smaller than the estimated 10%. Source of additional losses is the non-perfect alignment of the spectrograph. The total efficiency of the system, including the telescope, fibre feed and detector QE is expected to be $\sim 1\%$ (see Tab. 7.2).

Table 7.1: Summary of DIR-RHEA spectrograph parameters and equipment used.

Parameter	**Value**
Central wavelength	1550 nm
Free Spectral Range (per order)	60 nm
Wavelength range	1400 - 1700 nm
Number of orders	9
Resolving power	21 000
Pixel sampling (per FWHM)	2.26 pixels (at 1550 nm)
Pixel sampling	0.075 nm per resolution element (at 1550 nm)
Camera / Collimator	Achromatic Doublet, f=300 mm
Cross-disperser	N-SF11 Equilateral Dispersive Prism, double pass
Échelle grating	31.6 Grooves/mm, 63° Blaze
Detector Xenics Xeva-1.7-640	InGaAs, 640×512, 20 µm pixels, 900-1700 nm sensitivity, QE $\sim$ 80% at 1550 nm
Instrument efficiency	$(7 \pm 1)\%$
Wavelength Calibration Source	Tunable laser, TSL-210 (Santec Photonic Laboratories), 1500-1580 nm, max. resolution 0.01 nm, max. accuracy 0.1 nm, max. repeatability 0.05 nm.
Broadband Calibration Source	Tungsten Halogen light source LS-1-LL (Ocean Optics), 360-2000 nm

7.2.3 Multimode fibre/slit reformatting device coupling

The pigtailed devices consist of two systems allowing mode propagation: a multimode fibre, and a slit reformatting device or photonic lantern. The condition and properties of the beam launched into the multimode fibre as well as the fibre properties itself determine the distribution of the fibre output near field. The fibre output then becomes the launching field for the slit reformatting device. The characteristics of the launching beam into the slit reformatting device strongly influence the response of the device, e.g. in our throughput measurements (Section 4.3.2 and Section 4.3.3) we were injecting

Table 7.2: Estimated transmission of the system. All the components which are not optimised for the visible have a transmission of 0.9. The number of surfaces in the lens doublets was counted as 4.

Subsystem	**Unit**	**Unit transmission**	**Number of surfaces**	**Total transmission**
Telescope	Mirrors	0.96	2	0.92
Fibre feed	Lens, beamsplitter	0.9	8	0.43
Slit reformatting device	0.4 throughput	0.96	1	0.38
Spectrograph				
	Magnifying lens	0.96	2	0.92
	Collimator/ camera lens	0.9	2×4	0.43
	Prism	0.85	2×2	0.52
	Prism dead area	0.9	2	0.81
	Grating	0.6	1	0.60
Detector	QE $\sim 1500\,\mathrm{nm}$			0.80
Total				0.01 (1%)

light from a spatially incoherent source (and partially temporally incoherent source, LED) in order to excite all the modes. The response of the devices when injecting only one spatial mode was very different. It is beyond the scope of this thesis to exhaustively investigate the response to illumination with a diffraction-limited spot. Nevertheless, the multimode fibre can produce a speckle pattern at its output, which is called modal noise. The resulting speckle pattern changes the coupling between the fibre and the slit reformatting device and, as we will see in the next sections, it became visible in the highly dispersed signal.

In the following sections we will try to assess the modal noise issue in our system, after an overview of the reports on this issue by other groups. We will discuss the results in a qualitative fashion.

7.2.4 Modal noise in photonic lanterns

We noticed that when launching a broadband source into the multimode fibre, the spectrum can feature a speckle pattern across the dispersed signal. Similar patterns manifested as modal noise are observed in multimode fibres but since the photonic lanterns and slit reformatting devices perform the multimode-single-mode conversion, it was expected that the modal noise would not be observed after integrating all modes. Some of the previous studies on highly dispersed signals from fibre photonic lantern devices reported observing a similar pattern [37, 133, 7, 134], whereas other studies do not report on such oscillations [135, 29, 136]. The observation of a periodic pattern was ultimately attributed to the modal noise in the devices [37], and not the Fabry-Peŕot cavity effect as initially suspected [7, 133]. Because of the different propagation properties of the fibre photonic lantern and the integrated photonic lantern, the interference with the uncoupled light was also suspected as a reason for the pattern. This effect has been observed before in the Dragonfly instrument, which also incorporates a glass photonic chip [137, 138]. In that case the origin of the fringing was identified as interference of the coupled and uncoupled light from the input of the guides. When the geometry of the Dragonfly chip was changed to avoid the interference of the stray light, the effect was gone. However, the possibility of this effect in our chip has been excluded based on simple tests and more investigation on the modal noise was performed.

When the speckle pattern is unstable on a timescale between calibration and observation, it results in modal noise, which increases uncertainties in the astronomical measurements. The uncertainties are mostly defined by the signal-to-noise ratio (S/N) of the data. In the case of the multimode fibres, the speckle pattern introduces further noise and S/N relates to the signal fluctuation and the contrast (visibility) Vis of the speckles. The speckle contrast is defined as:

$$Vis = \frac{I_{\max} - I_{\min}}{I_{\max} + I_{\min}}, \tag{7.1}$$

where $I_{\max}$ and $I_{\min}$ are respectively the maximum and minimum intensity of the

speckles. S/N based on experimental data is usually calculated according to:

$$S/N = \frac{\bar{I}}{\sigma(I)}, \tag{7.2}$$

where $\bar{I}$ is the average signal intensity of a featureless source and σ is the standard deviation. Since the speckle contrast Vis is a measure of the coherence of the source, the resulting S/N highly depends on the coherence as well, and highly coherent sources produce high contrast speckles, hence low S/N. Both temporal and spatial coherence contribute to the final fringe contrast. In the following sections we will try to assess the contribution from both of these. For convenience the temporal coherence will be called spectral coherence.

7.2.4.1 Coherent regime

Daino et al. [139] showed that the maximum achievable signal to noise ratio in a multimode fibre depends purely on the number of transmitted modes, when considering a signal which is both spatially and spectrally (temporally) coherent. He proposed that S/N could be expressed as:

$$S/N_{\text{coh}} = \sqrt{2N_m} \tag{7.3}$$

where N_m is the number of modes supported by a fibre per polarisation direction (cf. Eq. 1.12 and Eq. 1.15). So the higher the number of modes in a fibre, the higher S/N is. When dealing with a system supporting only a few modes, the resulting maximum S/N is very low, e.g. $S/N(7) \approx 3.7$, $S/N(19) \approx 6.2$, and $S/N(65) \approx 11$.

Consider a single spatial and spectral mode (not necessarily a fibre eigenmode) launched into a multimode fibre. Due to mode coupling, the energy from one initial mode is transferred to other modes. Because each of the modes has a different propagation constant β, the modes travel at different velocities and become out of phase. When the modes exchange energy again, they will interfere with one another constructively or destructively, depending on their phase difference. The resulting speckle pattern will have a very high speckle contrast. The interference pattern will be strongly

wavelength-dependent and when such a pattern is then injected into a slit reformatting device the response and the output of the slit reformatting device will strongly depend on the wavelength as well. When the signal is dispersed by a high-resolution spectrograph, the periodic speckle variability will be observed across the wavelengths (typically $\sim$0.1-5 nm period). Temperature variation or flexing of the fibre changes the phase difference between the modes, therefore varying the speckle pattern. If there is no mode filtering in the system (e.g. no fibre truncation occurs), and no spatial filtering (e.g. by overfilling the optics in the spectrograph or by placing a slit at the fibre output), the total intensity of the signal should remain constant across wavelengths, when integrated in the spatial dimension. As a result, if the slit reformatting device has a smaller modal volume than the fibre, the integrated spectrum will not be stable and will exhibit fluctuation.

7.2.4.2 Incoherent regime

Reducing coherence of sources lowers the speckle contrast. This can be realised by injecting broadband light and using a low-resolution spectrograph to reduce the spectral coherence and by launching a spatially multimode signal – e.g. a seeing-limited signal – to reduce the spatial coherence. Most studies so far have reported only on the influence of the spectral coherence of the source [44] and stated that the modal noise cannot be avoided in a fibre-fed high-resolution spectrograph. However, the spatial coherence should also contribute, but the relative contribution of the spectral and spatial coherence has not yet been well described.

Let us imagine injecting into a fibre a beam which evenly illuminates the fibre core and excites all the modes (low spatial coherence) but is dispersed by a high resolution spectrograph (high spectral coherence). In principle, the coupling between the modes should produce an evenly illuminated pattern with very low speckle contrast at its output. In this case the fibre output presents spatially stable and evenly illuminated output. The coupling between the fibre and the slit reformatting device should depend only on the coupling constants between fibre and device, with different modes contributing as an incident sum. The wavelength dependence of the output is much lower

than in the high coherence case and a signal dispersed by a high resolution spectrograph will produce a low frequency variability across the wavelengths.

In this case the fibre output presents spatially stable and evenly illuminated output. The coupling between the fibre and the slit reformatting device should depend only on the coupling constants between the fibre and the device.

7.2.4.3 Fibre length dependence on the modal noise

Initial theories and measurements [43, 140] predicted a strong dependence of the fibre length on the speckle contrast, i.e. the modal noise decreases with the fibre length and ultimately vanishes for very long fibre lengths ($\geq 1\,\mathrm{km}$). This effect is due to mode coupling along the length of the fibre, which results in a gradual loss of coherence, so that the modes can no longer interfere with each other [140]. More recent studies in an astronomical context [44, 141] showed no significant dependence of the fibre length on the S/N of the data within a range of a few meters to a few decameters of fibre length. The speckle contrast dependence on the fibre length is thus non-conclusive.

7.2.5 Experimental results

The modal noise experiments were performed with a 1×19 slit reformatting device. The multimode waveguide, of 54 µm in diameter, was pigtailed to a 35 µm diameter, 0.22 NA multimode fibre. The waveguides were separated by 13 µm in the slit end, so when dispersed by DIR-RHEA spectrograph, they formed a thick strip about 38 pixels wide.

In order to verify the origin of the speckle pattern in the device, multiple tests were performed. All the experiments were done using the Ocean Optics Tungsten Halogen light source HL-2000 or the single-mode fibre coupled tunable laser TSL-210 operating at low power. Unless stated, all the images were recorded with fibre at rest and 5 s exposure and each dataset consists of 32 frames.

7.2.5.1 Pattern change depending on the injection conditions: incoherent and semi-coherent case

Sets of measurements were taken with two fibre lengths (2.6 m and 30 m) and at different injection conditions: (i) fibre straight in front of the source and in focus, (ii) fibre at an angle ($\sim 6^\circ$) to the source and in focus, and (iii) fibre straight in front of the source and out of focus. The data were acquired by coupling a LS-1-LL (Ocean Optics) broadband multimode source into the multimode fibre by means of a tightly focusing lens (f=5 mm).

Figure 7.9 shows sections of the acquired spectra for the three injection conditions and for a reference, in which the fibre was being agitated (smoothing out the spectrum). The different intensity in the vertical direction comes from different coupling and efficiency to the waveguides in the slit output. First of all, it is evident that the speckle pattern changes depending on injection conditions, giving the most uniform pattern for a straight injection in focus, and creating relatively periodic speckles once out of focus or at an angle, for both fibre lengths. We can interpret this effect as following: when the fibre face is placed in focus and straight, the fibre core is illuminated uniformly and the fibre modes are filled evenly by a high NA of the lens. Such a system operates close to the incoherent mode. Once the angle is changed, the illumination may not be uniform any more and lower NA will not fill all the modes. When the fibre is placed out of focus, the beam NA is smaller, so again it does not excite all the modes evenly. In this case the system operates closer to the coherent regime.

The second effect which can be noticed relates to the fibre length. When comparing the beam injection conditions and fibre lengths, we can see in Fig. 7.9 that the shorter fibre (2.6 m) is more prone to producing the speckle pattern if the fibre modes are not evenly filled. The fibre of 30 m length introduces only small deviation from the even illumination and at much lower degree. This suggests that the long fibre length can reduce the modal noise.

When comparing the results acquired with the best injection conditions (straight and in focus) with the results acquired when agitating the fibre, the spectra look almost the same. Whereas fibre length l=2.6 m presents slight evidence of speckles with greater

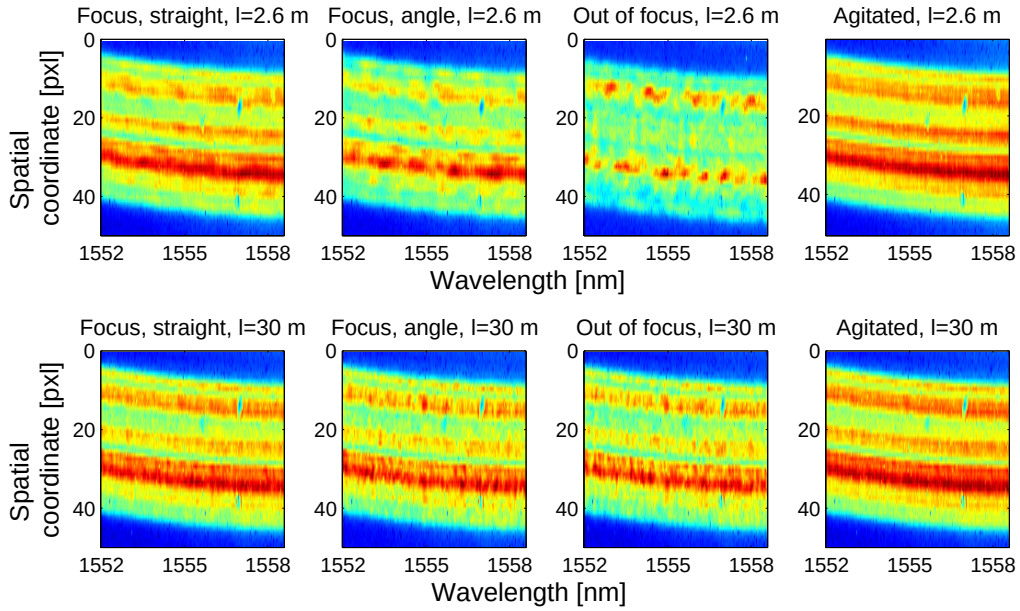

Figure 7.9: 50 pixels×200 pixels (6.7 nm) sections of the spectra obtained with DIR-RHEA spectrograph and the 1×19 slit reformatting device (vertical axis) when injecting a broadband multimode beam (white light source, LS-1-LL). The tests were done for two lengths of the multimode fibre: l=2.6 m and l=30 m and various injection conditions.

sensitivity to the alignment, the longer fibre produces a pattern almost as smooth as the agitated fibre.

7.2.5.2 Pattern change depending on the fibre length: semi-coherent case, short fibre range

The dependence of the multimode fibre length on the speckle pattern was also investigated in a short fibre length regime. The spectral images were recorded for fibre lengths of 2.6 m, 3.6 m, 5.0 m and 6.6 m. Figure 7.10 shows the recorded speckle patterns. For comparison we plotted the spectrum produced by an agitated fibre and a single-mode SMF28 fibre. All the measurements were done with the fibre being out of focus, with not all the modes in the multimode fibre excited, hence producing speckle patterns. A periodic fluctuation along the wavelength can be observed in the multimode fibre images. The periodicity of the pattern and the speckle contrast is affected by the fibre

length, however no drastic improvement can be observed in this length regime. A spectrum produced by the DIR-RHEA spectrograph fed with a SMF28 fibre is presented for a comparison to demonstrate that the periodic oscillation does not originate in the spectrograph system.

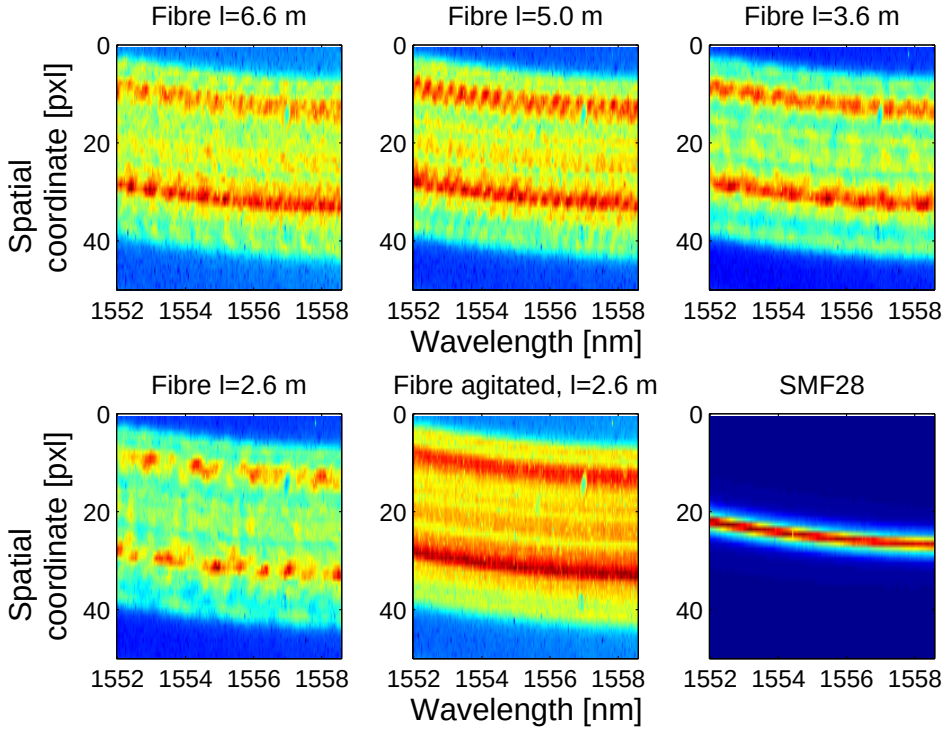

Figure 7.10: 50 pixels × 200 pixels (6.7 nm) sections of the spectra acquired with DIR-RHEA spectrograph and the 1×19 device or SMF28 fibre when injecting a broadband multimode beam (white light source, LS-1-LL) placed out of focus. The length of the multimode fibre varied between 2.6 m and 6.6 m. The spectra obtained with an agitated fibre and a SMF28 (without the slit reformatting device) are presented for comparison.

7.2.5.3 Pattern change depending on the fibre length: spatially coherent case

The output of the tunable laser TSL-210 operating at low power was coupled into a single-mode fibre, generating a single spatial mode, broadband source. The images were recorded at 8 s exposure time. Figure 7.11 shows the recorded speckle patterns

for one order and resulting spectra. The 2.6 m fibre produces a clear periodic structure 1.2 nm (0.6 nm peak-to-peak) period along the dispersion direction, which is manifested in the obtained spectrum (summed signal, bottom graph). The signal acquired with the 30 m fibre produces a random pattern, which we believe can vanish when using a very long fibre (> 100 m).

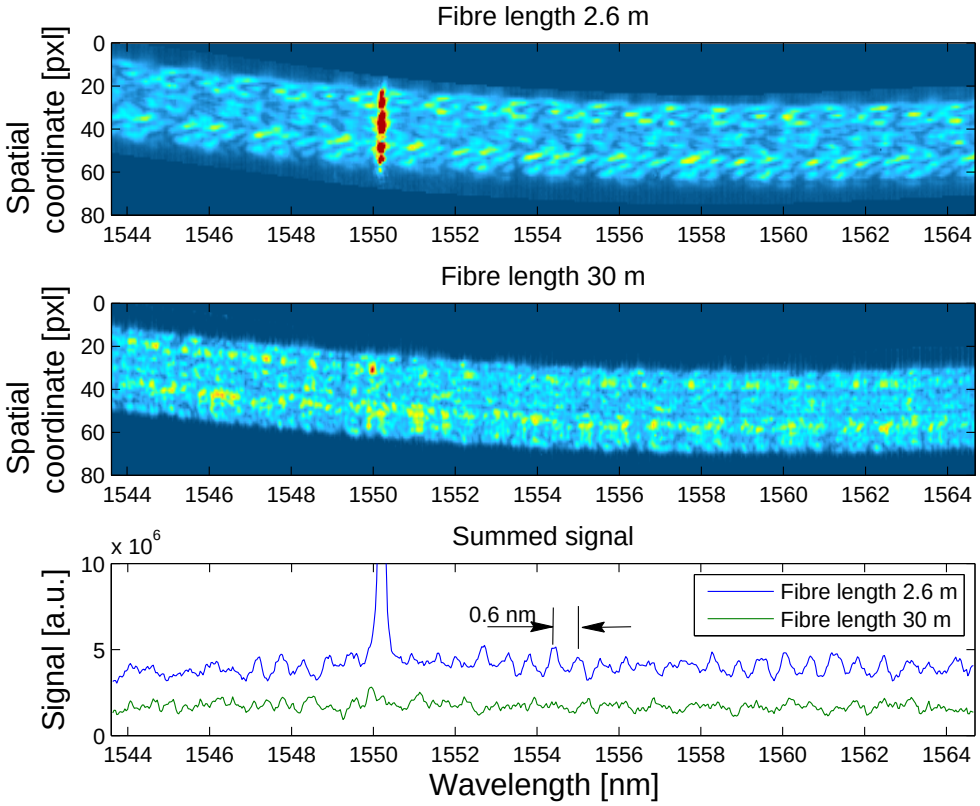

Figure 7.11: Spectra obtained with DIR-RHEA spectrograph and the 1×19 slit reformatting device for two lengths of the multimode fibre: 2.6 m and 30 m, when injecting a broadband single-mode signal. (Top and middle) recorded speckle patterns and (bottom) extracted spectrum. The 2.6 m fibre length spectrum features a 1550.2 nm line (here overexposed).

7.2.6 Modal noise – summary, conclusions and discussion

The conclusions based on the tests and analysis presented above can be summarised as follows:

1. A pigtailed device is not ideal.

   A system consisting of the integrated slit reformatting device pigtailed with a multimode fibre has a different response to a slit reformatting device alone. In order to create even illumination of the slit reformatting device input, the modes in the multimode fibre have to be filled evenly and originate from much larger modal volume than the photonic lantern. This is only possible with either an exact mode matching between the multimode and multimode waveguide in the photonic lantern or else large coupling loss between the multimode fibre and the photonic lantern. As a solution the light should be coupled directly from the telescope to the photonic lantern.

2. The injection into the device strongly affects the modal noise.

   Orientation and the spatial properties of the beam launched into the system (fibre and slit reformatting device) determine the system response. The key parameters relating to the injection are: (i) the degree of the overlap between the diameter of the injecting beam and the fibre face, (ii) the intensity profile, and (iii) the degree of the overlap between NA of the injecting beam and the fibre. By ensuring that all the modes are equally filled in the fibre, it is possible to avoid the modal noise. However for many cases the pigtailed devices are highly desirable and must be considered.

3. Fibre length affects the modal noise.

   A long fibre length reduces the modal noise. The required fibre length is proportional to the resolving power of the spectrograph, i.e. $\Delta n_{\text{eff}} \cdot l/\lambda \gg R$, where Δn_{eff} is a typical difference between fibre mode effective indices, l is the fibre length, λ is the wavelength and R is the spectrograph resolving power. In the experiment, a substantial reduction of the modal noise using 30 m fibre was observed and a very long fibre (> 100 m) should cause it to vanish completely. However, long fibres cause higher signal attenuation.

4. Modal noise is less significant in the seeing-limited regime.

Quickly varying speckles of the seeing spot create a perfect spatially incoherent source. Therefore we believe that when a device operates in the seeing-limited regime and/or the image exposure times are much longer than the atmosphere coherence time, the system will not introduce significant modal noise (as reported in [136]). A device incorporated into a telescope structure with an adaptive optics (AO) system will feature modal noise.

5. Fibre shakers are the easiest solution.

   When the device has to be pigtailed to deliver the light from an AO-equipped telescope, the easiest solution is to agitate the fibre during the exposure.

7.3 On-sky demonstration

We demonstrated the operation of the DIR-RHEA system with the slit reformatting device using sunlight and starlight from Antares. The following sections give details of the setup and a summary of the results, as well as an overview of several difficulties encountered.

7.3.1 Data acquisition and data processing

An equal number of `Sky` (solar or star) and `Dark` frames were taken during the observations, because the Xenics Xeva detector is characterised by a relatively high dark current which fluctuates over time. The data were reduced by subtracting `Dark` frames from each of the `Sky` frame. The `Dark` frames were taken at the same exposure time as the `Sky` frames but with blocked source light. The `FlatField` frames were taken by placing a white paper in front of the detector, to calibrate the pixel response. About 8 calibration laser lines per detector position were taken to perform the wavelength spectrum calibration. Calibration line information and the spectrograph geometric parameters were inserted into the Wavelength Scale Model (WSM) [27] to analytically create a map of pixel-wavelength relation. The wavelength-intensity information was

extracted by comparing the pixel-wavelength map with the pixel-intensity map (reduced image) and summing the intensities across the same wavelength. Such approach enables the extraction from curved spectra as presented here.

7.3.2 Solar observations

The first demonstration of the DIR-RHEA spectrograph was performed with sunlight. The spectrograph was fed with the pigtailed 1×7 slit reformatting device. The sunlight was directed by a heliostat down to the focusing lens with f=45 mm and the multimode fibre. For each detector position, a set of 32 frames, 5 s exposure time was taken. A mosaic of typical frames is presented in Fig. 7.7b. Figure 7.12 shows the resulting spectra. The data were not normalised for the grating efficiency, and therefore show higher intensities in the middle of the order than on the sides. Figure 7.12a shows the spectrum over 3 orders, covering a wavelength range of 1485-1633 nm. Different colours (red, blue and green) show different detector positions.

Even though there are not many features in the solar spectrum in the near-IR wavelength range, it is possible to see the atmospheric water absorption lines. Therefore, the atmospheric transmission spectra [142][1] were overlaid on top of the solar spectra. Figure 7.12b presents the spectrum in the 1570-1582 nm range, showing a good agreement between the lines recorded with DIR-RHEA spectrograph and the reference transmission lines. One of the origins of the noise in the spectrum is modal noise, which is visible in the form of speckles across the spectrum in Fig. 7.7b. This effect was discussed in details in Section 7.2.3.

7.3.3 Stellar observations

The object selection for the on-sky testing of the 1×7 slit reformatting device and DIR-RHEA spectrograph was dictated by the object brightness in the visible (astronomical V-band, 500-600 nm) and near-IR (astronomical H-band, 1500-1800 nm) wavelength range and the position in the sky at that time. The minimum brightness of 6-7 mag

[1]Gemini Observatory IR transmission spectra: http://www.gemini.edu/sciops/telescopes-and-sites/observing-condition-constraints/ir-transmission-spectra

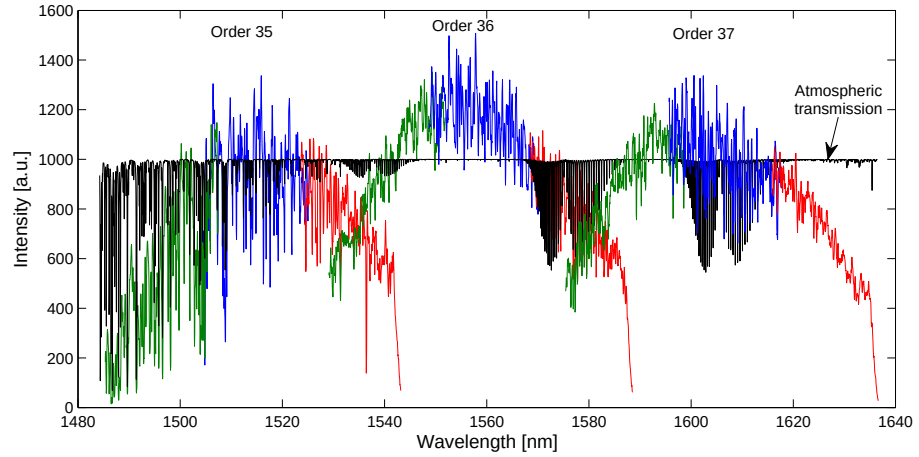

(a)

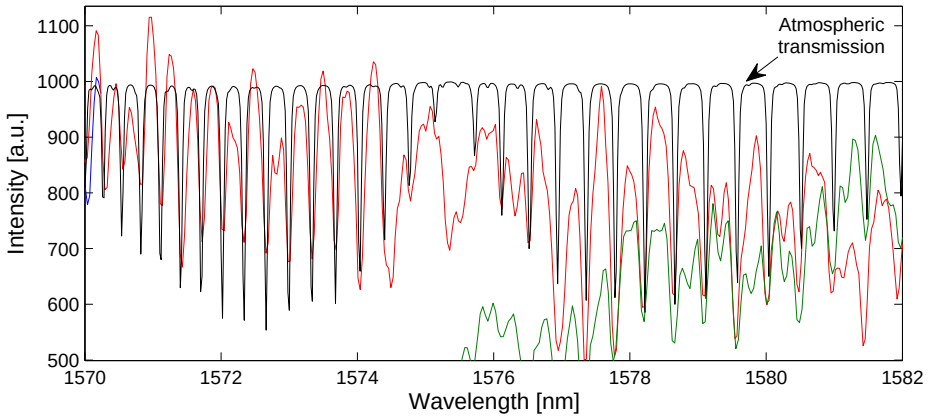

(b)

Figure 7.12: (a) Reduced solar spectra covering three spectral orders and the atmospheric transmission for a reference (airmass 2.0, water vapour column 1.6 mm) [142]. The three different colours are used to mark different detector positions. (b) Part of the spectrum showing water absorption lines.

in the V-band is required for the system to guide the telescope during the night. The minimum brightness of -2 mag in the H-band is required to detect the photoelectrons above the noise level on the detector. Based on these constraints, Antares and W Hya were the selected objects. Antares (α Sco) is a bright red supergiant star of brightness 0.91 mag in the V-band, and -3.49 mag in the H-band. W Hya is a Mira star, of brightness 7 mag in the V-band, and -2.46 mag in the H-band.

The data were collected in sets of 180×10 s or 60×30 s frames. Because of the high dark current level in the detector, the same number of `Dark` frames were taken. The

observations were conducted over a period of 11-29 May 2014, with seeing conditions that varied between 1.2 arcsec and 4 arcsec. Figure 7.13 shows one of the reduced images of Antares spectrum recorded on 22/23 of May 2014 featuring a relatively high signal-to-noise ratio S/N.

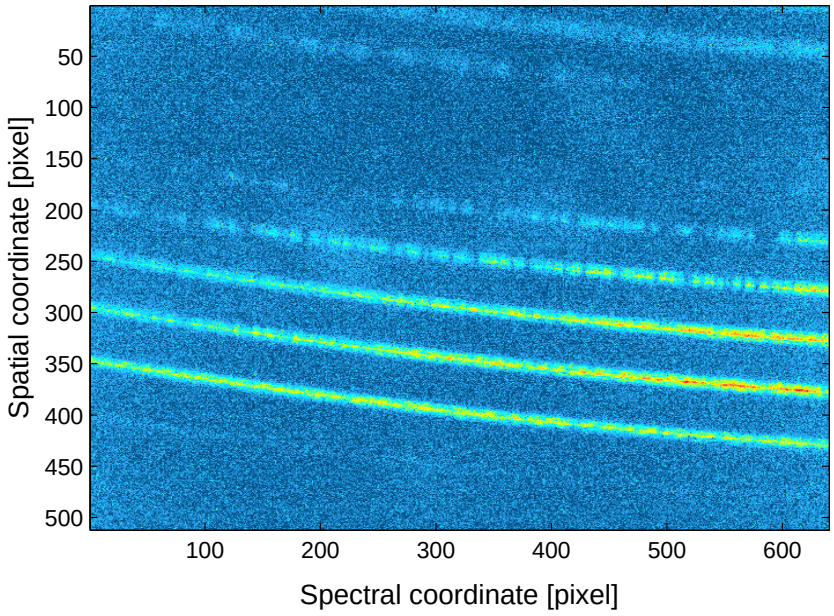

Figure 7.13: Spectral image of Antares recorded at detector position #0 with seeing 2 arcsec. Atmospheric absorption lines are visible in the orders towards the top of the image.

The spectrum for one spectral order resulting from Antares observations on three nights of 14/15, 22/23 and 28/29 of May 2014 is presented in Fig. 7.14. For a comparison we plotted also the result of the atmosphere model BT-Settl[2], which we performed for an Antares-like star of effective temperature $T_{\rm eff} = 3800\,{\rm K}$, $\log({\rm g}) = 0.0$, $[{\rm Fe/H}] = 0.0$, and convolved with an instrument spectral resolution of $R \sim 20,000$. Note that macro-turbulence or rotation (of Anatres or Earth) can introduce blurring of the spectrum. Antares, as a late-type supergiant M1.5Iab-b type star, is known to contain multiple absorption features in the IR part of the spectrum, resulting from the rotational-vibrational transitions of diatomic molecules. The strongest features in H-band are

[2]BT-Settl: `http://phoenix.ens-lyon.fr/Grids/FORMAT`

called band heads, which are created by carbon monoxide (^{12}CO) appearing as a sharp absorption line followed by lots of weak overlapping lines. Several of the CO band heads are marked with dotted lines in Fig. 7.14. Despite the fact that the observed spectrum is relatively noisy, the drops that are characteristic for the CO band heads are visible and closely coincide with the modelled features. The atmospheric absorption lines were also detected in Antares spectrum and are presented in Fig. 7.15.

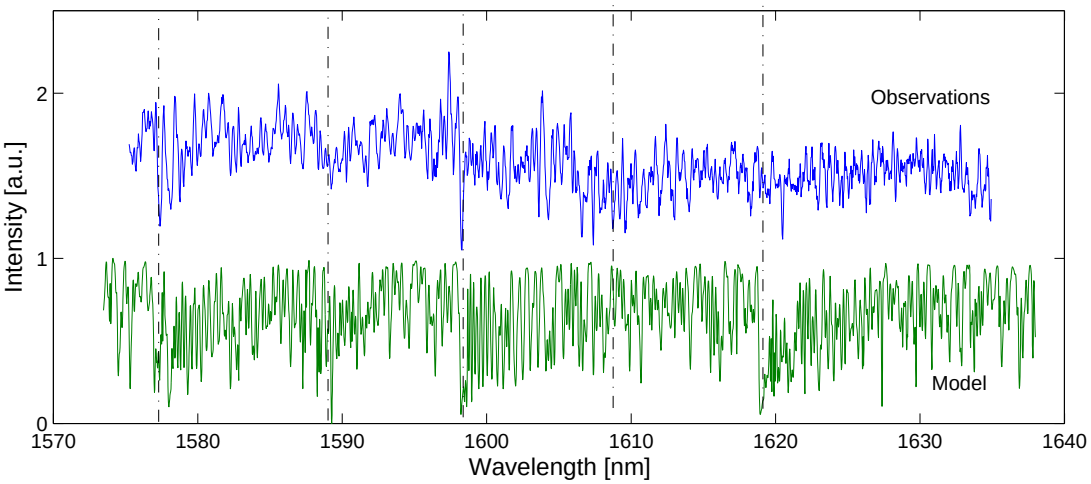

Figure 7.14: Comparison between the observed spectrum of Antares and the synthetic one computed for the model atmosphere ($T_{\rm eff} = 3800\,$K , log(g) = 0.0, [Fe/H]= 0.0). The dotted lines indicate the CO band heads.

W Hya is a more interesting object, with multiple emission and absorption lines in the H-band. However, its low brightness in the V-band made the telescope tracking very challenging, as 7 mag is at the bounds of the tracking camera sensitivity. W Hya is also 2.5 times fainter in the H-band than Antares and as a result all the data were at very low S/N and are not presented here.

7.4 Conclusions

A spectrograph of resolving power R=21,000 and covering a wavelength range of 1400-1700 nm was built to spectrally resolve signal from a 1×7 and 1×19 slit reformatting devices with 13 µm separation between the waveguides in the slit end.

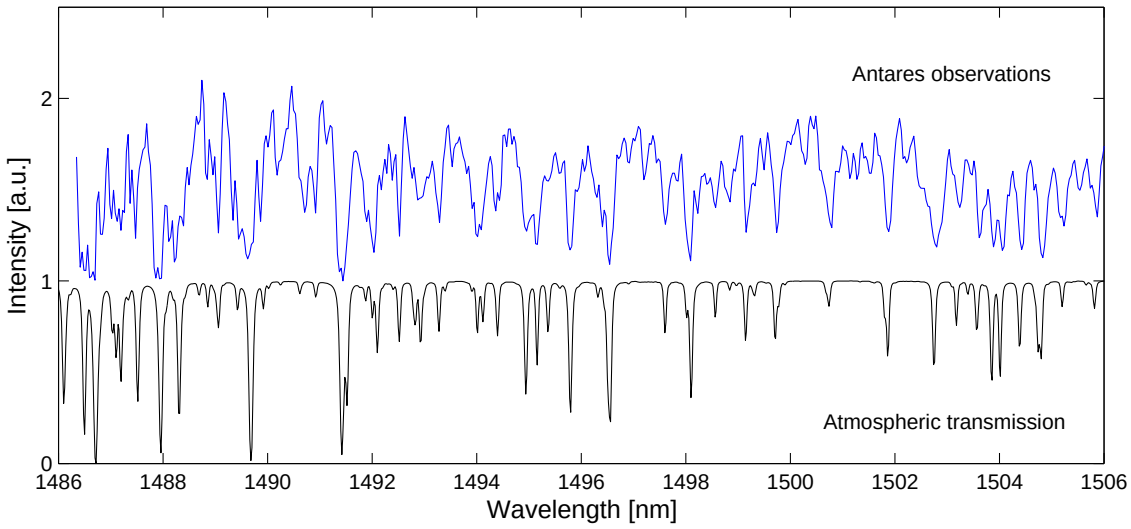

Figure 7.15: Comparison between the observed spectrum of Antares, featuring mostly the atmospheric absorption lines and the atmospheric transmission spectrum.

The modal noise was identified in the solar spectra. Further experiments showed that a device that is pigtailed to a multimode fibre features modal noise unless all the modes in the fibre are evenly excited. As a solution to this issue, the light should be directly injected into the glass chip or a fibre shaker has to be used.

The system was used to perform the on-sky demonstration using sunlight and starlight from Antares. The solar spectrum over 1480-1630 nm was collected, revealing accurately the water absorption lines. The system was also used to collect the spectra of Antares. By comparing the acquired spectrum with a modelled one, we were able to identify several CO features. However, the data would have less noise if we are able to increase S/N of the data. The main reasons for low S/N are the low throughput ($\sim 1\%$) of the system and high readout noise (~ 1000 e$^-$) of our detector. A number of system parameters and components can be changed to achieve higher S/N. First of all, the spectrograph alignment should be optimised and all components should be made of glass that is highly transparent in IR and coated with IR anti-reflection coating. By replacing the lenses, the transmission could be increased up to 25% for the spectrograph 85% for the fibre feed. The overall throughput would then be 5%. Secondly,

the current substrate for the slit reformatting device could be replaced by a glass of lower IR absorption, e.g. AF45 (Schott). Furthermore, the current detector could be replaced by another one of lower dark current and lower readout noise (~ 10 e$^-$), e.g. HAWAII-2 detector. Finally, a bigger telescope would collect more light and improve S/N. By using a telescope of double the diameter, we would achieve a 4 times better efficiency.

8

Conclusions and future work

In this project we explored and demonstrated integrated converters of multimode to single-mode light, called photonic lanterns and slit reformatting devices. This chapter presents the conclusions and a summary of the work completed in this project, together with a discussion of possible next steps for future research.

8.1 Conclusions

We undertook a detailed optimisation of three main building blocks of photonic lanterns and slit reformatting devices fabricated with the HPO femtosecond laser system. After finding the design for multimode waveguides [1], we analysed the mode evolution along a transition section between the multimode and isolated single-mode waveguide sections, and modelled three types and lengths of transition to find the adiabatic

regime. Then, we fabricated a range of devices to verify the modelling findings and optimised the separation between the waveguides in the multimode section, as well as the separation between single-mode waveguides in the slit end of the slit-reformatting devices. The simulation results showed that a cosine type of transition exhibits the lowest losses and the isolated waveguides need to be separated by $> 35\,\mu m$ to possesses minimal cross-coupling. The throughput measurements of the fabricated back-to-back devices showed that a transition of 4-5 mm length can result in an efficiency of 75% (62% total efficiency including glass absorption losses). The study of the efficiency of the back-to-back photonic lanterns showed the separation between the waveguides in the multimode section affects the number of modes supported by the device and highly influences the device loss. In our case a device of $\geq 13\,\mu m$ waveguide separation in the multimode part supports all the modes. Finally, we demonstrated that the slit length in a slit reformatting device can be minimised by placing the waveguides 13 µm apart, which allows for supporting all the modes. Such devices maintained the throughput of 95% for $F > 12$ injection excluding glass absorption losses (82% for $F/\#>12$ including glass absorption losses).

We created fully integrated photonic lanterns with multiple waveguide Bragg gratings. By planarising the single-mode middle section of the back-to-back photonic lanterns the femtosecond laser can access each of the waveguides and inscribe waveguide Bragg gratings of the same characteristics. Multiple gratings were placed in the waveguide using the point-by-point technique. Devices which filter out one, two, three or four wavelengths were fabricated. The best performance was demonstrated by the device with three gratings for wavelengths of 1545 nm, 1552 nm and 1559 nm, featuring grating depths of 5.12 dB, 5.60 dB, and 2.87 dB, respectively.

We used a 1×7 slit reformatting device and a single-mode high resolution DIRRHEA spectrograph to create a prototype on-sky demonstrator instrument and conducted a proof-of-concept test. For that we fabricated the slit reformatting device and pigtailed it to a multimode fibre, and built the spectrograph using off-the-shelf components. The spectrum of a broadband light source featured periodic speckles. The speckles were identified as being related to the modal noise originating from uneven

filling of the modes in the multimode fibre. The tests showed that it can be avoided by injecting the signal directly to the photonic lantern or by using a fibre shaker to agitate the fibre.

The on-sky demonstration was performed using sunlight and starlight from Antares. We obtained a solar spectrum by directing the sunlight into the multimode fibre by means of a set of heliostats. The starlight data were acquired on the 0.4 m telescope at the Macquarie University Observatory in the northern part of Sydney. Although the Sun does not possess many spectral feature in the near-IR we were able to see multiple atmospheric water absorption lines. The starlight observations turned out to be more challenging than expected. However, we managed to record the signal from Antares and identify multiple CO band heads in H band, as well as atmospheric water absorption demonstrating the feasibility of the technique.

In summary, we showed promising performance of integrated photonic lanterns and slit reformatting devices. We not only demonstrated the devices in the laboratory environment but also conducted observations in an observatory infrastructure.

8.2 Future work

The primary direction for future activities is to create photonic lanterns, and particularly slit reformatting devices operating in the visible wavelength regime. The visible wavelength regime is used for radial velocity studies in search of exoplanets and asteroseismology measurements. The precision of such measurements is highly enhanced when using single-mode spectrographs. There are two visible single-mode RHEA spectrographs [27, 130] built at Macquarie University and available for implementation of the slit reformatting devices. Based on the experience from the near-IR devices and recent development of the process to fabricate low-loss single-mode waveguides at 800 nm using the annealing technique [115], we are planning to fabricate the first devices operating at 800 nm and then move down to 400-600 nm. There devices will be also tested at the Macquarie University Observatory. Our long-term vision is to produce compact, high efficiency, high precision, high stability and relatively cheap

single-mode spectrographs which can be easily adapted for 0.5-1 m class telescopes.

In the future, we also plan to fabricate visible devices accommodating hundreds of waveguides to be used on 4-metre class telescopes. Our current limit of the number of waveguides in 3D geometry is 127. However, we are working on upgrading the system to increase the depth range of the femtosecond laser writing system.

Another avenue of integrated photonic lanterns is the development of low-loss multi-band filters. With new experience in low-absorption glass AF45, as well as new promising results with glass Corning Gorilla [143] we will fabricate low-loss near-IR photonic lanterns. A new femtosecond laser system is being built at Macquarie University and it will enable the fabrication of waveguide Bragg gratings with the phase mask technique using IR laser pulses. We expect to produce devices with transmission as high as 95% and a few gratings of 20-30 dB strength.

A

An Appendix

Formula derivation

The number of modes in the focus of a telescope can be calculated by comparing the number of modes in a multimode fibre and the number of modes created in the focus of telescope.

The number of modes N_m per polarisation state in a multimode fibre is given by [31]:

$$N_m = \frac{V^2}{4}, \tag{A.1}$$

where

$$V = \frac{\pi \cdot d_{\text{Fibre}} \cdot \text{NA}}{\lambda} \tag{A.2}$$

is the normalised frequency, d_{Fibre} is the fibre diameter, λ is the wavelength and NA is the numerical aperture, given by

$$\text{NA} \approx \frac{1}{2 \cdot F/\#}, \tag{A.3}$$

where $F/\#$ is the focal ratio. The telescope plate scale PS is defined as

$$PS = \frac{\theta_{Focus}}{d_{Focus}} = \frac{1}{D_{Telescope} \cdot F/\#}[rad/mm] \Rightarrow d_{\text{Focus}} = \theta_{\text{Focus}}(\lambda) \cdot D_{\text{Telescope}} \cdot F/\# \tag{A.4}$$

where $\theta_{Focus}(\lambda)$ is the angular size of the of the focus and is defined as

$$\theta_{\text{Focus}}(\lambda) = \sqrt{\theta_{\text{Diffraction}}(\lambda)^2 + \theta_{\text{Seeing}}(\lambda)^2}, \tag{A.5}$$

where $D_{\text{Telescope}}$ is the diameter of telescope, $\theta_{\text{Diffraction}}(\lambda)$ is the angular diameter of the telescope diffraction spot and $\theta_{\text{Seeing}}(\lambda)$ is the seeing of the telescope site (in rad).

The V number is then

$$V = \frac{2}{\pi} \cdot \frac{1}{2 \cdot F/\#} \cdot \theta_{\text{Focus}}(\lambda) \cdot D_{\text{Telescope}} \cdot F/\# = \frac{\pi \cdot \theta_{\text{Focus}}(\lambda) \cdot D_{\text{Telescope}}}{2\lambda}, \tag{A.6}$$

and the number of modes N_m is

$$N_m = \frac{V^2}{4} = \frac{1}{4} \cdot \left(\frac{\pi \cdot \theta_{Focus}(\lambda) \cdot D_{Telescope}}{2 \cdot \lambda} \right)^2 = \frac{\pi^2}{16} \cdot \left(\frac{\theta_{\text{Focus}}(\lambda) \cdot D_{Telescope}}{\lambda} \right)^2. \tag{A.7}$$

B

An Appendix B

This appendix includes the source code of the MATLAB program which designs the transition between the isolated waveguides section and the fanout section of the slit reformatting devices. Based on these functions the GUI which was shown in Fig. 3.13 was developed. All scripts shown here and the GUI were coded by myself.

```
function best_connections = DesignLantern(NWg, NumberOfIterations)
    % NWg -- Number of waveguides
    % NumberOfIterations -- Number of Iterations to find the best
    % set of connections between the isolated waveguide
    % and the fanouts
    clc;
    close all
```

```
%----------------------Set the parameters -------------------------------
Depth = 0.3;     % Depth of the centre of the lantern
NSeg = 3;    % Number of segments (mm section, taper section, fan out, ...)
LMM = 3;     % Length of the multimode section [mm]
LTap = 10;  % Length of the taper section
LFan = 10;  % Lenght of the fan-out section
SegVec = [0 LMM LTap LFan];    %Segment vector, add all segment parameters in order
Ltotal = sum(SegVec);
RhoIn = 0.015;          % Radius of the of the circles in the MM section
RhoTap = 0.035;       % Radius of the circles in the isolated wvaguides section
RhoFanOut=0.127;  % distance between the waveguides in the fanout

%#####################################################

% Create 6-based rings ...
Pattern = 6;
NumCircs = NumberOfCirclesForWaveguideCount(NWg, Pattern);
if ~NumCircs
    Pattern = 5;
    NumCircs = NumberOfCirclesForWaveguideCount(NWg, Pattern);
end;
if ~NumCircs
    error('DesignLantern:illegalWaveguideCount', ...
              'Don''t know how to handle that waveguide count');
end;

XCoordMM = zeros(1, NWg);
ZCoordMM = zeros(1, NWg);

% Create the input MM
% circ tells which circle around (0,0) it is
Offset = 0;
for circ = 0:NumCircs
    NumPoints = circ*Pattern;
    Angles = 2*pi * (1:NumPoints) / NumPoints;
```

```
        XCoordMM(Offset+1:Offset+NumPoints) = ...
                circ * round2(cos(Angles), 0.0001);
        ZCoordMM(Offset+1:Offset+NumPoints) = ...
                 circ * round2(sin(Angles), 0.0001);
        Offset = Offset + NumPoints;
    end;

    % Coordinates of fanout end
    Radius = (NWg-1) / 2;
    XCoordFanOut = RhoFanOut*(-Radius:Radius);
    ZCoordFanOut = zeros(1,NWg);
    YCoordFanOut = ones(1,NWg) * (LMM+LTap+LFan);

    XCoord = [ RhoIn*XCoordMM(:) , RhoIn*XCoordMM(:), ...
             RhoTap*XCoordMM(:) , XCoordFanOut(:) ]';
    ZCoord = [ RhoIn*ZCoordMM(:) , RhoIn*ZCoordMM(:), ...
             RhoTap*ZCoordMM(:) , ZCoordFanOut(:) ]' + Depth;
    YCoord = [ 0 , LMM , LMM+LTap, ...
             LMM+LTap+LFan ]' * ones(1,NWg);


%% Create a map of the length of cosine arcs of each combination
Distances = PairwiseDistance( XCoord(:,:), ZCoord(:,:), YCoord(:,:));

    Scores = zeros(NWg,1);
    KeepOrder = zeros(NumberOfIterations,NWg);
    BestScore = Inf;
    for iter = 1:NumberOfIterations
        % Create a random ordering

        [Ordering,TotalScore] = FindRandomPermutationCost(Distances);

        if TotalScore < BestScore
            BestOrdering = Ordering;
            BestScore = TotalScore;
        end
```

```
        KeepOrder(iter,:) = Ordering;
        Scores(iter) = TotalScore;
end

     %put the results (permutation + TotalScore) into one matrix
    OrderScores = [KeepOrder, Scores];
    OrderScores  = sortrows(OrderScores, size(OrderScores,2));
    ResultToDispaly = 1;

    XCoord = [XCoord(1:3, OrderScores(ResultToDispaly,1:NWg)); XCoord(4,:)];
    ZCoord = [ZCoord(1:3, OrderScores(ResultToDispaly,1:NWg)); ZCoord(4,:)];
    YCoord = [YCoord(1:3, OrderScores(ResultToDispaly,1:NWg)); YCoord(4,:)];

    CurrentScore = OrderScores(ResultToDispaly,end)

    TotalDistance = sum(sqrt((XCoord(3,:) - XCoordFanOut).^2 + ...
    (ZCoord(3,:) - ZCoordFanOut).^2 + (YCoord(3,:) - YCoordFanOut).^2))

    end

%################################
% A rounding function
function NN = round2(N, amt)
    NN = round(N / amt) * amt;
end

%################################
% A function to create circular patterns
function NumCircs = NumberOfCirclesForWaveguideCount(NWg, WaveguidePattern)
    NCircs = (sqrt((NWg - 1)/WaveguidePattern * 8 + 1) - 1) / 2;

    NWg_reconstructed = ((NCircs*2 + 1)^2 - 1) / 8 * WaveguidePattern + 1;
    if NWg_reconstructed == NWg
        NumCircs = NCircs;
    else
        NumCircs = 0;
```

```
    end
end

%################################
% Calculates the cosine arc distance if the connections
function D = PairwiseDistance( X, Z, Y )
NWg = size(X,2);
ampl = zeros(NWg,NWg);
D = zeros(NWg,NWg);

    for i=1:NWg
            for j = 1:NWg
            ampl(i,j) = sqrt((X(end,j)-X(end-1,i)).^2+(Z(end,j)-Z(end-1,i)).^2);
            D(i,j) = CosineArcLength(ampl(i,j),Y(end-1,i),Y(end,j));
           end
   end
end

%################################
% Calculates the arc length of the cosine connection
function length = CosineArcLength(ampl, startPoint, endPoint)
  helper = @(x) sqrt(1+(ampl*sin(x)).^2);
  length = quad(helper, startPoint, endPoint);
end

%################################
% Very basic - randomly match inputs to outputs,
%and calculate the sum of the distances between them.
function [Permutation,TotalScore] = FindRandomPermutationCost(D)
     NWg = size(D,1);
    Length = zeros(NWg);
    Permutation = randperm(NWg);

    for i=1:NWg
        Length(i) = D(Permutation(i),i);
    end
```

```
    TotalScore = sum(Length(:));
end

% ##############################
```

List of Symbols and Acronyms

NA ..... numerical aperture

SM ..... single-mode

MM..... multimode

PL..... photonic lantern

FBG..... fibre Bragg grating

WBG..... waveguide Bragg grating

FWHM..... full width half maximum

FRD..... focal ratio degradation

DIC ..... differential contrast microscopy

PSF ..... point spread function

V ..... V-number, normalised frequency

λ ..... wavelength

λ_B ..... Bragg wavelength

Λ ..... period of the refractive index modification

n ..... refractive index

n_{core} ..... refractive index of the core

n_{cladding} .... refractive index of the cladding

n_{eff} ..... effective refractive index

r_0 ..... Fried parameter

θ_{Seeing} ..... angular size of the seeing spot

$\theta_{\text{Diffraction}}$ ... angular size of the diffraction spot

$D_{\text{Telescope}}$ .... telescope diameter

$F/\#$ ..... focal ratio

PSF ..... point spread function

AO ..... adaptive optics

R ..... resolving power

β ..... propagation constant

α ..... overlap coefficient

ω ..... angular frequency of a wave

k ..... wavenumber

c ..... speed of the light

PS ..... plate scale

N_m ..... number of modes

OH ..... hydroxyl

S/N ..... signal-to-noise ratio

List of Publications

Refereed Journal Publications

- I. Spaleniak, S. Gross, N. Jovanovic, R. J. Williams, J. S. Lawrence, M. J. Ireland, and M. J. Withford, "Multiband processing of multimode light: combining 3D photonic lanterns with waveguide Bragg gratings," *Laser and Photonics Review*, vol. 8, no. 1, pp. L1–L5, 2013.

- I. Spaleniak, N. Jovanovic, S. Gross, M. J. Ireland, J. S. Lawrence, and M. J. Withford, "Integrated photonic building blocks for next-generation astronomical instrumentation II: the multimode to single mode transition," *Opt. Express*, vol. 21, no. 22, pp. 27197–27208, 2013.

- N. Jovanovic, I. Spaleniak, S. Gross, M. Ireland, J. S. Lawrence, C. Miese, A. Fuerbach, and M. J. Withford, "Integrated photonic building blocks for next-generation astronomical instrumentation I: the multimode waveguide," *Opt. Express*, vol. 20, no. 15, pp. 17029–17043, 2012.

Conference Publications

- S. Gross, A. Arriola, G. Palmer, N. Jovanovic, I. Spaleniak, T. D. Meany, Y. Duan, Q. Liu, P. Dekker, D. G. Lancaster, H. Ebendorff-Heidepriem, P. G. Tuthill, B. Norris, A. Fuerbach, M. Ireland, M. J. Steel, and M. J. Withford, "Ultrafast

laser inscribed 3D integrated photonics," in *Society of Photo-Optical Instrumentation Engineers (SPIE) Conference Series*, vol. 8876 of *Society of Photo-Optical Instrumentation Engineers (SPIE) Conference Series*, 2013.

- I. Spaleniak, N. Jovanovic, S. Gross, M. Ireland, J. Lawrence, and M. Withford, "Enabling photonic technologies for seeing-limited telescopes: fabrication of integrated photonic lanterns on a chip," in *Society of Photo-Optical Instrumentation Engineers (SPIE) Conference Series*, vol. 8450 of *Society of Photo-Optical Instrumentation Engineers (SPIE) Conference Series*, 2012.

- I. Spaleniak, N. Jovanovic, S. Gross, M. Ireland, J. Lawrence, and M. Withford, "Exploration of integrated photonic lanterns fabricated by femtosecond laser inscription," in *Proceedings of the International Quantum Electronics Conference and Conference on Lasers and Electro-Optics Pacific Rim 2011*, p. C430, Optical Society of America, 2011.

References

[1] N. Jovanovic, I. Spaleniak, S. Gross, M. Ireland, J. S. Lawrence, C. Miese, A. Fuerbach, and M. J. Withford. *Integrated photonic building blocks for next-generation astronomical instrumentation I: the multimode waveguide.* Optics Express **20**(15), 17029 (2012).

[2] *Giant Magellan Telescope.* URL `http://www.gmto.org/`.

[3] *The Thirty Meter Telescope.* URL `http://www.tmt.org/`.

[4] *European Extremely Large Telescope.* URL `http://www.eso.org/public/teles-instr/e-elt/`.

[5] *Solaris Project.* URL `http://www.projectsolaris.eu/en`.

[6] J. Bland-Hawthorn, J. Lawrence, G. Robertson, S. Campbell, B. Pope, C. Betters, S. Leon-Saval, T. Birks, R. Haynes, N. Cvetojevic, and N. Jovanovic. *PIMMS: photonic integrated multimode microspectrograph.* In I. S. McLean, S. K. Ramsay, and H. Takami, eds., *SPIE Astronomical Telescopes + Instrumentation*, pp. 77350N–77350N–9 (International Society for Optics and Photonics, 2010).

[7] S. G. Leon-Saval, T. A. Birks, J. Bland-Hawthorn, and M. Englund. *Multimode fiber devices with single-mode performance.* Optics Letters **30**(19), 2545 (2005).

[8] M. Mayor and D. Queloz. *A Jupiter-mass companion to a solar-type star.* Nature **378**(6555), 355 (1995).

[9] D. Noordegraaf, P. M. Skovgaard, M. D. Nielsen, and J. Bland-Hawthorn. *Efficient multi-mode to single-mode coupling in a photonic lantern.* Optics Express **17**(3), 1988 (2009).

[10] R. R. Thomson, T. A. Birks, S. G. Leon-Saval, A. K. Kar, and J. Bland-Hawthorn. *Ultrafast laser inscription of an integrated photonic lantern.* Optics Express **19**(6), 5698 (2011).

[11] G. Duchêne. *High-angular resolution imaging of disks and planets.* New Astronomy Reviews **52**(25), 117 (2008).

[12] A. Moffat. *A Theoretical Investigation of Focal Stellar Images in the Photographic Emulsion and Application to Photographic Photometry.* Astronomy and Astrophysics **3** (1969).

[13] D. L. Fried. *Optical Resolution Through a Randomly Inhomogeneous Medium for Very Long and Very Short Exposures.* Journal of the Optical Society of America **56**(10), 1372 (1966).

[14] J. Vernin and C. Munoz-Tunon. *Optical seeing at La Palma Observatory. 2: Intensive site testing campaign at the Nordic Optical Telescope.* Astronomy and Astrophysics (ISSN 0004-6361) **284**, 311 (1994).

[15] G. Raskin. *HERMES, a fibre-fed high-resolution spectrograph for the Mercator telescope.* Ph.D. thesis, Katholieke Universiteit Leuven (2011).

[16] J. Bland-Hawthorn. *Astrophophotonics: A new generation of astronomical instruments.* In *Optical Fiber Communication (OFC), collocated National Fiber Optic Engineers Conference, 2010 Conference on (OFC/NFOEC)* (2010).

[17] R. Content and J. R. P. Angel. *Design and model demonstration of a camera that removes the infrared OH background from two-dimensional images.* In D. L. Crawford and E. R. Craine, eds., *1994 Symposium on Astronomical Telescopes & Instrumentation for the 21st Century*, pp. 757–762 (International Society for Optics and Photonics, 1994).

[18] A. R. Offer and J. Bland-Hawthorn. *Rugate filters for OH-suppressed imaging at near-infrared wavelengths.* Monthly Notices of the Royal Astronomical Society **299**(1), 176 (1998). 9707298.

[19] A. Labeyrie. *Attainment of Diffraction Limited Resolution in Large Telescopes by Fourier Analysing Speckle Patterns in Star Images.* Ann. Appl. Probab. **6** (1970).

[20] J. E. Baldwin, P. J. Warner, and C. D. Mackay. *The point spread function in Lucky Imaging and variations inseeing on short timescales.* Astronomy and Astrophysics **480**(2), 589 (2008).

[21] H. W. Babcock. *The Possibility of Compensating Astronomical Seeing.* Publications of the Astronomical Society of the Pacific **65**, 229 (1953).

[22] J. Bland-Hawthorn and P. Kern. *Astrophotonics: a new era for astronomical instruments.* Optics Express **17**(3), 1880 (2009).

[23] M. T. Murphy, T. Udem, R. Holzwarth, A. Sizmann, L. Pasquini, C. Araujo-Hauck, H. Dekker, S. D'Odorico, M. Fischer, T. W. Hansch, and A. Manescau. *High-precision wavelength calibration of astronomical spectrographs with laser frequency combs.* Monthly Notices of the Royal Astronomical Society **380**(2), 839 (2007).

[24] J.-B. Le Bouquin, J.-P. Berger, B. Lazareff, G. Zins, P. Haguenauer, L. Jocou, P. Kern, R. Millan-Gabet, W. Traub, O. Absil, J.-C. Augereau, M. Benisty, N. Blind, X. Bonfils, P. Bourget, A. Delboulbe, P. Feautrier, M. Germain, P. Gitton, D. Gillier, M. Kiekebusch, J. Kluska, J. Knudstrup, P. Labeye, J.-L. Lizon, J.-L. Monin, Y. Magnard, F. Malbet, D. Maurel, F. Ménard, M. Micallef, L. Michaud, G. Montagnier, S. Morel, T. Moulin, K. Perraut, D. Popovic, P. Rabou, S. Rochat, C. Rojas, F. Roussel, A. Roux, E. Stadler, S. Stefl, E. Tatulli, and N. Ventura. *PIONIER: a 4-telescope visitor instrument at VLTI.* Astronomy & Astrophysics **535**, A67 (2011).

[25] N. Jovanovic, P. G. Tuthill, B. Norris, S. Gross, P. Stewart, N. Charles, S. Lacour, M. Ams, J. S. Lawrence, A. Lehmann, C. Niel, J. G. Robertson, G. D. Marshall, M. Ireland, A. Fuerbach, and M. J. Withford. *Starlight demonstration of the Dragonfly instrument: an integrated photonic pupil-remapping interferometer for high-contrast imaging.* Monthly Notices of the Royal Astronomical Society **427**(1), 806 (2012).

[26] N. Cvetojevic, N. Jovanovic, J. Lawrence, M. Withford, and J. Bland-Hawthorn. *Developing arrayed waveguide grating spectrographs for multi-object astronomical spectroscopy.* Optics Express **20**(3), 2062 (2012).

[27] C. H. Bacigalupo. *A Compact Spectrograph to Search for Extrasolar Planets.* Honours thesis, Macquarie University (2012).

[28] A. Ghasempour, J. Kelly, M. W. Muterspaugh, and M. H. Williamson. *A single-mode Echelle spectrograph: eliminating modal variation, enabling higher precision Doppler study.* In R. Navarro, C. R. Cunningham, and E. Prieto, eds., *SPIE Astronomical Telescopes + Instrumentation*, p. 845045 (International Society for Optics and Photonics, 2012).

[29] C. H. Betters, S. G. Leon-Saval, J. G. Robertson, and J. Bland-Hawthorn. *Beating the classical limit: a diffraction-limited spectrograph for an arbitrary input beam.* Optics Express **21**(22), 26103 (2013).

[30] K. Okamoto. *Fundamentals of Optical Waveguides* (Academic Press, Elsevier Inc., 2006), second edi ed.

[31] A. Snyder and J. Love. *Optical Waveguide Theory*, vol. 1983 (Springer, 1983).

[32] L. W. Ramsey. *Focal ratio degradation in optical fibers of astronomical interest.* IN: Fiber optics in astronomy; Proceedings of the Conference pp. 26–39 (1988).

[33] S. C. Barden. *Review of Fiber-Optic Properties for Astronomical Spectroscopy.* Fiber Optics in Astronomy III. ASP Conference Series **152** (1998).

[34] C. L. Poppett and J. R. Allington-Smith. *The dependence of the properties of optical fibres on length.* Monthly Notices of the Royal Astronomical Society **404**(3), 1349 (2010).

[35] F. Bouchy and P. Connes. *Autoguider locked on a fiber input for precision stellar radial velocities.* Astronomy and Astrophysics Supplement Series **136**(1), 193 (1999).

[36] F. Bouchy, R. F. Diaz, G. Hébrard, L. Arnold, I. Boisse, X. Delfosse, S. Perruchot, and A. Santerne. *SOPHIE+: First results of an octagonal-section fiber for high-precision radial velocity measurements.* Astronomy & Astrophysics p. 12 (2012). 1211.4785.

[37] J.-C. Olaya, S. G. Leon-Saval, D. Schirdewahn, K. Ehrlich, D. M. Haynes, and R. Haynes. *1:61 photonic lanterns for astrophotometry: a performance study.* Monthly Notices of the Royal Astronomical Society **427**(2), 1194 (2012).

[38] T. R. Hunter and L. W. Ramsey. *Scrambling properties of optical fibers and the performance of a double scrambler.* Publications of the Astronomical Society of the Pacific **104**, 1244 (1992).

[39] G. Avila and P. Singh. *Optical fiber scrambling and light pipes for high accuracy radial velocities measurements.* In E. Atad-Ettedgui and D. Lemke, eds., *SPIE Astronomical Telescopes + Instrumentation*, pp. 70184W–70184W–7 (International Society for Optics and Photonics, 2008).

[40] G. Avila, P. Singh, and B. Chazelas. *Results on fibre scrambling for high accuracy radial velocity measurements.* In I. S. McLean, S. K. Ramsay, and H. Takami, eds., *SPIE Astronomical Telescopes + Instrumentation*, pp. 773588–773588–9 (International Society for Optics and Photonics, 2010).

[41] P. Connes, M. Martic, and J. Schmitt. *Demonstration of photon-noise limit in stellar radial velocities.* Astrophysics and Space Science **241**(1), 61 (1996).

[42] R. E. Epworth. *Phenomenon of modal noise in fiber systems - 1979 OSA Technical Digest Series.* In *Optical Fiber Communication*, p. ThD1 (Optical Society of America, Washington, D.C., 1979).

[43] E. G. Rawson, J. W. Goodman, and R. E. Norton. *Frequency dependence of modal noise in multimode optical fibers.* Journal of the Optical Society of America **70**(8), 968 (1980).

[44] J. Baudrand and G. A. H. Walker. *Modal Noise in High-Resolution, Fiber- fed Spectra: A Study and Simple Cure.* Publications of the Astronomical Society of the Pacific **113**(785), 851 (2001).

[45] J. Bland-Hawthorn, A. Buryak, and K. Kolossovski. *Optimization algorithm for ultrabroadband multichannel aperiodic fiber Bragg grating filters.* Journal of the Optical Society of America A **25**(1), 153 (2008).

[46] C. Q. Trinh, S. C. Ellis, J. Bland-Hawthorn, J. S. Lawrence, A. J. Horton, S. G. Leon-Saval, K. Shortridge, J. Bryant, S. Case, M. Colless, W. Couch, K. Freeman, H.-G. Löhmannsröben, L. Gers, K. Glazebrook, R. Haynes, S. Lee, J. OŹByrne, S. Miziarski, M. M. Roth, B. Schmidt, C. G. Tinney, and J. Zheng. *GNOSIS: the first instrument to use fiber Bragg gratings for OH suppression.* The Astronomical Journal **145**(2), 51 (2013).

[47] S. G. Leon-Saval, A. Argyros, and J. Bland-Hawthorn. *Photonic lanterns.* Nanophotonics **2**(5-6), 429 (2013).

[48] T. A. Birks, B. J. Mangan, A. Díez, J. L. Cruz, and D. F. Murphy. *"Photonic lantern" spectral filters in multi-core Fiber.* Optics Express **20**(13), 13996 (2012).

[49] D. H. Chang, T. Azfar, S.-K. Kim, H. R. Fetterman, C. Zhang, and W. Steier. *Vertical adiabatic transition between a silica planar waveguide and an electro-optic polymer fabricated with gray-scalelithography.* Optics Letters **28**(11), 869 (2003).

[50] N. K. Fontaine, R. Ryf, J. Bland-Hawthorn, and S. G. Leon-Saval. *Geometric requirements for photonic lanterns in space division multiplexing.* Optics Express **20**(24), 27123 (2012).

[51] D. Noordegraaf, P. M. W. Skovgaard, M. D. Maack, J. Bland-Hawthorn, R. Haynes, and J. Læ gsgaard. *Multi-mode to single-mode conversion in a 61 port Photonic Lantern.* Optics Express **18**(5), 4673 (2010).

[52] R. Haynes, T. A. Birks, J. Bland-Hawthorn, J. L. Cruz, A. Diez, S. C. Ellis, D. Haynes, R. G. Krämer, B. J. Mangan, S. Min, D. F. Murphy, S. Nolte, J. C. Olaya, J. U. Thomas, C. Q. Trinh, A. Tünnermann, and C. Voigtländer. *Second generation OH suppression filters using multicore fibers.* In R. Navarro, C. R. Cunningham, and E. Prieto, eds., *SPIE Astronomical Telescopes + Instrumentation*, p. 845011 (International Society for Optics and Photonics, 2012).

[53] S.-s. Min, C. Trinh, S. Leon-Saval, N. Jovanovic, P. Gillingham, J. Bland-Hawthorn, J. Lawrence, T. A. Birks, M. M. Roth, R. Haynes, and L. Fogarty. *Multicore fibre Bragg grating developments for OH suppression.* In R. Navarro, C. R. Cunningham, and E. Prieto, eds., *SPIE Astronomical Telescopes + Instrumentation*, p. 84503L (International Society for Optics and Photonics, 2012).

[54] R. R. Thomson, A. K. Kar, and J. Allington-Smith. *Ultrafast laser inscription: an enabling technology for astrophotonics.* Optics Express **17**(3), 1963 (2009).

[55] R. R. Gattass and E. Mazur. *Femtosecond laser micromachining in transparent materials.* Nat Photon **2**(4), 219 (2008).

[56] D. Du, X. Liu, G. Korn, J. Squier, and G. Mourou. *Laser-induced breakdown by impact ionization in SiO2 with pulse widths from 7 ns to 150 fs.* Applied Physics Letters **64**(23), 3071 (1994).

[57] E. N. Glezer, M. Milosavljevic, L. Huang, R. J. Finlay, T.-H. Her, J. P. Callan, and E. Mazur. *Three-dimensional optical storage inside transparent materials.* Optics Letters **21**(24), 2023 (1996).

[58] K. M. Davis, K. Miura, N. Sugimoto, and K. Hirao. *Writing waveguides in glass with a femtosecond laser.* Optics Letters **21**(21), 1729 (1996).

[59] J. Liu, Z. Zhang, S. Chang, C. Flueraru, and C. P. Grover. *Directly writing of 1-to-N optical waveguide power splitters in fused silica glass using a femtosecond laser.* Optics Communications **253**(4-6), 315 (2005).

[60] K. Yamada, W. Watanabe, Y. Li, K. Itoh, and J. Nishii. *Multilevel phase-type diffractive lenses in silica glass induced by filamentation of femtosecond laser pulses.* Optics Letters **29**(16), 1846 (2004).

[61] G. D. Marshall, M. Ams, and M. J. Withford. *Direct laser written waveguide-Bragg gratings in bulk fused silica.* Optics Letters **31**(18), 2690 (2006).

[62] G. D. Marshall, P. Dekker, M. Ams, J. A. Piper, and M. J. Withford. *Directly written monolithic waveguide laser incorporating a distributed feedback waveguide-Bragg grating.* Optics Letters **33**(9), 956 (2008).

[63] G. D. Marshall, A. Politi, J. C. F. Matthews, P. Dekker, M. Ams, M. J. Withford, and J. L. O'Brien. *Laser written waveguide photonic quantum circuits.* Optics Express **17**(15), 12546 (2009).

[64] M. Kamata, M. Obara, R. R. Gattass, L. R. Cerami, and E. Mazur. *Optical vibration sensor fabricated by femtosecond laser micromachining.* Applied Physics Letters **87**(5), 051106 (2005).

[65] S. M. Eaton, M. L. Ng, J. Bonse, A. Mermillod-Blondin, H. Zhang, A. Rosenfeld, and P. R. Herman. *Low-loss waveguides fabricated in BK7 glass by high repetition rate femtosecond fiber laser.* Applied Optics **47**(12), 2098 (2008).

[66] S. M. Eaton, H. Zhang, M. L. Ng, J. Li, W.-J. Chen, S. Ho, and P. R. Herman. *Transition from thermal diffusion to heat accumulation in high repetition rate femtosecond laser writing of buried optical waveguides.* Optics Express **16**(13), 9443 (2008).

[67] G. Cerullo, R. Osellame, S. Taccheo, M. Marangoni, D. Polli, R. Ramponi, P. Laporta, and S. De Silvestri. *Femtosecond micromachining of symmetric waveguides at 1.5 m by astigmatic beam focusing.* Optics Letters **27**(21), 1938 (2002).

[68] M. A. Hughes, W. Yang, and D. W. Hewak. *Spectral broadening in femtosecond laser written waveguides in chalcogenide glass.* Journal of the Optical Society of America B **26**(7), 1370 (2009).

[69] K. Miura, J. Qiu, T. Mitsuyu, and K. Hirao. *Preparation and optical properties of fluoride glass waveguides induced by laser pulses.* Journal of Non-Crystalline Solids **256-257**, 212 (1999).

[70] J. Thomas, M. Heinrich, P. Zeil, V. Hilbert, K. Rademaker, R. Riedel, S. Ringleb, C. Dubs, J.-P. Ruske, S. Nolte, and A. Tünnermann. *Laser direct writing: Enabling monolithic and hybrid integrated solutions on the lithium niobate platform.* physica status solidi (a) **208**(2), 276 (2011).

[71] A. H. Nejadmalayeri, P. R. Herman, J. Burghoff, M. Will, S. Nolte, and A. Tünnermann. *Inscription of optical waveguides in crystalline silicon by mid-infrared femtosecond laser pulses.* Optics Letters **30**(9), 964 (2005).

[72] V. Apostolopoulos, L. Laversenne, T. Colomb, C. Depeursinge, R. P. SalatheĄ, M. Pollnau, R. Osellame, G. Cerullo, and P. Laporta. *Femtosecond-irradiation-induced refractive-index changes and channel waveguiding in bulk Ti[sup 3+]:Sapphire.* Applied Physics Letters **85**(7), 1122 (2004).

[73] R. Osellame, G. Cerullo, and R. Ramponi. *Femtosecond Laser Micromachining: Photonic and Microfluidic Devices in Transparent Materials* (Springer, 2012).

[74] B. Stuart, M. Feit, A. Rubenchik, B. Shore, and M. Perry. *Laser-Induced Damage in Dielectrics with Nanosecond to Subpicosecond Pulses.* Physical Review Letters **74**(12), 2248 (1995).

[75] M. Lenzner, J. Krüger, S. Sartania, Z. Cheng, C. Spielmann, G. Mourou, W. Kautek, and F. Krausz. *Femtosecond Optical Breakdown in Dielectrics.* Physical Review Letters **80**(18), 4076 (1998).

[76] S. Gross. *Direct-write mid-IR waveguide lasers.* Phd thesis, Macquarie University (2012).

[77] L. Keldysh. *Ionization in the Field of a Strong Electromagnetic Wave.* Journal of Experimental and Theoretical Physics **20**(5), 1307 (1965).

[78] D. J. Little, M. Ams, and M. J. Withford. *Influence of bandgap and polarization on photo-ionization: guidelines for ultrafast laser inscription [Invited].* Optical Materials Express **1**(4), 670 (2011).

[79] C. Schaffer, J. García, and E. Mazur. *Bulk heating of transparent materials using a high-repetition-rate femtosecond laser.* Applied Physics A: Materials Science & Processing **76**(3), 351 (2003).

[80] B. Stuart, M. Feit, S. Herman, A. Rubenchik, B. Shore, and M. Perry. *Nanosecond-to-femtosecond laser-induced breakdown in dielectrics.* Physical Review B **53**(4), 1749 (1996).

[81] J. F. Poumellec, B.; Niay, P.; Douay, M.; Bayon. *Photosensitivity and Quadratic Nonlinearity in Glass Waveguides: Fundamentals and Applications : Postconference Edition 1995* (Optical Society of Amer, 1995).

[82] J. W. Chan, T. Huser, S. Risbud, and D. M. Krol. *Structural changes in fused silica after exposure to focused femtosecond laser pulses.* Optics Letters **26**(21), 1726 (2001).

[83] O. M. Efimov, K. Gabel, S. V. Garnov, L. B. Glebov, S. Grantham, M. Richardson, and M. J. Soileau. *Color-center generation in silicate glasses exposed to infrared femtosecond pulses.* Journal of the Optical Society of America B **15**(1), 193 (1998).

[84] K. Hirao and K. Miura. *Writing waveguides and gratings in silica and related materials by a femtosecond laser.* Journal of Non-Crystalline Solids **239**(1-3), 91 (1998).

[85] A. M. Streltsov and N. F. Borrelli. *Study of femtosecond-laser-written waveguides in glasses.* Journal of the Optical Society of America B **19**(10), 2496 (2002).

[86] P. Dekker, M. Ams, G. D. Marshall, D. J. Little, and M. J. Withford. *Annealing dynamics of waveguide Bragg gratings: evidence of femtosecond laser induced colour centres.* Optics express **18**(4), 3274 (2010).

[87] D. J. Little, M. Ams, S. Gross, P. Dekker, C. T. Miese, A. Fuerbach, and M. J. Withford. *Structural changes in BK7 glass upon exposure to femtosecond laser pulses.* Journal of Raman Spectroscopy **42**(4), 715 (2011).

[88] L. B. Fletcher, J. J. Witcher, W. B. Reichman, A. Arai, J. Bovatsek, and D. M. Krol. *Changes to the network structure of ErYb doped phosphate glass induced by femtosecond laser pulses.* Journal of Applied Physics **106**(8), 083107 (2009).

[89] Y. Liu, B. Zhu, L. Wang, J. Qiu, Y. Dai, and H. Ma. *Femtosecond laser induced coordination transformation and migration of ions in sodium borate glasses.* Applied Physics Letters **92**(12), 121113 (2008).

[90] L. Sudrie, M. Franco, B. Prade, and A. Mysyrowicz. *Writing of permanent birefringent microlayers in bulk fused silica with femtosecond laser pulses.* Optics Communications **171**(4-6), 279 (1999).

[91] Y. Shimotsuma, P. Kazansky, J. Qiu, and K. Hirao. *Self-Organized Nanogratings in Glass Irradiated by Ultrashort Light Pulses.* Physical Review Letters **91**(24), 247405 (2003).

[92] C. Hnatovsky, R. Taylor, E. Simova, P. Rajeev, D. Rayner, V. Bhardwaj, and P. Corkum. *Fabrication of microchannels in glass using focused femtosecond laser radiation and selective chemical etching.* Applied Physics A **84**(1-2), 47 (2006).

[93] A. Marcinkevičius, S. Juodkazis, M. Watanabe, M. Miwa, S. Matsuo, H. Misawa, and J. Nishii. *Femtosecond laser-assisted three-dimensional microfabrication in silica.* Optics Letters **26**(5), 277 (2001).

[94] D. Wortmann, J. Gottmann, N. Brandt, and H. Horn-Solle. *Micro- and nanostructures inside sapphire by fs-laser irradiation and selective etching.* Optics Express **16**(3), 1517 (2008).

[95] S. Richter, C. Miese, S. Döring, F. Zimmermann, M. J. Withford, A. Tünnermann, and S. Nolte. *Laser induced nanogratings beyond fused silica - periodic nanostructures in borosilicate glasses and ULÉ.* Optical Materials Express **3**(8), 1161 (2013).

[96] W. Cai, A. R. Libertun, and R. Piestun. *Polarization selective computer-generated holograms realized in glass by femtosecond laser induced nanogratings.* Optics Express **14**(9), 3785 (2006).

[97] G. Cheng, K. Mishchik, C. Mauclair, E. Audouard, and R. Stoian. *Ultrafast laser photoinscription of polarization sensitive devices in bulk silica glass.* Optics Express **17**(12), 9515 (2009).

[98] E. N. Glezer and E. Mazur. *Ultrafast-laser driven micro-explosions in transparent materials.* Applied Physics Letters **71**(7), 882 (1997).

[99] S. Juodkazis, K. Nishimura, S. Tanaka, H. Misawa, E. Gamaly, B. Luther-Davies, L. Hallo, P. Nicolai, and V. Tikhonchuk. *Laser-Induced Microexplosion Confined in the Bulk of a Sapphire Crystal: Evidence of Multimegabar Pressures.* Physical Review Letters **96**(16), 166101 (2006).

[100] H.-B. Sun, Y. Xu, S. Juodkazis, K. Sun, M. Watanabe, S. Matsuo, H. Misawa, and J. Nishii. *Arbitrary-lattice photonic crystals created by multiphoton microfabrication.* Optics Letters **26**(6), 325 (2001).

[101] C. Miese, M. J. Withford, and A. Fuerbach. *Femtosecond laser direct-writing of waveguide Bragg gratings in a quasi cumulative heating regime.* Optics express **19**(20), 19542 (2011).

[102] N. Jovanovic, J. Thomas, R. J. Williams, M. J. Steel, G. D. Marshall, A. Fuerbach, S. Nolte, A. Tünnermann, and M. J. Withford. *Polarization-dependent effects in point-by-point fiber Bragg gratings enable simple, linearly polarized fiber lasers.* Optics Express **17**(8), 6082 (2009).

[103] K. Yamada, W. Watanabe, T. Toma, K. Itoh, and J. Nishii. *In situ observation of photoinduced refractive-index changes in filaments formed in glasses by femtosecond laser pulses.* Optics Letters **26**(1), 19 (2001).

[104] M. Ams, G. D. Marshall, D. J. Spence, and M. J. Withford. *Slit beam shaping method for femtosecond laser direct-write fabrication of symmetric waveguides in bulk glasses.* Optics Express **13**(15), 5676 (2005).

[105] A. A. Said, M. Dugan, P. Bado, Y. Bellouard, A. Scott, and J. R. Mabesa, Jr. *Manufacturing by laser direct-write of three-dimensional devices containing optical and microfluidic networks.* In P. R. Herman, J. Fieret, A. Pique, T. Okada, F. G. Bachmann, W. Hoving, K. Washio, X. Xu, J. J. Dubowski, D. B. Geohegan, and F. Traeger, eds., *Lasers and Applications in Science and Engineering*, pp. 194–204 (International Society for Optics and Photonics, 2004).

[106] H. S. Carslaw and J. J. C. Jaeger. *CONDUCTION OF HEAT IN SOLIDS. 2nde edition, Edition anglaise* (Clarendo Press, 1986).

[107] Y. Nasu, M. Kohtoku, and Y. Hibino. *Low-loss waveguides written with a femtosecond laser for flexible interconnection in a planar light-wave circuit.* Optics Letters **30**(7), 723 (2005).

[108] S. M. Eaton, M. L. Ng, R. Osellame, and P. R. Herman. *High refractive index contrast in fused silica waveguides by tightly focused, high-repetition rate femtosecond laser.* Journal of Non-Crystalline Solids **357**(11-13), 2387 (2011).

[109] S. M. Eaton, H. Zhang, P. R. Herman, F. Yoshino, L. Shah, J. Bovatsek, and A. Y. Arai. *Heat accumulation effects in femtosecond laser-written waveguides with variable repetition rate.* Optics Express **13**(12), 4708 (2005).

[110] A. M. Streltsov and N. F. Borrelli. *Fabrication and analysis of a directional coupler written in glass by nanojoule femtosecond laser pulses.* Optics Letters **26**(1), 42 (2001).

[111] S. Nolte, M. Will, J. Burghoff, and A. Tünnermann. *Ultrafast laser processing: New options for three-dimensional photonic structures.* Journal of Modern Optics **51**(16-18), 2533 (2004).

[112] J. W. Chan, T. R. Huser, S. H. Risbud, J. S. Hayden, and D. M. Krol. *Waveguide fabrication in phosphate glasses using femtosecond laser pulses.* Applied Physics Letters **82**(15), 2371 (2003).

[113] Corning. *Corning EAGLE2000.* Tech. rep., Corning (2005).

[114] T. Meany, M. Delanty, S. Gross, G. D. Marshall, M. J. Steel, and M. J. Withford. *Non-classical interference in integrated 3D multiports.* Optics express **20**(24), 26895 (2012).

[115] T. Meany, S. Gross, N. Jovanovic, A. Arriola, M. J. Steel, and M. J. Withford. *Towards low-loss lightwave circuits for non-classical optics at 800 and 1,550 nm.* Applied Physics A **114**(1), 113 (2013).

[116] *Synopsys Optical Solutions: RSoft, BeamPROP & FemSIM.* URL `http://optics.synopsys.com/rsoft/`.

[117] A. Arriola, S. Gross, N. Jovanovic, N. Charles, P. G. Tuthill, S. M. Olaizola, A. Fuerbach, and M. J. Withford. *Low bend loss waveguides enable compact, efficient 3D photonic chips.* Optics Express **21**(3), 2978 (2013).

[118] R. R. Thomson, R. J. Harris, T. A. Birks, G. Brown, J. Allington-Smith, and J. Bland-Hawthorn. *Ultrafast laser inscription of a 121-waveguide fan-out for astrophotonics.* Optics letters **37**(12), 2331 (2012).

[119] N. Cvetojevic, J. S. Lawrence, S. C. Ellis, J. Bland-Hawthorn, R. Haynes, and A. Horton. *Characterization and on-sky demonstration of an integrated photonic spectrograph for astronomy.* Optics Express **17**(21), 18643 (2009).

[120] H. Zhang, S. M. Eaton, and P. R. Herman. *Single-step writing of Bragg grating waveguides in fused silica with an externally modulated femtosecond fiber laser.* Optics Letters **32**(17), 2559 (2007).

[121] H. Zhang, S. M. Eaton, J. Li, and P. R. Herman. *Femtosecond laser direct writing of multiwavelength Bragg grating waveguides in glass.* Optics Letters **31**(23), 3495 (2006).

[122] M. Ams, P. Dekker, G. D. Marshall, and M. J. Withford. *Monolithic 100 mW Yb waveguide laser fabricated using the femtosecond-laser direct-write technique.* Optics Letters **34**(3), 247 (2009).

[123] G. D. Marshall, R. J. Williams, N. Jovanovic, M. J. Steel, and M. J. Withford. *Point-by-point written fiber-Bragg gratings and their application in complex grating designs.* Optics Express **18**(19), 19844 (2010).

[124] J. Thomas, N. Jovanovic, R. G. Becker, G. D. Marshall, M. J. Withford, T. Andreas, S. Nolte, and M. J. Steel. *Cladding mode coupling in highly localized fiber Bragg gratings: modal properties and transmission spectra.* Optics Express **19**(1), 20651 (2011).

[125] R. J. Williams, R. G. Krämer, S. Nolte, and M. J. Withford. *Femtosecond direct-writing of low-loss fiber Bragg gratings using a continuous core-scanning technique.* Optics letters **38**(11), 1918 (2013).

[126] J. Thomas, E. Wikszak, T. Clausnitzer, U. Fuchs, U. Zeitner, S. Nolte, and A. Tünnermann. *Inscription of fiber Bragg gratings with femtosecond pulses using a phase mask scanning technique.* Applied Physics A **86**(2), 153 (2006).

[127] J. Thomas, C. Voigtländer, R. Becker, D. Richter, A. Tünnermann, and S. Nolte. *Femtosecond pulse written fiber gratings: a new avenue to integrated fiber technology.* Laser & Photonics Reviews **6**(6), 709 (2012).

[128] D. Grobnic, C. Smelser, S. Mihailov, R. Walker, and P. Lu. *Fiber Bragg Gratings With Suppressed Cladding Modes Made in SMF-28 With a Femtosecond IR Laser and a Phase Mask.* IEEE Photonics Technology Letters **16**(8), 1864 (2004).

[129] M. Ams, P. Dekker, G. D. Marshall, and M. J. Withford. *Ultrafast laser-written dual-wavelength waveguide laser.* Optics letters **37**(6), 993 (2012).

[130] T. Feger, C. Bacigalupo, T. Bedding, J. Bento, D. Coutts, M. J. Ireland, Q. Parker, A. Rizzuto, and I. Spaleniak. *RHEA: the ultra-compact Replicable High-resolution Exoplanet Asteroseismology spectrograph.* In *SPIE Astronomical Telescopes + Instrumentation* (2014).

[131] R. Bernstein, S. A. Shectman, S. M. Gunnels, S. Mochnacki, and A. E. Athey. *MIKE: A Double Echelle Spectrograph for the Magellan Telescopes at Las Campanas Observatory.* In M. Iye and A. F. M. Moorwood, eds., *Astronomical Telescopes and Instrumentation*, pp. 1694–1704 (International Society for Optics and Photonics, 2003).

[132] J. G. Robertson and J. Bland-Hawthorn. *Compact high-resolution spectrographs for large and extremely large telescopes: using the diffraction limit* (2012). 1208.4667.

[133] J.-C. Olaya, K. Ehrlich, D. M. Haynes, R. Haynes, S. G. Leon-Saval, and D. Schirdewahn. *Multimode to single-mode converters: new results on 1-to-61 photonic lanterns.* In R. Navarro, C. R. Cunningham, and E. Prieto, eds., *SPIE Astronomical Telescopes + Instrumentation*, p. 84503K (International Society for Optics and Photonics, 2012).

[134] S. G. Leon-Saval, C. H. Betters, and J. Bland-Hawthorn. *The Photonic TIGER: a multicore fiber-fed spectrograph.* In R. Navarro, C. R. Cunningham, and E. Prieto,

eds., *SPIE Astronomical Telescopes + Instrumentation*, p. 84501K (International Society for Optics and Photonics, 2012).

[135] C. H. Betters, S. G. Leon-Saval, J. Bland-Hawthorn, and G. Robertson. *Demonstration and design of a compact diffraction limited spectrograph.* In I. S. McLean, S. K. Ramsay, and H. Takami, eds., *SPIE Astronomical Telescopes + Instrumentation*, p. 84463H (International Society for Optics and Photonics, 2012).

[136] N. Cvetojevic, N. Jovanovic, C. Betters, J. S. Lawrence, S. C. Ellis, G. Robertson, and J. Bland-Hawthorn. *First starlight spectrum captured using an integrated photonic micro-spectrograph.* Astronomy & Astrophysics **544**, L1 (2012).

[137] N. Jovanovic, P. G. Tuthill, B. Norris, S. Gross, P. Stewart, N. Charles, S. Lacour, J. Lawrence, G. Robertson, A. Fuerbach, and M. J. Withford. *Progress and challenges with the Dragonfly instrument; an integratedphotonic pupil-remapping interferometer.* In F. Delplancke, J. K. Rajagopal, and F. Malbet, eds., *SPIE Astronomical Telescopes + Instrumentation*, p. 844505 (International Society for Optics and Photonics, 2012).

[138] N. Charles, N. Jovanovic, S. Gross, P. Stewart, B. Norris, J. O'Byrne, J. S. Lawrence, M. J. Withford, and P. G. Tuthill. *Design of optically path-length-matched, three-dimensional photonic circuits comprising uniquely routed waveguides.* Applied Optics **51**(27), 6489 (2012).

[139] B. Daino, G. De Marchis, and S. Piazzolla. *Speckle and Modal Noise in Optical Fibres Theory and Experiment.* Optica Acta: International Journal of Optics **27**(8), 1151 (1980).

[140] H. Olesen. *Dependence of modal noise on source coherence and fibre length.* Electronics Letters **16**(6), 217 (1980).

[141] J. C. Corbett. *Photonic crystal fibres in astronomy.* Ph.D. thesis, Durham University. (2006).

[142] S. D. Lord. *IR Transmission Spectra.* NASA Technical Memorandum **103957** (1992).

[143] J. Lapointe, M. Gagné, M.-J. Li, and R. Kashyap. *Making smart phones smarter with photonics.* Optics express **22**(13), 15473 (2014).